

Inductive Magnetic Energy Harvesting—Modeling, Power Conversion and Control

A Dissertation Presented

by

Qian Sun

to

The Department of Electrical and Computer Engineering

in partial fulfillment of the requirements
for the degree of

Doctor of Philosophy

in the field of

Electrical Engineering

Northeastern University
Boston, Massachusetts

July 15, 2016

Acknowledgments

I would like to express my deepest gratitude to my advisor, Dr. Brad Lehman, for his continuous support and guidance for the past six years. We owe him so much for maintaining such a great research environment for everyone in the power electronics group. Dr. Brad Lehman makes fair judgment to students works, gives students guidance whenever necessary, and has extraordinary patience to discuss research problems with students. I feel deeply grateful and lucky to have him as my research advisor in this journey.

I would also like to show my special thanks to Dr. Julia Zhang for reviewing and providing insightful comments on Chapter 2 of my dissertation.

I am grateful to my committee members, Dr. Nian-Xiang Sun and Dr. Peng Li, who examine my dissertation and give me so many valuable suggestions.

I am fortunate to meet all my friends during my graduate study in Boston. I would like to thank all my colleagues in the power electronics research group: Dr. Song Chen, Dr. Ye Zhao, Ling Yang, Dr. Chung-Ti Hsu, Stephanie Quinn, Su Sheng, Jen-Hung Huang, Dawood Talebi, Yue Zheng, Dr. Yuan Li, Xinmin Zhang, Jonathan Kim and Dr. Albert Alexander, who provide me their friendly help and professional suggestions. I would like to thank my friends: Ji Hao, Dr. Hankang Yang, Sanwei Liu, Dr. Run Zhu, Dr. Yuezhou Chen for the friendship over the years and wonderful memories in Boston.

I would also like to say thank you to Lindsay Sorensen for proofreading my publications.

Finally, I would like to express my great appreciation to my family members: my parents and my husband. I would not able to pursue the doctoral study without my parents, Peilun Yin and Changhai Sun, who are always proud of any trivial achievements I made and have never limited me because I am a girl. I am fortunate to have my husband, Dr. Sanzhong Bai, who discussed research problems with me, endured my bad temper when I was frustrated and took most of the houseworks when I was busying with this thesis. All their love and support over the past years helped me to make my dream come true.

Contents

List of Figures	vii
List of Tables	x
List of Variables	xi
Abstract	xiv
1 Introduction	1
1.1 Motivation and Background	1
1.2 Problem Statement	4
1.3 Dissertation Organization	7
2 Modeling and Optimization	9
2.1 Overview	11
2.2 Inductive Magnetic Harvester Modeling	15
2.2.1 Magnetic Circuit Model (<i>Step 1</i>)	16
2.2.2 Electrical Circuit Model (<i>Step 2</i>)	18
2.2.3 Finite Element Analysis (FEA) Simulation	21
2.2.3.1 FEA model (<i>Step 3(A)</i>)	22
2.2.3.2 L_{eq} Calculation (<i>Step 4(A)</i>)	23
2.2.4 L_k and L_m (<i>Step 4(A)</i>)	25
2.2.5 Experimental Measurement	27
2.2.6 Clarification and Correction of Preliminary Research	29
2.3 Conclusion and Comparison between FEA and Experimental Modeling Approach	30
3 AC-DC Power Conversion for Magnetic Energy Harvester	31
3.1 Literature Review	33
3.1.1 Conventional Rectifier	33
3.1.2 Piezoelectric AC-DC rectifiers (SSH circuit)	35
3.1.3 Boost Derived AC-DC Converters	36
3.1.4 Summary	38

3.2	Capacitive Rectifier Based on Synchronized Switch Harvesting Technique	40
3.2.1	A Family of SSH Capacitive Rectifiers	40
3.2.2	Synchronized Switch Harvesting on Resonant Capacitor	43
3.2.2.1	Conventional Rectification	43
3.2.2.2	Type I Capacitive Rectifier	46
3.2.2.3	Type II Capacitive Rectifier	51
3.2.2.4	Type III Capacitive Rectifier	53
3.2.3	Experimental Result	54
3.3	Dual Polarity Boost Converter	57
3.3.1	Principle of Operation	58
3.3.2	Power Loss Analysis	62
3.3.3	Experimental Result	64
3.4	Conclusion	66
4	Maximum Power Point Tracking Control	68
4.1	Literature Review	70
4.1.1	Approximate Optimal Reference Voltage	71
4.1.2	PWM Based Perturb and Observe Method	72
4.1.3	Perturb and Observe Method with Active Bridge	74
4.2	Proposed MPPT Control Algorithm	75
4.2.1	Impedance Matching	79
4.2.2	Phase/RMS Control Algorithm	82
4.2.3	Simplified Quasi-MPPT Method	88
4.3	Control Implementation	98
4.3.1	Current Sampling	99
4.3.2	Limitation on Conversion Ratio	101
4.3.3	Current Reference (Phase/RMS)	102
4.3.4	Frequency Tracking (Phase/RMS)	105
4.4	Stability Analysis	107
4.4.1	Duty Ratio to Input Current $G_{id}(s)$	109
4.4.2	Input Current to Output Current G_{io}	112
4.4.3	Perturb and Observe Algorithm	113
4.5	Experimental Results	115
4.6	Dynamic Input Voltage/Frequency	124
4.6.1	Simulation	125
4.6.2	Experiments	131
4.6.2.1	Experiment 1: Programmable AC Source	131
4.6.2.2	Experiment 2: Real Rotational Harvester	133
4.7	Conclusion	136
5	Conclusions and Future Work	139

5.1	Conclusions	139
5.2	Future Work	141
 A Source Code of The Phase/RMS Algorithm		 145
 B Converter Schematics		 164
 Bibliography		 167

List of Figures

1.1	Energy harvesting applications (from left to right): Micro wind energy harvester (Humdinger Wind Energy); Energy harvesting rolling sneaker (Energy Harvesting Dérive); Blood bridge harvests energy from blood flow (Energy Addicts).	2
1.2	Piezoelectric harvester [1].	3
2.1	Magnetic energy harvesters with magnetic core: (a) Vibrational harvester; (b) Rotational harvester.	12
2.2	Air-cored magnetic energy harvester [11].	12
2.3	Inductive magnetic energy harvesters in equilibrium.	13
2.4	The spring mass damper system and conventional equivalent circuit.	14
2.5	The step by step modeling methodology to design a equivalent circuit.	16
2.6	The magnetic circuit model.	17
2.7	Equivalent model of inductive magnetic energy harvester.	19
2.8	Rotational magnetic harvester.	21
2.9	FEA simulation of inductive magnetic harvester.	22
2.10	Open and short circuit of harvester.	24
2.11	Equivalent inductance L_{eq} vs. Air gap derived using FEA simulation.	25
2.12	The flux density in magnets and coil cores (Gap=2mm).	27
2.13	Leakage and magnetizing inductance with gap.	27
2.14	Experimentally measured L_{eq} vs. Frequency (Air gap = 2mm).	28
3.1	Conventional power converter.	33
3.2	Active full wave rectifier.	34
3.3	Series SSHI circuit [5].	35
3.4	Boost derived AC-DC converter.	37
3.5	Proposed capacitive rectifier and its control scheme.	41
3.6	New family of ultra-low threshold capacitive rectifiers.	42
3.7	Conventional rectifier: shaded areas are the power conduction period.	44
3.8	Resonant capacitive rectifier (Type I).	46
3.9	Principle of Operation (Type I converter).	48
3.10	Resonant capacitive rectifier (Type II).	51
3.11	Resonant capacitive rectifier (Type III).	53

3.12	Open circuit voltage of proposed rotational inductive magnetic harvester.	55
3.13	Output average current vs. Frequency.	55
3.14	Capacitive rectifier: (a) Output current (100mA/div); (b) Output voltage (2V/div).	57
3.15	Capacitive rectifier: (a) Output current (100mA/div); (b) Output voltage (2V/div).	57
3.16	Proposed circuit and input current.	59
3.17	Principle of Operation:(a) (b) Positive half cycle of AC voltage. (c) (d) Negative half cycle of AC voltage.	60
3.18	(a) Output voltage (2V/div); (b) Input current (200mA/div).	65
4.1	MPPT with optimal reference voltage.	72
4.2	Conventional PWM based perturb and observe method.	73
4.3	Perturb and observe method with active diode bridge.	75
4.4	Match the impedance to get maximum power transfer.	76
4.5	Duty ratio of conventional MPPT and two proposed MPPT methods. .	77
4.6	The schematic diagram of proposed method.	81
4.7	Tune the phase angle and RMS of input current to achieve MPPT. .	81
4.8	Control algorithm of the MPPT method.	84
4.9	$I_{o(\text{avg})}$ vs. θ/I_{in}	85
4.10	Fixed duty ratio Quasi-MPPT method.	89
4.11	Input current changes with L_{eq} , V_{eq} , V_o and ω_{in}	91
4.12	Quasi-MPPT method: maximum power vs. L_{eq}	97
4.13	Proposed phase/RMS MPPT and quasi-MPPT control algorithm. .	100
4.14	Tune the input current i_{in} /impedance z_{in} to achieve MPPT.	101
4.15	Construct the look up table for input current reference.	105
4.16	The proposed boost derived AC-DC converter is simplified.	108
4.17	Block diagram of Phase/RMS MPPT algorithm.	108
4.18	The inner loop.	109
4.19	State space average model.	110
4.20	The perturbation settling time.	114
4.21	Experimental results of power amplifier (Phase/RMS MPPT): $f_{in} = 100\text{Hz}$; X-axis: 4ms/div; Y-axis: (a) Ch2: $v_{eq} = 3\text{VRMS}$, 5V/div; Ch3: i_{in} , 200mA/div; and (b) Ch2: v_{eq} , 1.5VRMS, 2V/div; Ch3: i_{in} ,200mA/div.	117
4.22	Experimental results of power amplifier (Phase/RMS MPPT): X-axis: 40ms/div; Y-axis: (a) f_{in} from 100Hz to 50Hz; Ch2: $v_{eq} = 2\text{VRMS}$, 2V/div; Ch3: i_{in} , 200mA/div; and (b) v_{eq} from 1.5VRMS to 3VRMS; Ch2: v_{eq} , 2V/div; Ch3: i_{in} , 200mA/div.	118

4.23 Experimental waveforms of magnetic harvester (Phase/RMS MPPT): X-axis: (a) 10ms/div; (b) 4ms/div; (c) 100ms/div; Y-axis: (a) $f_{in} = 40\text{Hz}$; Ch1: V_o , 2V/div; Ch2: i_{in} , 1V/div(250mA/div); Ch3: i_o , 50mA/div; (b) $f_{in} = 100\text{Hz}$; Ch1: V_o , 5V/div; Ch2: i_{in} , 1V/- div(250mA/div); Ch3: i_o , 100mA/div; (c) f_{in} from 40Hz to 100Hz; Ch1: V_o , 5V/div; Ch2: i_{in} , 1V/div(250mA/div); Ch3: i_o , 100mA/div.	120
4.24 Output current vs. Frequency	123
4.25 Output power vs. Frequency	124
4.26 Block diagram of MPPT algorithms comparison.	125
4.27 The Perturb & Observe controlled parameters vs. Time.	128
4.28 The duty ratio of three methods	128
4.29 Instantaneous power of Phase/RMS MPPT, Quasi-MPPT and PWM based MPPT method (MATLAB/Simulink).	129
4.30 Instantaneous power of Phase/RMS MPPT, Quasi-MPPT and PWM based MPPT method (Chroma AC source).	132
4.31 Instantaneous power of Phase/RMS MPPT, Quasi-MPPT and PWM based MPPT method (Harvester).	134
4.32 Frequency jitter lowers the output power.	136
4.33 Harvester open circuit voltage at 100Hz and 200Hz.	137
4.34 High order harmonics of harvester voltage under 100Hz and 200Hz. .	137
5.1 Alternative power conversion solution.	142

List of Tables

2.1	Parameters of proposed magnetic harvester	23
3.1	Summary of the AC-DC power conditioning circuit	39
3.2	Circuit parameters of the rectifier	55
3.3	Circuit parameters and loss of the converter	65
4.1	Circuit parameters of the converter	115
4.2	Electrical performance of the system	115
4.3	Output power of three methods	129

List of Variables

Magnetic Field:

\mathcal{F}	Magnetomotive force (MMF) from magnets
\mathcal{F}_{lM}	Leakage MMF through the air
\mathcal{F}_{cp}	Coupled MMF between magnet and coil
ϕ_{lM}	Leakage flux of magnet
ϕ_{cp}	Coupled flux
ϕ_{lc}	Leakage flux of coil winding
\mathfrak{R}_{lM}	Magnetic reluctance for ϕ_{lM}
\mathfrak{R}_{coil}	Magnetic reluctance of coil winding
\mathfrak{R}_g or \mathfrak{R}'_g	Magnetic reluctance of air gap
\mathfrak{R}_{lc}	Magnetic reluctance for ϕ_{lc}
n_{lM}	Turns of coupled magnet
n_{cp}	Turns of fully coupled coil
n_{lc}	Turns of fully decoupled coil

Electrical Field (Modeling):

v_s	Harvester induced voltage
i_s	Harvester induced current
i_{in}	Harvester current to the output
i_m	Magnetizing current
L_m	Magnetizing inductance
L_k	Leakage inductance
R_w	Coil winding resistance

Electrical Parameters (Power Conversion and Control):

v_{eq}	Harvester equivalent voltage
i_L	Resonant current of harvester inductance ($i_L = i_{in}$)
v_{C_r}	Resonant voltage of resonant capacitor C_r
v_{rect}	Voltage fed into rectifier
V_o	Converter output voltage
V_{DC}	Converter output DC voltage ($V_{DC} = V_o$)
L_{eq}	Harvester equivalent inductance
C_r	Resonant capacitance

The variables in Chapter 4 will be defined as below (The input current i_{in} is used only as an example variable):

- i_{in} Lower case variable and subscript indicates instantaneous value
- I_{in} Upper case variable and lower case subscript indicates RMS value
- $\overline{i_{in}}$ ‘—’ with lower case variable indicates average value over a switching period
- $\overline{I_{in}}$ ‘—’ with upper case variable indicates average value over an input voltage line period
- \hat{i}_{in} ‘^’ with lower case indicates variable small signal value
- I_{in_q} The steady state value at quiescent operation point
- $|i_{in}|$ The absolute value

Abstract

This thesis first reviews the challenges and limitations of the existing approaches designed for inductive magnetic energy harvesting systems. An equivalent circuit model of magnetic energy harvester is developed, which takes into account the non-linearity of the magnetic reluctance and flux. Then, using the models, a family of low threshold capacitive rectifier topologies and a center tapped boost-derived AC-DC converter are derived for better convert the AC harvesting power to DC voltage. Both of the approaches avoid using the conventional two stage structure and increases the efficiency and system output power. Two new impedance matching control algorithms for bridgeless AC-DC power conversion of magnetic harvester are presented: a Phase/RMS maximum power point tracking (MPPT) method, which controls the phase and RMS value of the converter input current without voltage reference, and a Quasi-MPPT method simplified from Phase/RMS MPPT. Experimental results are presented to validated the proposed modeling, power conversion and control approaches. Comparison with previous work shows that the proposed approaches achieve higher output power for the magnetic energy harvesting system.

Chapter 1

Introduction

1.1 Motivation and Background

Mechanical energy harvesting technologies (vibrational and rotational) show great potential in replacing batteries or as a supplemental energy source to recharge batteries. They can be applied to widely available energy sources, such as wind, vibrations in automobiles/bridges, biomechanical power, human motion, and etc.

Fig. 1.1 shows some commercial products of typical lower-power mechanical energy harvesters. From left to right, three commercial energy harvesters are listed: 1. A micro wind energy harvester uses the oscillation of a thin strip of material held in tension with a spring to vibrate a magnet that generates electrical power; 2. An energy harvesting rolling sneaker that extracts energy from rotation movement; 3. A blood bridge jewelry that uses the blood flow to drive a micro motor and light

several LEDs. Most of these environmental energy resources are intermittent and discontinuous in nature. Often, a special circuit is designed and attached to the harvesters to transform the intermittent energy to the stable output power.



FIGURE 1.1: Energy harvesting applications (from left to right): Micro wind energy harvester (Humdinger Wind Energy); Energy harvesting rolling sneaker (Energy Harvesting Dérive); Blood bridge harvests energy from blood flow (Energy Addicts).

Based on the technique, mechanical energy harvesters can be divided to several categories: piezoelectric, magnetic inductive, electrostatic and magnetoelectric (ME) sensor structure, etc. So far, the piezoelectric harvesting is the most commercially mature technology compared to the other energy harvesting techniques [1–5]. The piezoelectric device creates electrical field from mechanical deformation of piezoelectric materials (Fig. 1.2). Typically, the piezoelectric harvester is modeled as an AC current source in parallel with a capacitor. It is widely adopted in the applications such as wireless sensor networks, where stable power source is hard to reach; or battery chargers, which recycles energy from ambient energy sources like human movement to achieve higher energy efficiency. The output voltage of most piezoelectric harvesters ranges from several millivolts to several volts [1, 2].

Due to its low AC output voltage, specially designed power conversion circuits are essential to low power and low voltage applications that require DC input voltage.

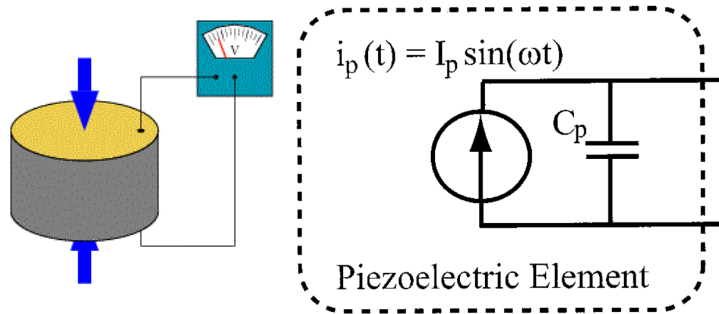


FIGURE 1.2: Piezoelectric harvester [1].

On the other hand, in electrostatic energy harvesting technology, the vibration changes the capacitance value of a variable capacitor while keeping the charge or the voltage as constant. Using the equation $Q = C \cdot V$, in the voltage constraint conversion, the capacitance drop drives charge out of the device to the load by maintaining the voltage as constant. Similarly, in the charge constraint conversion, higher voltage is created by reducing the variable capacitance and power is delivered to the load [6, 7]. Alternatively, magnetoelectric (ME) energy harvesters are made up of two layers: piezoelectric fibers (first layer) coated by high-permeability magnetostrictive alloy ribbons (second layer). The outer magnetostrictive layer vibrates when an external magnetic field is applied and the piezoelectric fiber layer creates the electrical field with the vibration [8]. Compared to the piezoelectric harvesting, the electrostatic and magnetoelectric harvesters are less widely used.

The electromagnetic harvesting technique is a new emerging transduction mechanism that has drawn more and more research attention [9–22]. It converts ambient

kinetic energy into electrical energy under the principle of Faraday's Law [9, 10].

Due to its relative high power density and output power, inductive magnetic energy harvesting technology shows intriguing potential. The research in this thesis will focus on the power electronics particularly for inductive magnetic energy harvesting.

1.2 Problem Statement

Like all the kinetic energy harvesting technologies, inductive magnetic energy harvesting is limited by the small amount of energy that can be harvested, particularly for energy scavenging applications, such as those to be studied in this research. A difficulty with extracting energy is that the output of the inductive magnetic energy harvesters may have small AC voltage in the low frequency range (typically around 100Hz). Although the output voltage might be increased by increasing the number of turns around the coil in the harvester, it may cause a large internal resistance, which would severely decrease the output power. At the same time, the voltage requirement for low voltage, low power, electronic devices is typically from 1.8VDC to 3.6VDC. Thus, rectification stage cannot be avoided in the converter design. However, at such low frequencies, additional step-up transformers cannot be used before rectification because of their large size. With fixed voltage drop on the rectifier diodes, rectification losses can dominate in the power processing circuit of magnetic harvester.

Since the inductive magnetic harvester follows the principle of Faradays Law of electromagnetism, it is typically modeled as an AC voltage source in series with a built-in inductor. Considering its low input AC voltage and possible voltage drop on the conventional rectifier, boost-derived bridgeless converter topologies are feasible for the application. The boost-derived topologies can both make use of the harvester internal inductor to reduce converter size and keep step-up conversion ratio with lower power loss on the switching devices. This has led to the initial research in designing boost-derived bridgeless converter for inductive energy harvesters to avoid some of the losses [11–18]. Meanwhile, a number of high step-up converter topologies for low power applications have also been presented, especially for piezoelectric harvesters, which this thesis will demonstrate can form a dual relationship with inductive magnetic harvesters [1–5, 23–30]. The approaches improve the converter efficiency by eliminating the diode bridge rectifier at the first stage, which is inefficient due to the power loss to overcome the diode voltage drop. For example, in [11], a direct AC-DC boost converter is designed utilizing the harvester internal inductance to avoid an external inductor for the boost converter. In this case, the harvester equivalent inductance is also used as an input inductance of a boost derived power conversion circuit. As the shared component, the harvester internal equivalent inductance can be of great importance for both harvester and converter. But it is not carefully studied or even ignored in the previous works [11–14]. Methods to optimize the operation by considering the harvester and the converter together as a system leads to new

research challenges that have yet to be discussed in the literature, such as: What models can estimate the internal equivalent inductance and also predict the harvester performance accurately? How will the shared harvester internal inductance affect the system output power? What parameters can be tuned to adjust the harvester internal inductance, and further how can the system achieve maximum output power? etc.

This thesis begins to answer these above questions. Specifically, the contributions of this research includes:

1. A procedure for magnetic harvester modeling is presented to aid both harvester and AC-DC converter design. The modeling method takes into account the nonlinearity of the magnetic reluctance and flux of the magnetic field.
2. New AC-DC converters are designed that can be fully integrated to the magnetic harvester based on the proposed new equivalent circuit model of the magnetic harvester. The proposed approach integrates the internal inductance of the magnetic harvester into the inductance of the AC-DC converter to reduce the size. New control methods are developed that can extract maximum power from the harvester, having the ability to adopt in real-time to compensate for environmental changes.

1.3 Dissertation Organization

Motivated by the previously discussed research problems, this dissertation aims to analyze the electromagnetic harvester to propose new modeling, power conversion circuit and control algorithms for electromagnetic energy harvesting applications.

Chapter 2, Chapter 3, and Chapter 4 focus on the electromagnetic harvester modeling, power conversion circuit design and control algorithm, respectively. Specifically, the dissertation is organized as follows.

Chapter 2 Models and explains the operation principle of the magnetic harvester. First, the mechanical, magnetic and electrical characteristic of the inductive magnetic harvesters are explored, and then the benefits and drawbacks of existing harvesting approaches are explained. An equivalent circuit model that considers the nonlinear effect of the magnetic field is proposed to aid the AC-DC converter design. It is subsequently used in Chapter 3. The models are validated with an experimental setup of a rotational inductive magnetic harvester.

Chapter 3 develops new AC-DC converter topologies for inductive magnetic energy harvesters. A series of resonant capacitive rectifiers that work in rotation/vibration frequency and a high frequency AC-DC converter to boost the harvester AC input voltage to 3.3VDC are proposed. The AC-DC converter are simulated with the equivalent model of the harvester developed in Chapter 2. The proposed AC-DC converters are designed, built and experimentally tested..

Chapter 4 develops new maximum power point trackers specialized for magnetic energy harvesters. A Phase/RMS MPPT algorithm is introduced based on tuning the phase and amplitude/RMS of the converter input current with perturb and observe method. Then the Phase/RMS MPPT method is simplified to a Quasi-MPPT method that directly adjusts converter duty ratio. An experimental setup of a magnetic harvester and a boost derived AC-DC converter are built to validate the two control algorithm. The proposed algorithms are also compared with the conventional MPPT algorithm used for low power energy harvesting applications.

Chapter 2

Modeling and Optimization

This chapter presents a literature review of conventional magnetic harvesters and a formal explanation of the harvester model considering the effect of the magnetic fields. As analyzed in Chapter 1, a converter is needed to change the harvester AC voltage to DC voltage for the load. In order to achieve maximum power transferred to the load, the harvester should be studied with the converter as a whole system. Therefore, this section presents an electrical circuit model of the inductive magnetic harvester. A number of approaches on modeling and optimization of the inductive magnetic harvesters have been presented [12, 19–22]. The conventional approaches tend to replace the magnetic harvester with an equivalent RLC circuit [19, 20], which is purely mechanical. The RLC circuit actually relates to mechanical parameters but not to electrical performance of the harvester. On the other hand, the most simplified electrical circuit model for magnetic harvester

is an AC voltage source [12]; but this model is over-simplified because it ignores the effect of the magnetic field [21, 22]. However, although [21, 22] consider the nonlinear effect of the magnetic field, the modeling approaches cannot easily convert to an equivalent circuit model, which is essential to aid the AC-DC converter design. Specifically, this chapter explains the following research contributions:

- A procedure to develop an equivalent circuit model for magnetic harvester based on electromagnetic theory and finite element analysis is presented. Finite dimensional models are also derived.
- An experimental rotational magnetic harvester in a roller skate is built and used to validate the proposed models on the magnetic harvester.
- The models relate the physical properties of the harvester, such as air gap between magnets and coils, number of coil turns, magnetic permeability of the core material to the harvester internal inductance. The circuit model is vital to design an AC-DC converter to rectify and boost the output voltage. It is discovered that the magnetic harvester internal inductance can be used to replace the input boost inductor on boost derived circuits.

In the preliminary research [31, 32], the magnetizing inductance L_m was assumed to be constant. This chapter clarifies incorrect assumptions and model that were previously proposed by this Ph.D research in preliminary research in Section 2.2.6.

2.1 Overview

Several inductive magnetic harvesters are shown in Fig. 2.1 and Fig. 2.2. The mechanical structure can vary depending on whether the coils of the magnetic harvester contains ferrite core inside (Fig. 2.1) or not (Fig. 2.2). An inductive magnetic harvester typically consists of magnets, coils, and rotation or vibration mechanical structure. As shown in Fig. 2.2, the air-cored magnetic harvesters do not contain high permeability cores in the coils. In order to achieve maximum flux variation, the permanent magnets are placed in the coil windings. The ferrite-cored harvesters contain high permeability cores in the coils and the permanent magnets are placed outside the coils (Fig. 2.1). The permeability of the magnetic core material can be as high as 1000 times more than the air, so it can reduce the magnetic reluctance of the magnetic path and enhance the induced voltage. Both approaches, though, share the same working principle and follow Faraday's Law of electromagnetism. They share similar equivalent models, in spite of different magnetic reluctance generated from different permeability materials in the magnetic circuit. The magnetic harvesters can also be divided into rotational (Fig. 2.1(a)) and vibrational (Fig. 2.1(b)) by its motion. Harvesters utilize the rotation or vibration movement of permanent magnets to generate an alternating magnetic field, which induces electromagnetic force (EMF) across the stator coils. In this thesis, the simulation and experiment are based on the rotational harvester shown in Fig. 2.1(b).

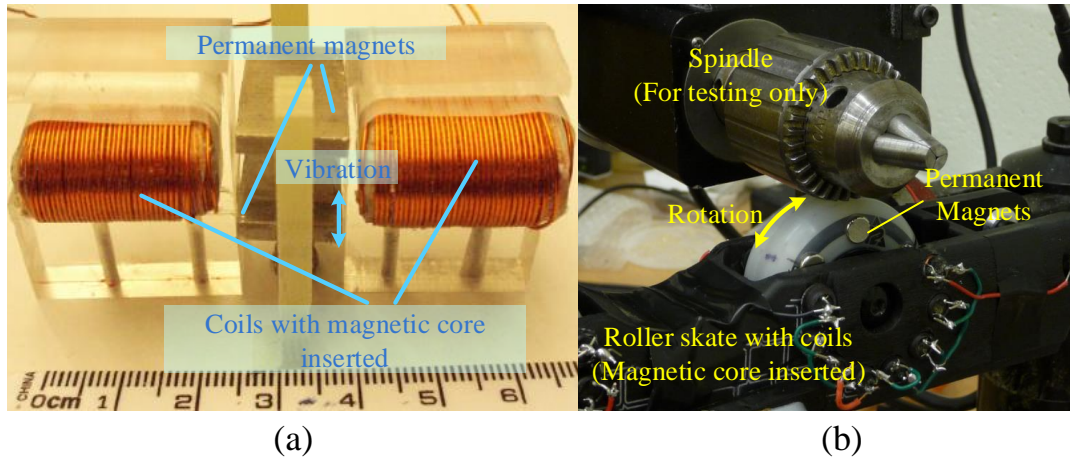


FIGURE 2.1: Magnetic energy harvesters with magnetic core: (a) Vibrational harvester; (b) Rotational harvester.

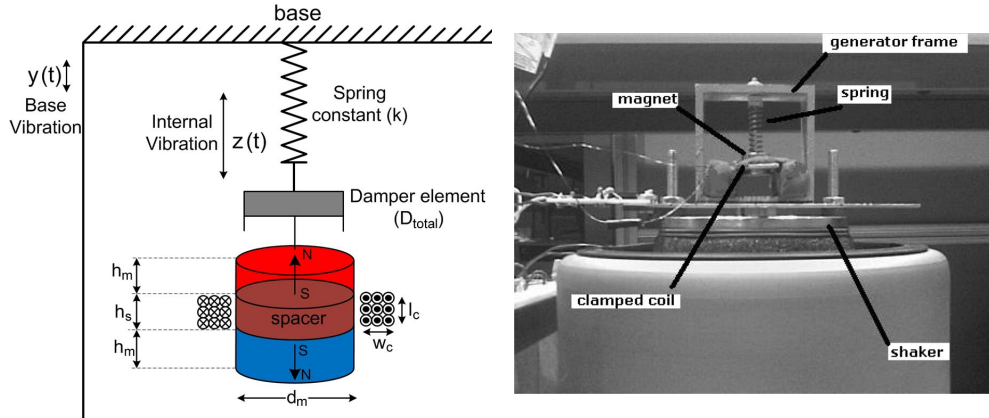


FIGURE 2.2: Air-cored magnetic energy harvester [11].

Fig. 2.3 illustrates a portion of an inductive magnetic energy harvester in equilibrium. The permanent magnets are placed to have opposite polarities of magnetization from each other, where ‘N’ is the north pole and ‘S’ is the south pole. When the magnets move with a rotational or vibrational force, an alternating magnetic field is created. The flux from the magnets can be divided into three parts: coupled flux of magnets and coil ϕ_{cp} , leakage flux of magnets ϕ_{lM} and leakage flux of coils ϕ_{lc} . The magnetic core inserted to the coil reduces the magnetic reluctance

of the magnetic path and increases coupled flux ϕ_{cp} . Thus the induced voltage is increased.

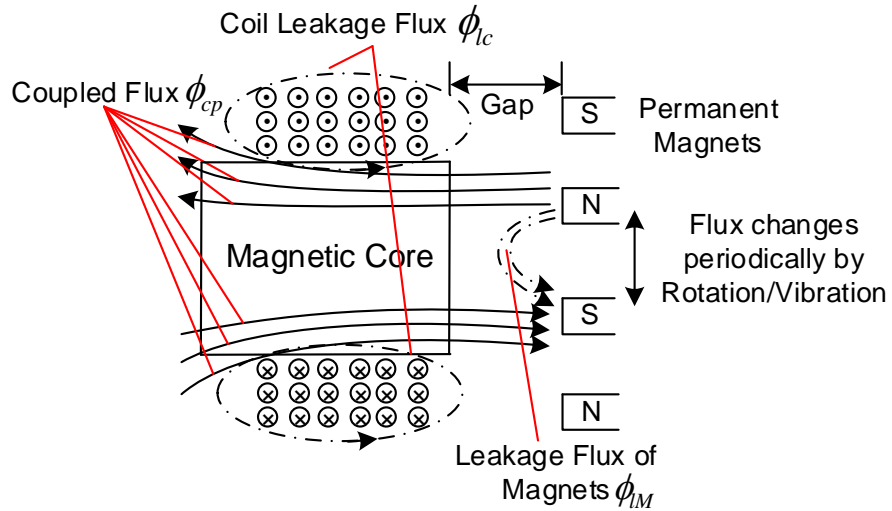


FIGURE 2.3: Inductive magnetic energy harvesters in equilibrium.

Both the rotational and vibrational inductive magnetic harvesters are often modeled as spring mass damper systems [19, 20] (Fig. 2.4), with the fact that the proof mass m in vibration is replaced by the moment of inertia I in rotation. The behavior of the system can be described as $m\ddot{x} + c\dot{x} + kx = -m\ddot{y}$, where x is the displacement between the proof mass and the base, y is the displacement of the base, c is the damping coefficient, k is the stiffness and m is the proof mass [19, 20]. The conventional RLC equivalent model is thus derived. It can be seen from Fig. 2.4, that each electrical parameter in the equivalent circuit model represents one or more mechanical characteristics of the harvester: inductor for proof mass, capacitor for stiffness, resistor for damping coefficient, etc. This model has its own limitations. The equivalent spring is considered as linear; however, this

hypothesis is valid only when the displacement of the harvester mass is negligible or very small. Furthermore, this model is purely mechanical. The effect of the electromagnetic field is not considered.

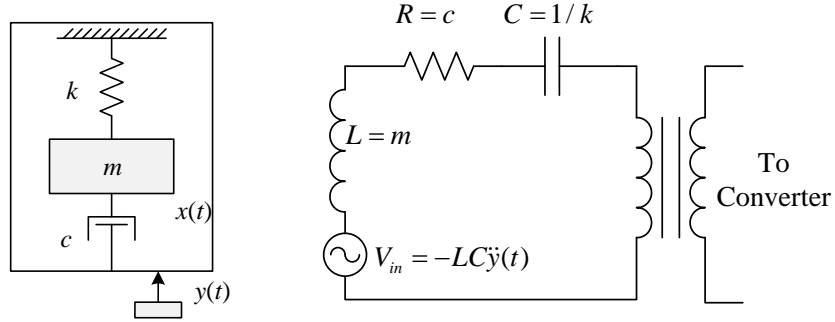


FIGURE 2.4: The spring mass damper system and conventional equivalent circuit.

The most simplified electrical circuit model for a rotation or vibration inductive magnetic harvester is to treat it as an ideal AC voltage source, assuming the mechanical movement and the magnetic coupling are both ideal [12, 22]. The model tends not to be accurate when it is applied to a real harvester due to the assumption of 100% energy efficiency. Since the magnetic reluctance of any magnetic core cannot reach zero, the flux variation generated from rotation cannot be fully coupled with the coil. Therefore, there is kinetic energy dissipated with the leakage flux into the air. In order to reduce the error, several approaches intend to correct the result by including non-linear effect of the mechanical movement and magnetic field [21, 22]. However, none of these approaches derive an electrical circuit model, and this is essential to aid the converter design. An AC-DC converter is needed for a magnetic harvesting system in order to convert the low AC voltage from the

harvester device to the stable DC output voltage. When the AC-DC converter is attached to the harvester device, the system efficiency and output power are also affected by the converter circuit. In this case, an equivalent circuit model of the harvester device is necessary to analyze the harvester device along with the converter circuit.

2.2 Inductive Magnetic Harvester Modeling

This research proposes a step-by-step modeling methodology to design an equivalent circuit model for an inductive magnetic harvester (Fig. 2.5). The magnetic circuit and electrical circuit model are built based on the electromagnetic theory. With the procedure given in Fig. 2.5, the parameters of the magnetic harvester can be designed and tuned according to the requirements of the AC-DC converter design. There are two ways to estimate the parameter values of the electrical circuit model—one from finite element analysis (FEA) simulation and the other from a proposed experimental measurement procedure. The FEA analysis can be used to design or estimate the electrical performance of the magnetic harvester before it is built, but it is more time consuming compared to the experimental measurement. The experimental measurement is used to aid the design of the AC-DC converter design to achieve high energy efficiency of the system. It can also be used to verify the FEA simulation results.

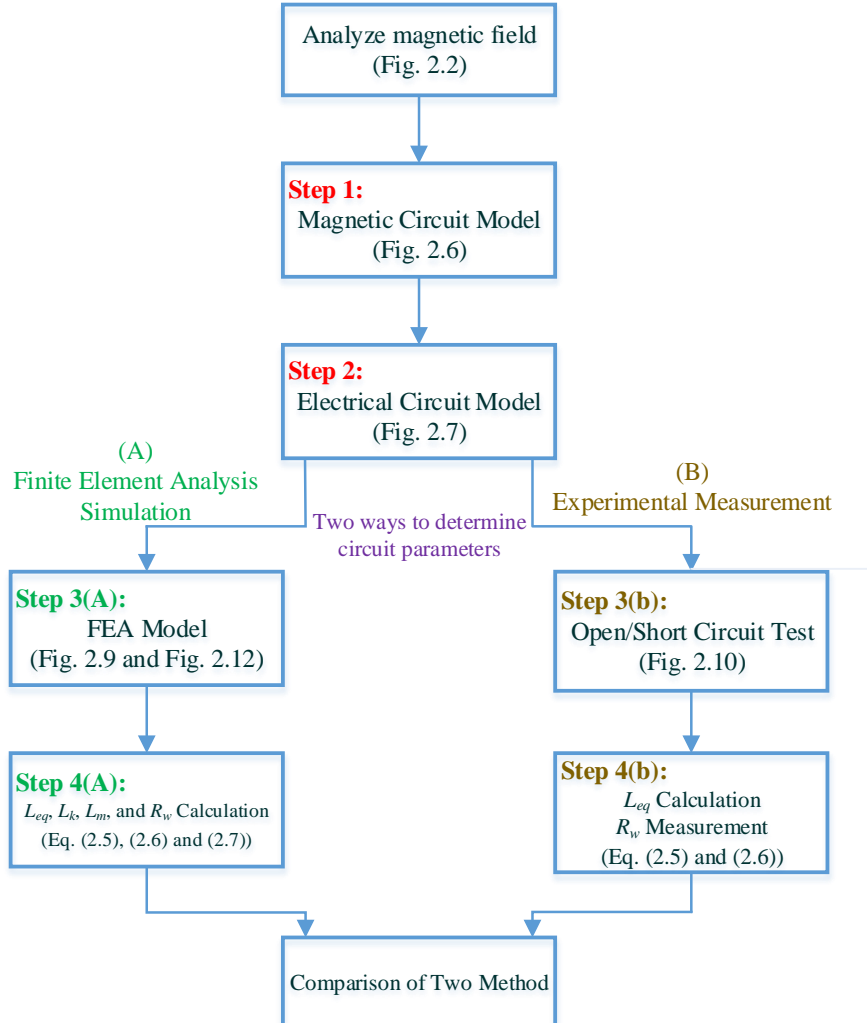


FIGURE 2.5: The step by step modeling methodology to design a equivalent circuit.

2.2.1 Magnetic Circuit Model (*Step 1*)

The magnetic circuit model for one coil and one magnet is proposed in Fig. 2.6 based on the harvester shown in Fig. 2.3 [31, 32]. The leakage flux ϕ_{LM} leaks through the air with the air magnetic reluctance \mathfrak{R}_{LM} . The coupled flux goes through the magnetic reluctance of the air gaps on the North and South poles of

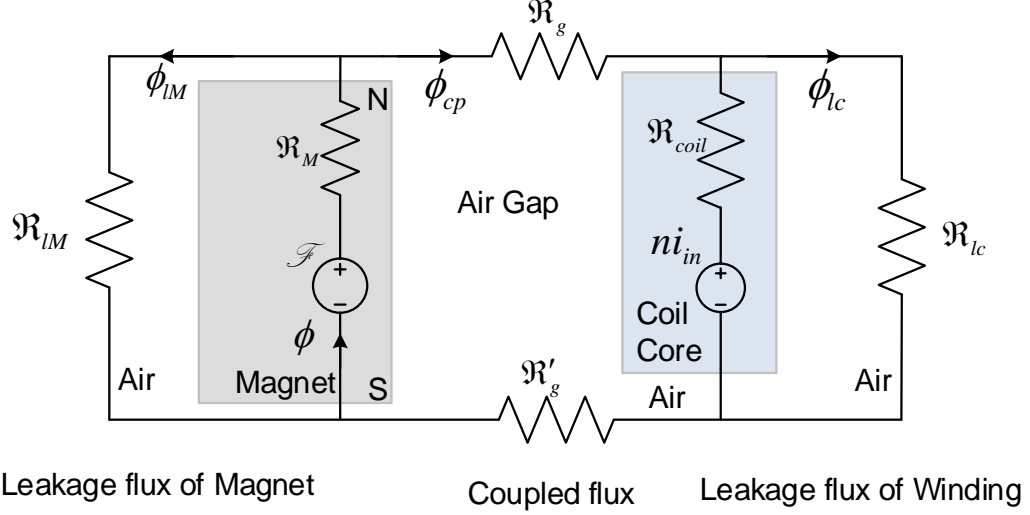


FIGURE 2.6: The magnetic circuit model.

the magnet \mathfrak{R}_g and \mathfrak{R}'_g , respectively, and magnetic reluctance of the coil \mathfrak{R}_{coil} .

The leakage flux of the coil winding ϕ_{lc} is much smaller compared to the coupled flux ϕ_{cp} due to large magnetic reluctance through air \mathfrak{R}_{lc} , so it is ignored. By ignoring \mathfrak{R}_{lc} , the coupled flux can be combined as the coupled reluctance.

$$\mathfrak{R}_{cp} = \mathfrak{R}_g + \mathfrak{R}_{coil} + \mathfrak{R}'_g \quad (2.1)$$

More flux through the coil can be attracted if \mathfrak{R}_{cp} is minimized. \mathfrak{R}_g is significantly affected by the air gap, the distance between the magnets and the coil. The air gap could be made as small as possible in order to minimize \mathfrak{R}_g and leakage flux so in order to maximize the energy transfer efficiency. For air-core magnetic harvesters, since the magnet is normally inserted to the coil, adjusting the air gap between the coil winding and the magnet is still valid, though the direction of adjustment between coil and magnet changes from perpendicular to horizontal. Later in this

research we will show that the harvester can be followed by a boost derived converter, which utilizes the harvester coil equivalent inductance to enhance or replace the input boost inductance. However, the magnetic reluctance and flux are the non-linear parameters that cannot easily be used in electrical circuit analysis, so an equivalent electrical circuit model will be introduced in the following part.

2.2.2 Electrical Circuit Model (*Step 2*)

In order to analyze the harvester with any converter circuit followed, the equivalent electrical circuit model is derived from the magnetic circuit model (Fig. 2.7). In the analysis, \mathfrak{R}_{lc} is assumed to be large so that ϕ_{lc} can be ignored. Suppose the induced voltage is v_s , we have

$$\begin{cases} \mathcal{F} - \phi \mathfrak{R}_M = \phi_{cp} \mathfrak{R}_{cp} + n i_{in} & \text{and } v_s = n \frac{d\phi}{dt} \\ \mathcal{F} - \phi \mathfrak{R}_M = \phi_{lM} \mathfrak{R}_{lM} \end{cases} \quad (2.2)$$

$\phi = \phi_{cp} + \phi_{lM}$ Flux from magnet

ϕ_{cp} Coupled flux of magnet and coil

ϕ_{lM} Flux generated from the magnet

i_{in} Harvester current to the output

Suppose $\mathcal{F} - \phi \mathfrak{R}_M = n i_s$, yields

$$v_s = n^2 \frac{1}{\mathfrak{R}_{lM}} \frac{di_s}{dt} + n^2 \frac{1}{\mathfrak{R}_{cp}} \frac{d(i_s - i_{in})}{dt} = L_k \frac{di_s}{dt} + L_m \frac{di_m}{dt} \quad (2.3)$$

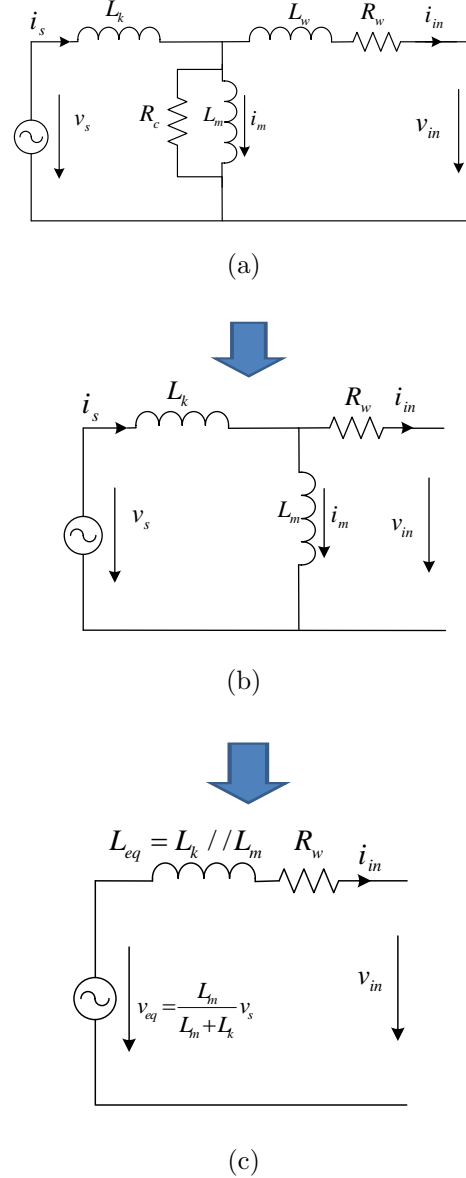


FIGURE 2.7: Equivalent model of inductive magnetic energy harvester.

where L_k is the leakage inductance, L_m is the magnetizing inductance. The equivalent circuit in Fig. 2.7(b) is simplified to Fig. 2.7(c) using Thevenin's theorem.

$$\begin{cases} v_{eq} = \frac{L_m}{L_k + L_m} v_s \\ L_{eq} = L_k // L_M = n^2 \frac{1}{\mathfrak{R}_{lM} + \mathfrak{R}_{cp}} \end{cases} \quad (2.4)$$

It is shown from (2.4), the equivalent inductance of the harvester is directly proportional to the square of turns n^2 and inversely proportional to the magnetic reluctance $\mathfrak{R}_{lM} + \mathfrak{R}_{cp}$. The magnetic reluctance \mathfrak{R}_{lM} and \mathfrak{R}_{cp} are difficult to calculate even in FEA simulation. However, they are related to several parameters such as permeability of magnet and core material, size of magnet and core, and air gap between magnet and core. Higher permeability of the core material and smaller air gap lead to higher equivalent inductance due to lower magnetic reluctance.

R_w in series with L_{eq} represents winding resistance as shown in Fig. 2.7(c). In order to increase the output voltage of the harvester, the harvester winding usually is made up of large number of turns. Thus, generally, the winding resistance cannot be ignored, and it is a crucial parameter affecting the efficiency of the harvesting system. R_w is decided by the conductivity of the material, cross-section area of the conductor and turns of the coil. If the coil size if fixed, roughly, R_w is directly proportional to the square of turns n^2 . The harvester output voltage is directly proportional to number of turns n . Increasing turns leads to higher output voltage. However, because $R_w \propto n^2$, theoretically, the maximum available power is still the same. The output voltage, equivalent inductance, winding resistance and harvester size should all be balanced in the harvester design.

Since the magnetic core is highly permeable, the core is subject to core loss. In Fig. 2.7(a), a resistor R_c in parallel with L_m represents eddy current loss and

hysteresis loss. Compared to L_m and L_k , the effect of core loss is negligible. Thus, R_c is neglected in subsequent analysis.

2.2.3 Finite Element Analysis (FEA) Simulation

In order to build the correlation between the harvester mechanical design and electrical performance to aid the converter design, it is necessary to analyze the magnetic field with FEA simulation. With the FEA model, the parameter values of the electric circuit model can be tuned by changing the mechanical design. The value of L_{eq} is also a vital parameter that affects converter power loss. FEA simulation is used to estimate the value of harvester equivalent inductance.

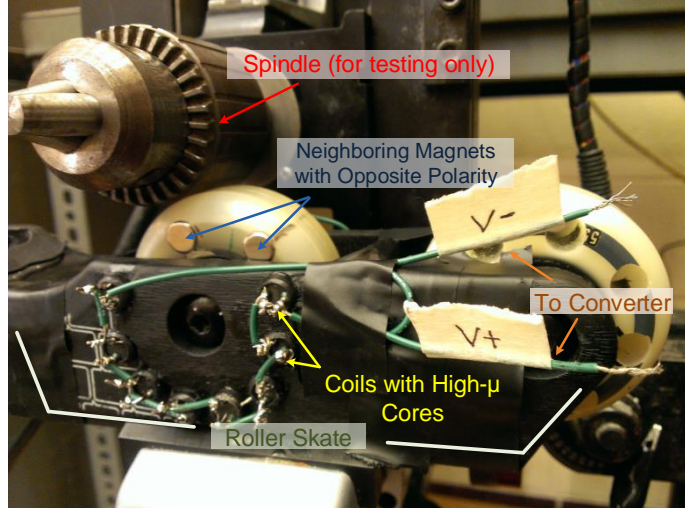


FIGURE 2.8: Rotational magnetic harvester.

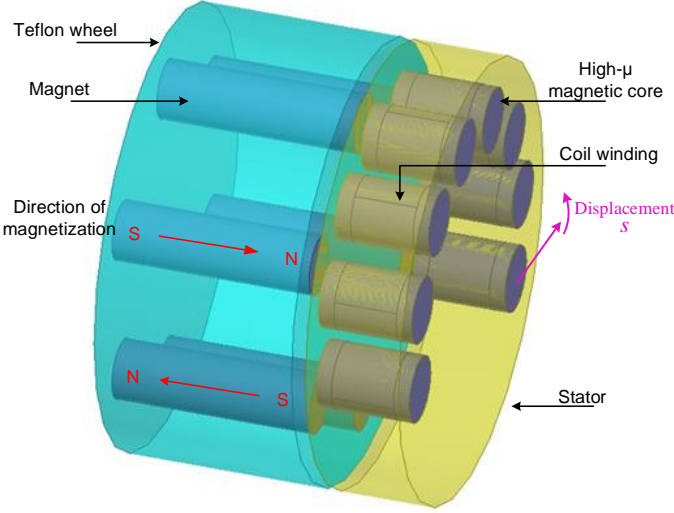


FIGURE 2.9: FEA simulation of inductive magnetic harvester.

2.2.3.1 FEA model (*Step 3(A)*)

The proposed rotational inductive magnetic energy harvester is built in a roller skate with the parameters in TABLE 2.1 (Fig. 2.8). The FEA model is built with ANSYS/Maxwell3D based on the proposed magnetic harvester (Fig. 2.9). It contains 6 identical NdFeB N42 magnets placed inside the Teflon wheel in alternate positions separated by 60 degrees. The neighboring magnets are arranged to have opposite polarities of magnetization from each other, where ‘N’ is the North and ‘S’ is the South Pole. An alternating magnetic field is generated when the magnets pivot on the axis of the Teflon wheel. The eight inductor coils mounted on the stator are divided into two windings, each with four coils in series. The experimental and simulation results in Section 2.2.3 and 2.2.5 are based on four coils in series. The harvester output voltage and the coil winding inductance L_{coil} can be measured at the output interface of each winding.

TABLE 2.1: Parameters of proposed magnetic harvester

Parameters	Value
Maximum rotation speed	~2200RPM
Air-gap	2mm
Magnet height	25.4mm
Magnet diameter	7.6mm
Number of coil turns	~180
Winding resistance	4.7Ω
Wheel thickness	25.4mm
Wheel diameter	56mm

2.2.3.2 L_{eq} Calculation (Step 4(A))

The data from simulation is processed in this section to calculate harvester equivalent inductance L_{eq} . Open circuit voltage $v_{in(OC)}$ and short circuit current $i_{in(SC)}$ data are collected at different air gap values. As shown in Fig. 2.10, under open circuit condition:

$$v_{eq} = v_{in(OC)} \quad (2.5)$$

And under short circuit condition, the winding resistance R_w becomes the load:

$$i_{in(SC)} = \frac{v_{eq}}{R_w + j\omega L_{eq}} \quad (2.6)$$

The equivalent inductance of the harvester is calculated from (2.5) and (2.6). The winding resistance R_w is measured from the experimental setup. In the simulation, the open circuit voltage $v_{in(OC)}$ and short circuit current $i_{in(SC)}$ are close to sinusoid waveform. The RMS values of the open circuit voltage and short circuit current are calculated from FEA simulation results. Given RMS value of harvester open circuit

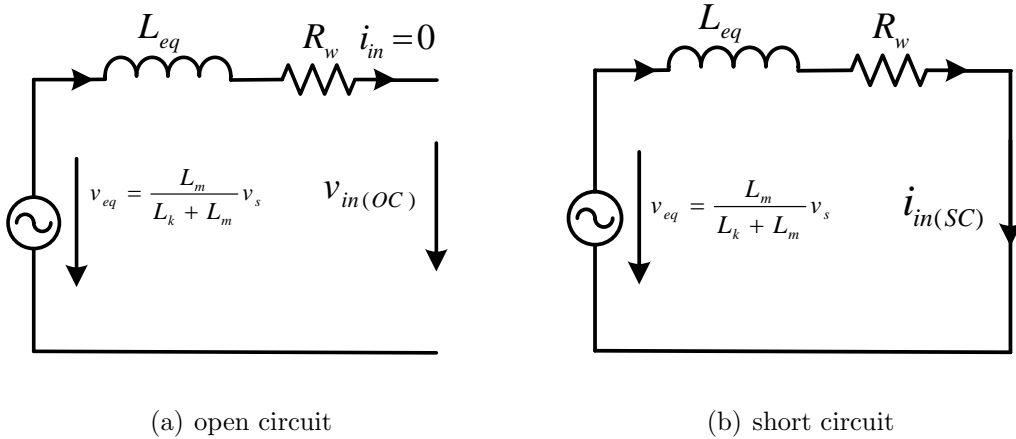


FIGURE 2.10: Open and short circuit of harvester.

voltage, short circuit current and winding resistance, the equivalent inductance L_{eq} is thus solved with (2.5) and (2.6). As shown in Fig. 2.11, the equivalent inductance drops with the air gap. According to (2.4), the equivalent inductance is inversely proportional to the magnetic reluctance $\mathfrak{R}_{lM} + \mathfrak{R}_{cp}$. The magnetic reluctance is a function of geometry of the magnetic path. When the air gap between the magnet and coil core is reduced, the magnetic reluctance decreases. As shown in Fig. 2.11, the inductance drops fast in this region when the air gap is less than 1mm. When the air gap is large, the effect of air gap variation is reduced and the equivalent inductance becomes stable. In the test result, it maintains a stable value around 5.6mH when the air gap is larger than 1mm. It should be noted that, when the air gap is small, the coil core works closer to the saturation region. That effect leads to inductance reduction. Which effect is dominant depends on the coil core material, air gap between the magnet and the coil core, and the strength of the magnetic field. The results show that the magnetic reluctance reduction effect

dominates in the proposed system when the air gap is larger than 0.3mm.

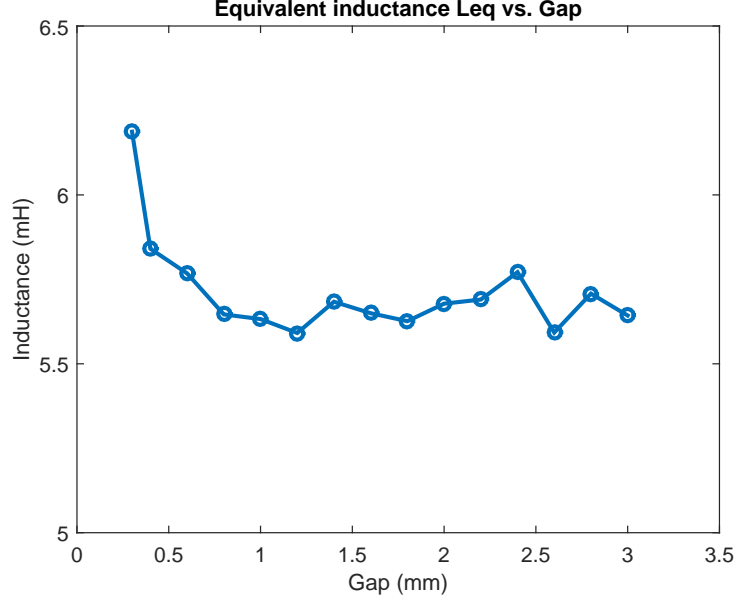


FIGURE 2.11: Equivalent inductance L_{eq} vs. Air gap derived using FEA simulation.

2.2.4 L_k and L_m (Step 4(A))

The leakage inductance L_k and magnetizing inductance L_m are hard to determined by its magnetic reluctance in (2.3). Instead, they are estimated by the flux variation. In the open circuit condition, when $i_{in} = 0$,

$$\frac{L_k}{L_m} = \frac{n^2 \frac{1}{\mathfrak{R}_{lM}}}{n^2 \frac{1}{\mathfrak{R}_{cp}}} = \frac{\frac{n\phi_{lM}}{i_s}}{\frac{n\phi_{cp}}{i_s}} = \frac{\phi_{lM}}{\phi_{cp}} \quad (2.7)$$

From Fig. 2.3, the flux from magnets is $\phi_M = \phi_{lM} + \phi_{cp}$. Solving ϕ_{cp} and ϕ_{lM} is equivalent to solving ϕ_M and ϕ_{cp} . At each position of s , the simulation result

provides a corresponding flux distribution. Fig. 2.12 shows the flux density in the magnets and coil cores at air gap=2mm when the magnet is facing the coil core. Under open circuit condition, the flux from the magnets ϕ_M is measured from the integration of the flux density on the surfaces of the magnet when the magnet is facing the coil core as shown in Fig. 2.12 ($s = 0^\circ$). And coupled flux can be calculated from the flux linkage λ of the coil given by FEA simulation.

$$\phi_{cp} = \frac{\lambda}{n} \quad (2.8)$$

ϕ_M and ϕ_{cp} data is collected by taking average at each position when the magnet and the coil is facing each other ($s = 0^\circ$, 60° and 120°). Given (2.7) and

$$L_{eq} = \frac{L_k L_m}{L_k + L_m} \quad (2.9)$$

L_k and L_m can be estimated from solved L_{eq} value in Section 2.2.3.2 (Fig. 2.13). When the air gap increases, the leakage flux ϕ_{lM} increases and the coupled flux ϕ_{cp} decreases. According to (2.7), the ratio of leakage inductance and magnetizing inductance L_k/L_m increases. Meanwhile, the value of equivalent inductance L_{eq} is stable from 0.3mm to 3mm air gap (Fig. 2.11). So the leakage inductance L_k increases with air gap and the magnetizing inductance decreases with the air gap. The simulation results shown in Fig. 2.13 verifies the analysis.

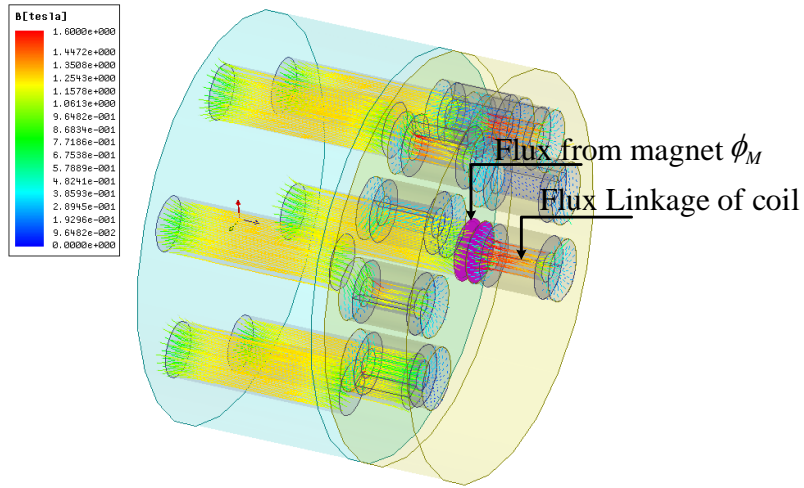


FIGURE 2.12: The flux density in magnets and coil cores (Gap=2mm).

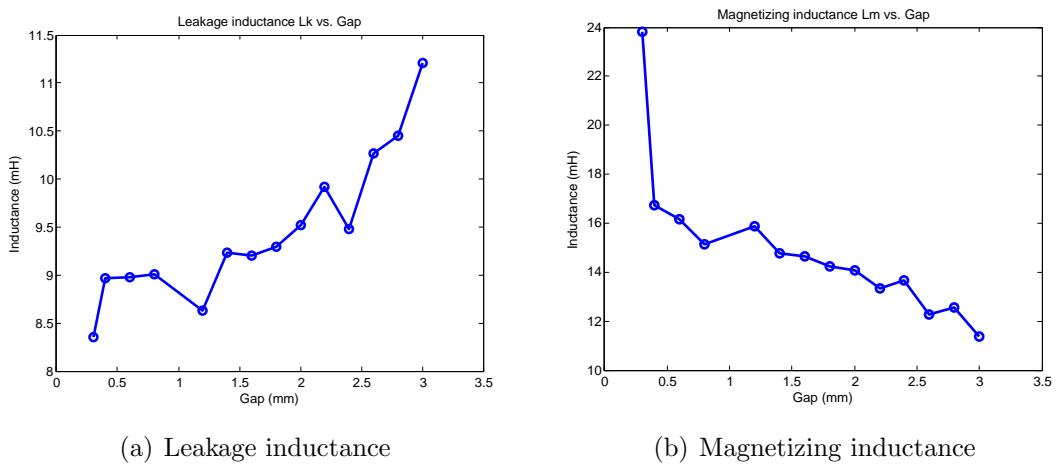


FIGURE 2.13: Leakage and magnetizing inductance with gap.

2.2.5 Experimental Measurement

The circuit parameters of the harvester model can also be estimated by the experimental measurement if the harvester device has been built (Fig. 2.5). Compared to the FEA simulation, the experimental measurement method is less time consuming, but it cannot be applied before the harvester is built. It can also be used to verify the result of the FEA simulation. For the experimental harvester system

in Fig. 2.8, open and short circuit tests are applied to the harvester under several frequencies to estimate the equivalent inductance L_{eq} , with the experimental setup shown in Fig. 2.10. R_w is 4.7Ω measured from the output interface of the winding.

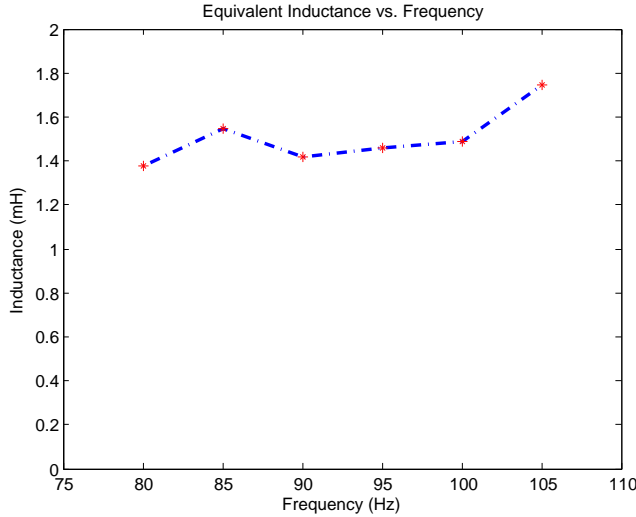


FIGURE 2.14: Experimentally measured L_{eq} vs. Frequency (Air gap = 2mm).

Thus, the unknown parameter L_{eq} can be calculated under each fixed frequency following (2.5) and (2.6) with the RMS value of open circuit voltage and short circuit current. The measured equivalent inductance of the harvester is around 1.5mH as shown in Fig. 2.14. However, the equivalent inductance calculated from simulation is around 5.6mH. The main reason that may cause the difference is the permeability of the materials. The relative permeability of the coil core and permanent magnet used in the simulation are 1000 and 1.05, respectively. The actual values are in a rough range. The relative permeability of the ferrite material may be as low as 640 and the relative permeability of permanent magnet may vary from 1.01 to 1.05. It is possible that the actual permeability of the core and magnet material in the experimental setup is lower than the simulation

values. Lower relative permeability leads to higher magnetic reluctance and lower equivalent inductance.

2.2.6 Clarification and Correction of Preliminary Research

This section clarifies the incorrect assumptions and models that were previously proposed in the preliminary research [31, 32]. In the preliminary research, the same magnetic circuit model and electrical circuit model were proposed as shown in Fig. 2.6 and Fig. 2.7. The leakage inductance was calculated by (2.7) from magnetic inductance L_m , which was assumed to be a fixed value in [32]. With this inaccurate assumption, the leakage inductance L_k is calculated. When the air gap changes from 0.5mm to 3mm, L_k changes from 0.2mH to 11.5mH. However, with L_m constant and $L_{eq} = L_m//L_k$, this implies L_{eq} increases with the air gap in the preliminary research [31, 32], which is not valid. This thesis corrects this inaccuracy in Section 2.2.3 and 2.2.4. In fact, Fig. 2.11 demonstrates that L_{eq} initially decreases when the gap increases from a very small value, and then it holds relatively constant value. This is because L_m is not constant but is increasing with gap, as shown in Fig. 2.13(b).

Because preliminary research assumed L_m constant with air gap, this led to the incorrect conclusion that there was an optimal air gap that maximized the harvester system output power when the AC-DC conversion efficiency calculations were included in the system efficiency calculations.

However, as shown in Fig. 2.13(b) and Fig. 2.11, L_m decreases and L_{eq} is relatively stable over the air gap range 0.5mm to 3mm. Therefore, there should be no design trade off needed between air gaps (in this range) and overall system efficiency, as reported in preliminary research [31, 32].

2.3 Conclusion and Comparison between FEA and Experimental Modeling Approach

In this chapter, a step-by-step procedure is developed to build an equivalent circuit model for magnetic energy harvester. The new model is based on the electromagnetic theory. The FEA simulation is employed to build an equivalent method. The results are compatible with the experimental measurements. The model represents the harvester by an equivalent electric circuit with an AC voltage source in series with an equivalent inductance and resistance. This model will subsequently be used in Chapter 3 and Chapter 4 to design AC-DC harvesting electronics and their maximum power point tracking controllers.

Chapter 3

AC-DC Power Conversion for Magnetic Energy Harvester

This chapter first reviews several typical approaches and introduces new topologies to optimize the performance of an inductive magnetic energy harvesting system. A number of AC-DC energy conversion circuits have been reported for low power applications [1–5, 11–17, 23–27, 33–35]. The conventional approaches normally use diode bridge rectifier as the first stage and a DC-DC converter as the second stage [1, 2]. This approach has low efficiency due to high diode voltage loss considering low input voltage of most energy harvesters. Other approaches improve the converter efficiency by getting rid of the diode bridge rectifier as the first stage [3–5, 11–15]. New approaches will be introduced in this chapter based on the

summary of the typical approaches. The main research contributions presented in this chapter are:

- A literature survey of typical topologies designed for low voltage and low power energy harvesting applications is presented. The benefits and limitations of these approaches are fully evaluated.
- A new family of low threshold capacitive rectifier topologies are introduced that are specially designed for inductive magnetic harvesting. By adding one resonant capacitor and one bi-directional switch, the proposed rectifiers can harvest much higher energy compared to the conventional diode bridge rectifier. The topology is simple to implement and low cost.
- A center tapped boost-derived AC-DC converter which utilizes the harvester internal inductance is proposed. The high switching frequency boost converter is able to extract more energy from the harvester compared to the resonant rectifier. It is also compatible with maximum power point tracking algorithms presented in Chapter 4. The models from Chapter 2 are utilized to demonstrate that no external inductor is needed for the boost derived topology. The experimental results shows 89% system efficiency compared to the state of the art converter (50% in [11])

3.1 Literature Review

3.1.1 Conventional Rectifier

Conventional power converters for energy harvesting normally consist of two stages: a diode bridge rectifier for the first stage and a capacitor/battery/DC-DC converter for the second stage (Fig. 3.1) [1, 2].

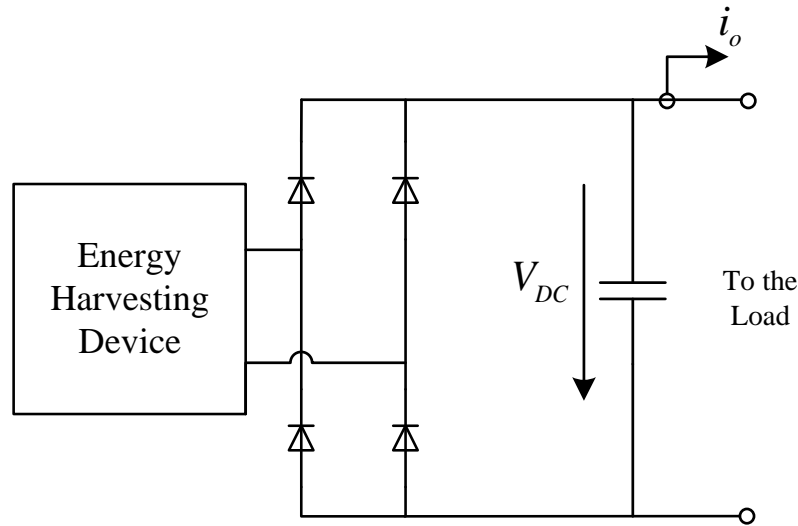


FIGURE 3.1: Conventional power converter.

For low input voltage applications, there are major disadvantages of two stage topologies. The output voltage of energy harvester is typically several hundred millivolts. Even with Schottky diode, there is still $\sim 0.3V$ voltage drop. For input voltage lower than 1V applications, diode bridge rectifier is not feasible. Even though the input voltage can drive diode bridge rectifier, the voltage drop in rectification will cause large amount power loss. That will significantly lower the

power conversion efficiency. Therefore, the conventional power converter made of a diode bridge rectifier as the first stage is often not suitable for energy harvesting devices.

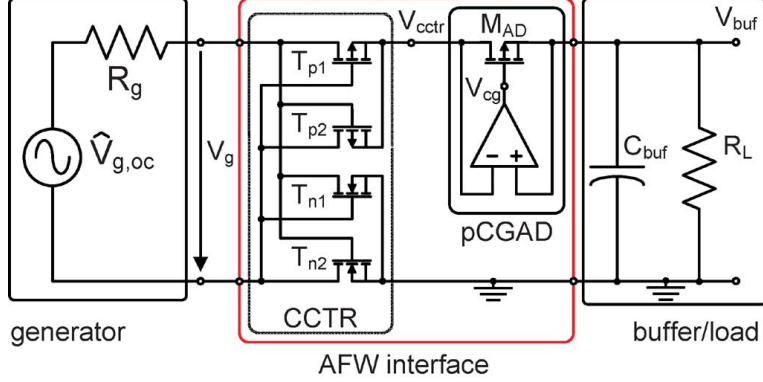


FIGURE 3.2: Active full wave rectifier.

Several variations of the conventional rectifier improves the power conversion efficiency by using MOSFETs or active diodes to replace the bridge diodes [18, 23, 28, 29, 36–38]. Normally these approaches requires external driver for the MOSFETs [18, 23, 28, 29, 37]. One typical approach called active full-wave rectifier is introduced in [36] (Fig. 3.2), which avoids to use external power supply by driving the MOSFETs with the AC input voltage. As shown in Fig. 3.2, four rectifier diodes are replaced by four MOSFETs and the harvester voltage is connected to the gate to drive the MOSFETs. This structure avoids the diode forward voltage drop without extra gate driver circuit so that it increases the power conversion efficiency and achieves self start-up. However, considering most of the low gate voltage MOSFETs require 1.8VDC to 2.5VDC for normal function, the MOSFETs may not be turned on or has huge $R_{DS(on)}$ if the harvester voltage is lower than

1.8V, which leads to low power conversion efficiency or even zero output power. Other approaches are reported to solve the problem by avoiding to use bridge rectifier as the first stage to increase the power conversion efficiency.

3.1.2 Piezoelectric AC-DC rectifiers (SSHI circuit)

One approach has recently been proposed to overcome the deficiency of conventional two stage power conversion called Synchronized Switch Harvesting on Inductor (SSHI) [3–5] for the piezoelectric energy harvester. This topology adds one bi-directional switch and an inductor in parallel or in series (Fig. 3.3 Series SSHI) with the conventional converter.

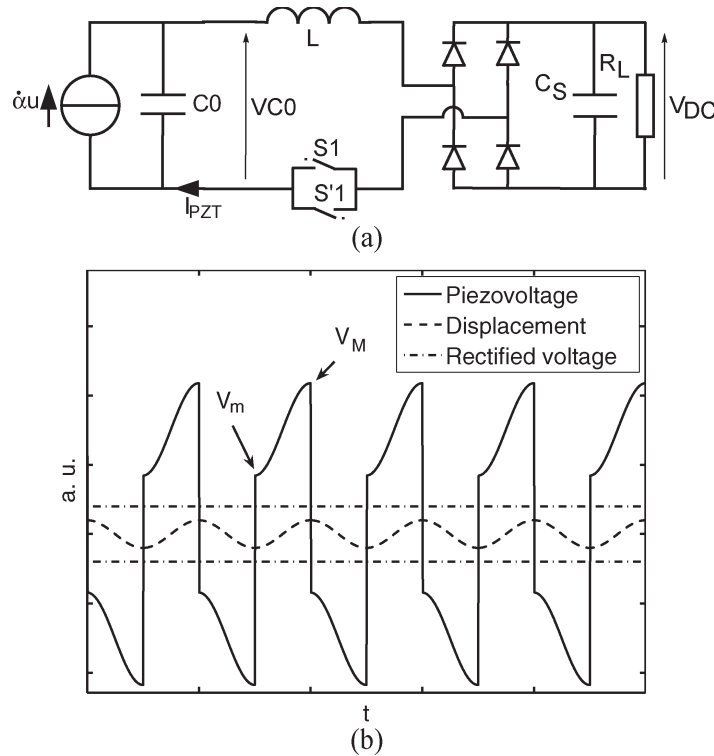


FIGURE 3.3: Series SSHI circuit [5].

A piezoelectric element is typically modeled as a sinusoid current source in parallel with a capacitor (Fig. 3.3). The bi-directional switch is triggered when the displacement reaches its extreme point. The resonant inductor resonates with the piezoelectric capacitor and the piezoelectric voltage decreases. After half of the resonant period, the bi-directional switch turns off and the resonance between the inductor and the piezoelectric capacitor stops. In the reverse direction, the piezoelectric voltage continues increasing as the displacement changes direction.

SSHI circuits have benefits: 1. The piezoelectric voltage is always increasing except for short resonant duration, which increases the conduction time of the rectifier; 2. The piezoelectric voltage always has the same sign as the current, in other words, the direction of displacement. The power (product of voltage and current) will always be positive [5]. The major drawback of this approach is that it can only work at the vibration frequency of the piezoelectric element, and generally this frequency is significantly lower than typical working frequency of switching devices. Lower frequency requires larger passive components, which severely increases the converter size. Especially for series SSHI circuit, which requires even larger inductor to get better result.

3.1.3 Boost Derived AC-DC Converters

Since the magnetic energy harvester is inductive, a number of approaches consider to use the built-in inductor of the harvester to reduce the converter size. With

an inductor at the input, boost converter topology is feasible to convert the low voltage (AC voltage around 1VRMS) of the magnetic harvester to a useful voltage level (typically from 1.8 to 3.3VDC) without increase the converter size [11–15]. An example of boost derived AC-DC converter is shown in Fig. 3.4 [11]. The converter includes one bi-directional switch by connecting two n-MOSFETs in reverse directions (Fig. 3.4(b)). A diode bridge rectifier is used instead of the output diode of the basic boost topology to convert AC input voltage to DC voltage. The operation principle of the boost derived converter is similar to a basic boost converter in each positive or negative AC voltage cycle.

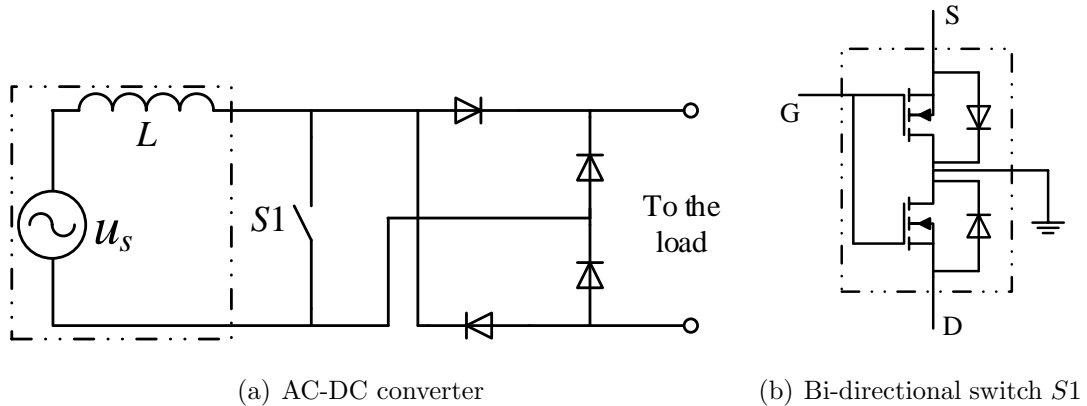


FIGURE 3.4: Boost derived AC-DC converter.

The benefits to use the boost derived AC-DC converter topology is apparent:

1. They may use the harvester internal inductance to reduce converter size and achieve high step-up conversion ratio;
 2. High switching frequency is achievable which may reduce the size and rating of possible passive components [13, 15];
 3. The control and drive circuit is easy to design and implement (fixed duty ratio).
- But although the power conversion circuit is made an integrated part of the

harvester with the shared inductor, these approaches are designed separately from the harvester design. As the shared component, the harvester internal equivalent inductance is of great importance for both harvester efficiency and converter power loss, which is arbitrarily defined as the coil inductance in the previous works [11].

3.1.4 Summary

With the goal of designing a AC-DC converter that can extract maximum useful energy out from the magnetic harvester, the approaches mentioned above are carefully studied. The features and drawbacks of the reviewed converters are listed in Table 3.1. Based on the analysis, there is a need for research to create new energy harvesting circuits that:

1. avoids using diode bridge rectifier as the first stage;
2. makes use of the harvester internal built-in inductance to reduce the converter size;
3. optimizes the maximum energy harvested from the entire system, including both the harvester and the AC-DC converter. It should not try to separately optimize the converter or the magnetic harvester;
4. is able to track the maximum power or use other method to enhance the power extracted from the magnetic harvester;
5. have high working frequency to reduce the value of the passive components;

TABLE 3.1: Summary of the AC-DC power conditioning circuit

	Structure	Features	Drawbacks
Conventional rectifier [1, 2]	Consisted of two stages: a diode bridge rectifier and a capacitor	Circuit design is simple to implement.	The conversion efficiency is low due to the voltage drop on the rectification stage.
SSHI circuit [3–5]	Adds one bi-directional switch and an inductor in parallel or in series with the conventional converter.	<p>The efficiency is enhanced by:</p> <ul style="list-style-type: none"> • Power transfer time is increased; • The input voltage and the current always has the same sign. 	<ul style="list-style-type: none"> • Low frequency & Large passive component; • High side driver needed; • Applicable to piezoelectric harvesters.
Boost derived converter [11–15]	Consists of a bi-directional switch before a bridge rectifier.	<ul style="list-style-type: none"> • The harvester internal inductance is used; • High switching frequency & Low passive components; • Simple control and drive circuit design. 	<ul style="list-style-type: none"> • Harvester and converter design are separated; • No maximum power transfer.

6. have low side switches are used to simplify the drive circuit;
7. have simple control algorithm.

The preferred solution for the magnetic harvester needs to meet as many requirements listed above as possible to reduce the converter size and increase the net energy out of the magnetic harvester. However, there are conflicts among some of

the requirements. For example, if maximum power transfer tracking control is applied, the control algorithm becomes more complicated. The design goal becomes to balance these requirements.

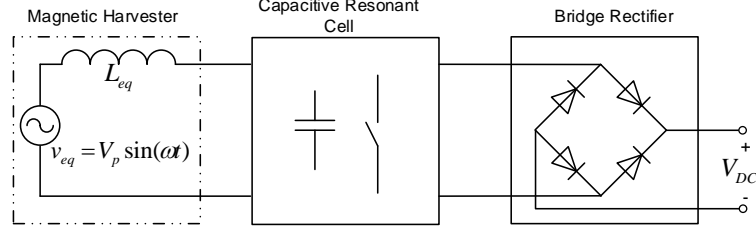
3.2 Capacitive Rectifier Based on Synchronized Switch Harvesting Technique

This research proposes a new family of low threshold capacitive rectifiers for inductive magnetic harvester extending the “Synchronized Switch Harvesting” (SSH) technique [39] to become applicable to inductive magnetic energy harvesters. With one resonant capacitor and one bi-directional switch, the proposed rectifiers can harvest higher energy than conventional diode bridge rectifier by adding the high voltage or current generated by the resonance between the resonant capacitor and the harvester internal equivalent inductor. Thus, the proposed circuit can operate with magnetic harvesters that have low output voltage. The experimental results are provided to verify the theoretical predictions.

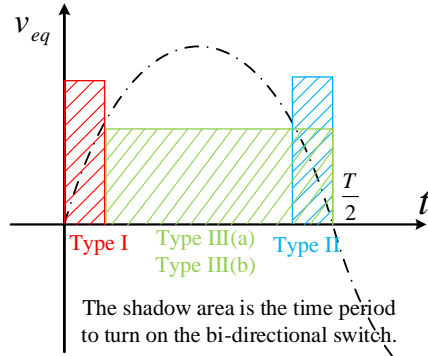
3.2.1 A Family of SSH Capacitive Rectifiers

Fig. 3.5 shows the proposed capacitive rectifier. The inductive magnetic harvester is modeled as a voltage source in series with an internal equivalent inductor as derived in Fig. 2.7(c) [31, 32]. One capacitive resonant cell is inserted between

the inductive magnetic harvester and the conventional diode bridge rectifier. The resonant cell consists of one capacitor and one bi-directional switch. There are several combinations of capacitor and switch pairs. Based on these combinations, four new capacitive rectifiers are generated as shown in Fig. 3.6.



(a) Schematic of capacitive rectifiers



(b) The

FIGURE 3.5: Proposed capacitive rectifier and its control scheme.

Referring to Fig. 3.6, the new rectifiers use the resonance between the harvester internal equivalent inductance L_{eq} and the resonant capacitor C_r to generate a high voltage or current at a certain phase angle of the harvester input voltage (Fig. 3.5(b)). For the Type I rectifier, the bi-directional switch $S1$ is triggered at $t = 0$. During the resonant period, the resonant capacitor C_r is charged to its maximum voltage. Then the switch $S1$ is turned off and the voltage before rectifier is increased by adding V_{C_r} . The Type II and Type III rectifier work under similar

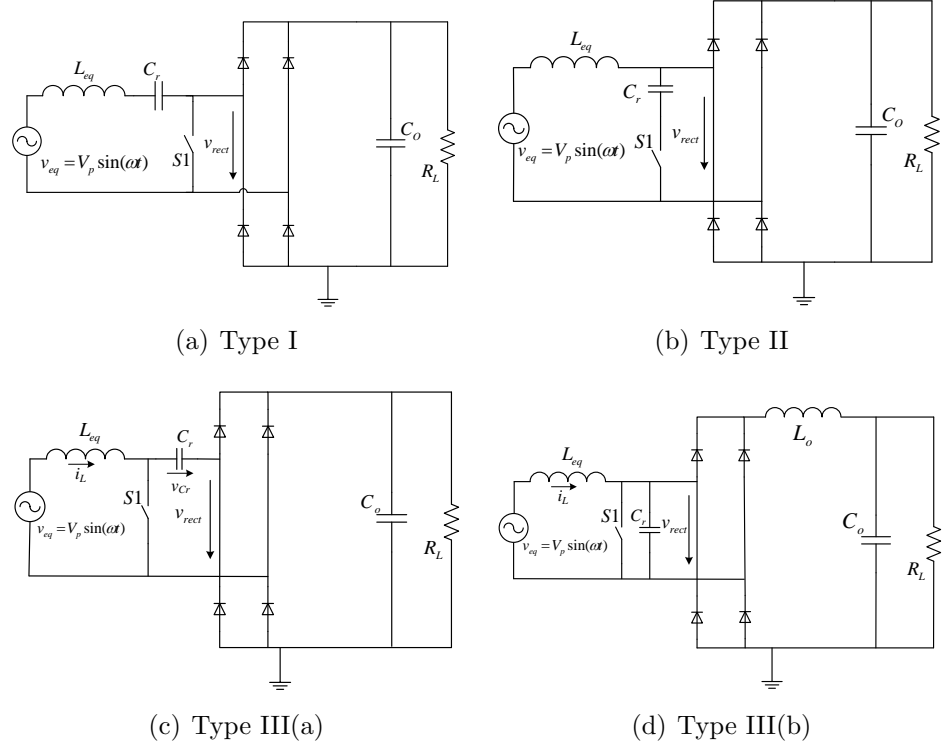


FIGURE 3.6: New family of ultra-low threshold capacitive rectifiers.

principle. For Type I and II, the switching time period t_r is approximately half the resonant period of resonant capacitor C_r and the input equivalent inductor L_{eq} .

$$\text{Type I \& II: } t_{r,I\&II} = \pi \sqrt{L_{eq}C_r} \quad (3.1)$$

And the switching time for Type III converter is

$$\text{Type III: } t_{r,III} = \frac{T}{2} - \pi \sqrt{L_{eq}C_r} \quad (3.2)$$

where T is the period of the input harvester voltage. Due to the fact that the input voltage is not a constant, the actually switch conducting time is a little lower than

$$\pi\sqrt{L_{eq}C_r}.$$

3.2.2 Synchronized Switch Harvesting on Resonant Capacitor

3.2.2.1 Conventional Rectification

Conventional power rectifier for energy harvesting normally consist of two stages: a diode bridge rectifier for the first stage and a capacitor filter for the second stage (Fig. 3.7(a)). As shown in Fig. 3.7(b), before the rectifier input voltage v_{rect} reaches $V_{DC} + 2V_D$, the rectifier diodes are reverse biased and no power transfers to the load. The power transfer duration begins when v_{rect} reaches $V_{DC} + 2V_D$. v_{rect} is clamped by load and diode voltage $V_{DC} + 2V_D$. When v_{eq} drops below $V_{DC} + 2V_D$, the harvester current i_L freewheels through the rectifier diodes due to the existence of L_{eq} . v_{rect} is maintained at $V_{DC} + 2V_D$ until i_L reaches zero and the rectifier diodes are blocked again.

As shown in Fig. 3.7(b), before the rectifier input voltage v_{rect} reaches $V_{DC} + 2V_D$, the rectifier diodes are turned off and no power transfers to the load. The power transfer duration begins when v_{rect} reaches $V_{DC} + 2V_D$. v_{rect} is clamped by load and diode voltage $V_{DC} + 2V_D$. When v_{eq} drops below $V_{DC} + 2V_D$, the harvester current i_L freewheels through the rectifier diodes due to the existence of L_{eq} . v_{rect}

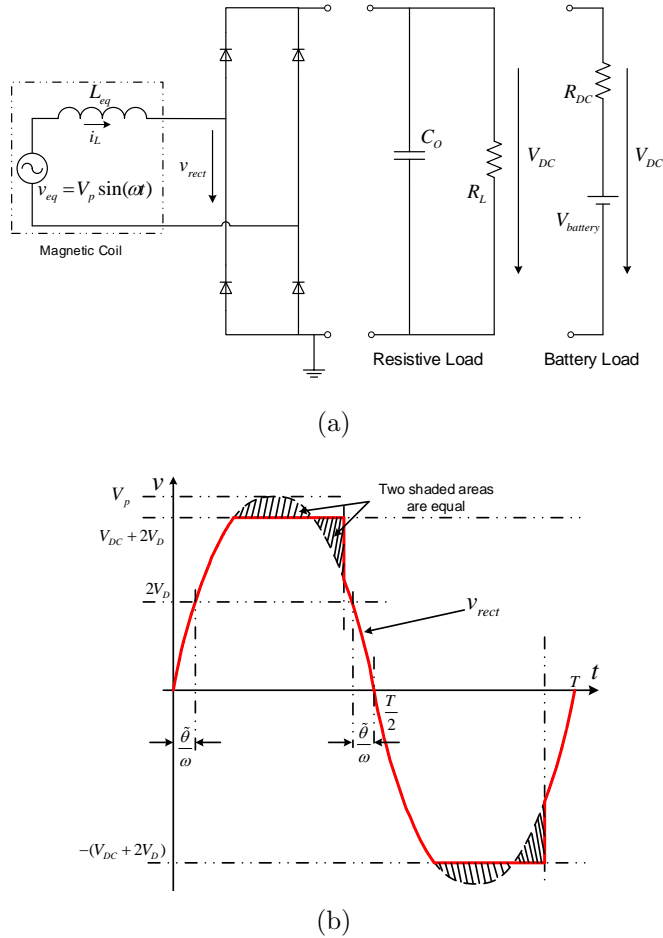


FIGURE 3.7: Conventional rectifier: shaded areas are the power conduction period.

is maintained at $V_{DC}+2V_D$ until i_L reaches zero and the rectifier diodes are blocked again.

When the resistive load is added, the output voltage V_{DC} can be determined by looking at the Fourier series

$$v_{DC_r}(t) = V_{DC0} + \sum_{n=1}^{\infty} V_{DCn} \cos(n\omega t + \Phi_n) \quad (3.3)$$

Suppose the harvester voltage is $v_{eq} = V_p \sin \omega t$. The DC component of the output voltage for the conventional rectifier is

$$\begin{aligned} V_{DC0_conv} &= \frac{1}{\pi} \int_{\tilde{\theta}}^{\pi - \tilde{\theta}} [V_p \sin(\omega t) - 2V_D] d(\omega t) \\ &= \frac{2}{\pi} [V_p \cos \tilde{\theta} - V_D (\pi - 2\tilde{\theta})] \end{aligned} \quad (3.4)$$

where $\tilde{\theta} = \arcsin(2V_D/V_p)$. Ignoring the harmonics in the output voltage, $V_{DC} \equiv V_{DC_conv}$ follows

$$V_{DC_conv} \leq \frac{2}{\pi} [V_p \cos \theta_1 - V_D (\pi - 2\theta_1)] \quad (3.5)$$

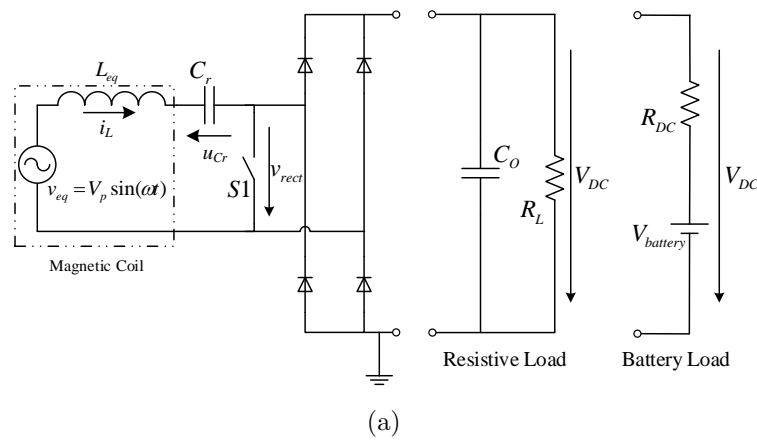
The value of the output voltage V_{DC_conv} varies with load resistance R_L . The peak harvester output voltage is typically several volts (some are even below 1V). Because the diode losses dominate in (3.5), even when V_{DC} reaches its maximum value, it can hardly satisfy the power requirement for most applications.

When the load changes to battery, V_{DC} can be seen as $V_{battery}$ due to the limited output power of the harvester (R_{DC} is small). Power transfer from the harvester to the load begins at $v_{eq} = V_{DC} + 2V_D$. Therefore, it is possible that the harvester peak output voltage V_p is lower or only little higher than the threshold voltage $V_{DC} + 2V_D$. The power transfer duration is limited to the shaded areas in Fig. 3.7(b) and the net energy extracted from the harvester cannot be high. When $V_p \leq V_{DC} + 2V_D$, no power can be extracted from the harvester.

3.2.2.2 Type I Capacitive Rectifier

The proposed Type I capacitive rectifier involves adding a resonant capacitor C_r in series with the magnetic coil and a bi-directional switch $S1$ in parallel (Fig. 3.8(a)).

Using the resonance between harvester internal inductance and the outside resonant capacitor, a high voltage is added to v_{rect} to overcome the threshold voltage $V_{DC} + 2V_D$.



(a)

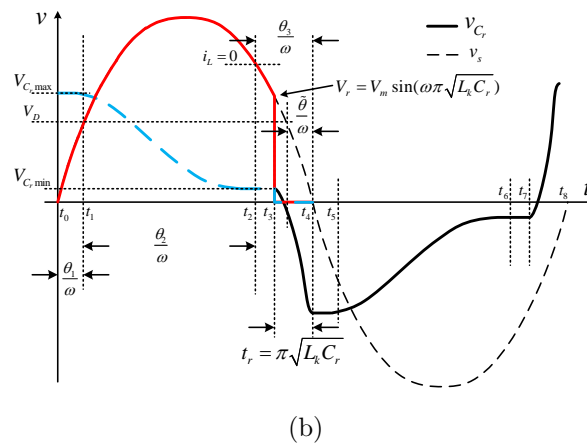


FIGURE 3.8: Resonant capacitive rectifier (Type I).

The switching timing diagram and principle of operation is shown in Fig. 3.8(b) and Fig. 3.9. Before t_0 , the resonant capacitor C_r is charged to its highest voltage

$V_{C_r\max}$ through bi-directional switch $S1$.

Mode I [t_0, t_1] [Fig. 3.9(a)]: The rectifier input voltage $v_{rect} = v_{eq} + V_{C_r\max}$ is lower than the threshold voltage $V_{DC} + 2V_D$. No power transfers from the harvester to the load.

Mode II [t_1, t_2] [Fig. 3.9(b)]: At t_1 , the rectifier input voltage v_{rect} reaches the threshold voltage $V_{DC} + 2V_D$ and the input current increases from 0. v_{rect} increases dramatically by adding the capacitor voltage $V_{C_r\max}$. The conduction period of the rectifier is thus extended. The capacitor voltage is discharged to $V_{C_r\min}$ and the two diodes in the positive direction turn off when i_L reaches zero at t_2 .

Mode III [t_2, t_3] [Fig. 3.9(c)]: The rectifier input voltage v_{rect} decreases with v_s and four diodes are blocked.

Mode IV [t_3, t_4] [Fig. 3.9(d)]: The bi-directional switch $S1$ turns on at t_3 , and the harvester leakage inductance L_k starts to resonate with outside capacitor C_r . The switching time period t_r is half the resonance period of C_r and L_k , as shown in (3.1).

Mode III and *Mode IV* are adjustable according to different applications. If the harvester output voltage is high, the power transfer duration is longer so that *Mode III* may disappear and *Mode IV* can be shortened. *Mode V* to *Mode VIII* are similar despite the fact that all the parameters are in the reverse direction.

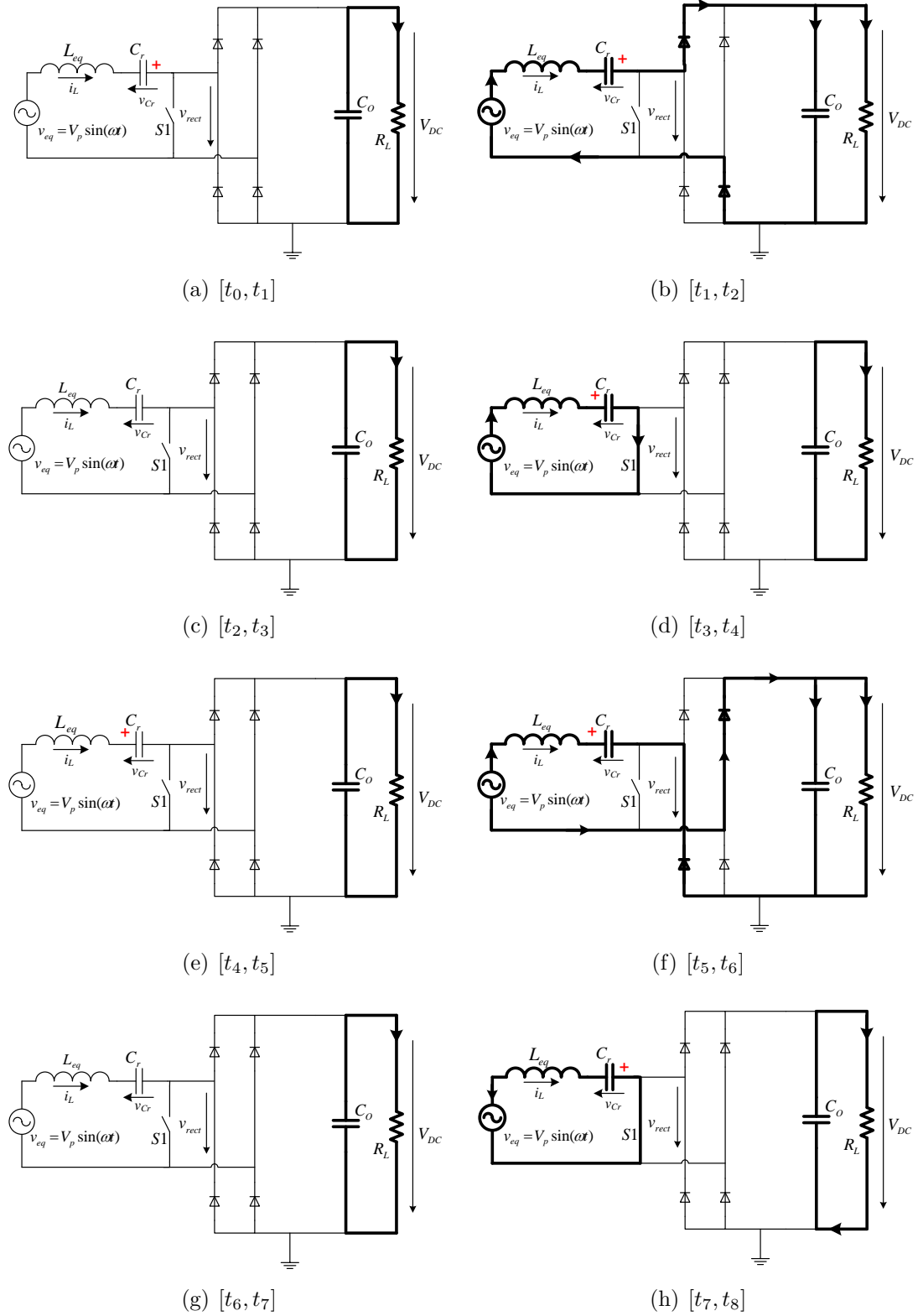


FIGURE 3.9: Principle of Operation (Type I converter).

When the resistive load is added, the output voltage V_{DC} can be derived from the Fourier series of the sum of the harvester output voltage v_{eq} and resonant capacitor voltage v_{Cr} (red and blue curve in Fig. 3.8(b)). In order to simplify the calculation, assume $V_{Cr,\min} = 0$ and v_{Cr} varies linearly. Since the harvester voltage v_{eq} is low, typically the harvester resonant voltage V_r in Fig. 3.8 is close to or lower than the diode forward voltage $2V_D$, so the DC component of the output voltage can be found similarly by integrating from θ_1 to $\tilde{\theta}$.

$$\begin{aligned} V_{DC0,I} &= \frac{1}{\pi} \int_{\theta_1}^{\pi - \tilde{\theta}} [V_p \sin(\omega t) - 2V_D] d(\omega t) + \frac{1}{\pi} \cdot (V_{Cr,\max} \theta_1 + \frac{1}{2} V_{Cr,\max} \theta_2) \\ &= \frac{1}{\pi} [V_p (\cos \tilde{\theta} + \cos \theta_1) - 2V_D (\pi - 2\tilde{\theta} - \theta_1)] + \frac{1}{2\pi} V_{Cr,\max} (2\theta_1 + \theta_2) \end{aligned} \quad (3.6)$$

The DC output voltage $V_{DC} \equiv V_{DC,I}$ follows

$$V_{DC0,I} < V_{DC,I} < V_{Cr,\max} + V_p - 2V_D \quad (3.7)$$

From (3.6), it can be seen that $V_{Cr,\max}$ is the key factor affecting output voltage V_{DC} , which can be found from the resonant period of leakage inductance L_{eq} and resonant capacitor C_r .

$$V_{Cr,\max} = V_p \cdot \frac{\sin(\omega\pi\sqrt{L_{eq}C_r})}{1 - \omega^2 L_{eq} C_r} \approx V_p \sin(\omega\pi\sqrt{L_{eq}C_r}) \quad (3.8)$$

Equation (3.8) indicates that for an existing harvester (V_p and L_{eq} are fixed, frequency is in a limited range), the resonant voltage $V_{Cr,\max}$ is decided by its resonant

capacitance. The maximum $V_{C_r\max}$ occurs at

$$C_r = \frac{\theta_3^2}{\pi^2 \omega^2 L_{eq}} \quad (3.9)$$

Substitute (3.9) into (3.8), the conduction period extends, compared to the conventional rectifier, by

$$t_{e\text{-max}} = \frac{1}{\omega} \tilde{\theta} - \frac{1}{\omega} \theta_{1\text{-min}} = \frac{1}{\omega} \arcsin\left(\frac{2V_D}{V_p}\right) \quad (3.10)$$

This extension of conduction time allows more energy from the harvester to be delivered to the load.

When the load changes to a battery, $V_{DC} = V_{battery}$. Suppose V_{C_r} in $[t_0, t_1]$ interval is linear

$$v_{rect} = V_{C_r\max} \left(\frac{\omega t - \theta_1 - \theta_2}{\theta_2} \right) + V_p \sin(\omega t) \quad (3.11)$$

where $\theta_1 < \omega t < \theta_1 + \theta_2$.

Compared to conventional rectifier, the proposed topology extends the conduction period by adding $V_{C_r\max} \left(\frac{\omega t - \theta_1 - \theta_2}{\theta_2} \cdot V_{C_r\max} \right)$. $V_{C_r\max}$ still follows equation (3.8), (3.9) and (3.10).

3.2.2.3 Type II Capacitive Rectifier

The proposed Type II capacitive rectifier involves adding a resonant capacitor C_r and a bi-directional switch $S1$ in parallel with the coil (Fig. 3.10(a)). Using the resonance between harvester internal inductance and the outside resonant capacitor, an extra inductor current is generated so that more energy can be transferred to the load.

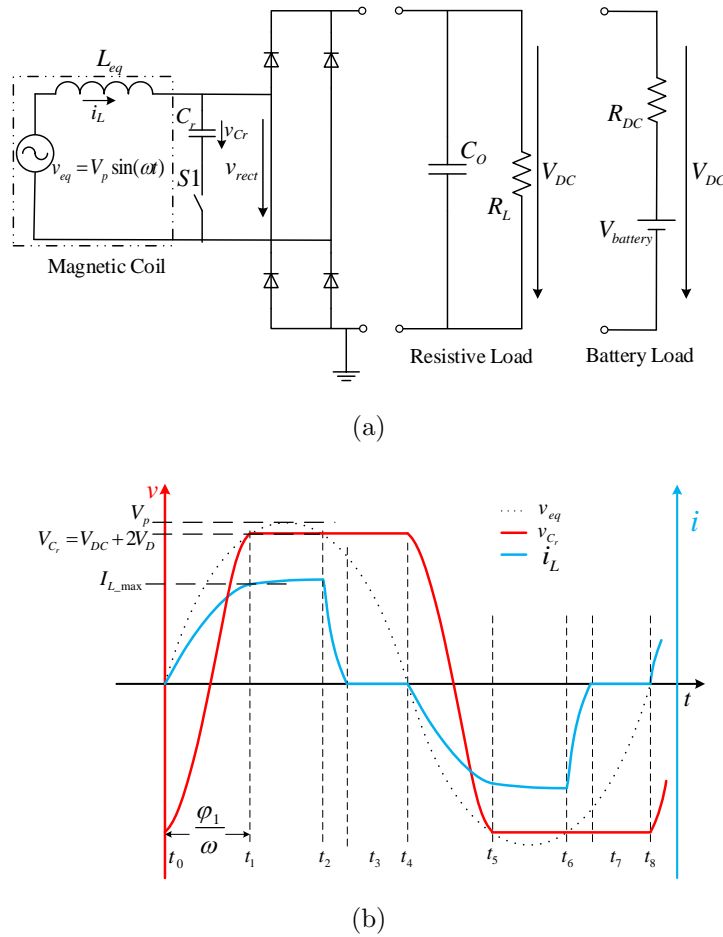


FIGURE 3.10: Resonant capacitive rectifier (Type II).

When the battery load is added, V_{DC} can be seen as $V_{battery}$ due to limited output power of the harvester (R_{DC} is small). As shown in Fig. 3.10(b), the bi-directional

switch $S1$ is triggered when the harvester voltage changes from negative to positive at t_0 . The input equivalent inductor resonates with the resonant capacitor and the input current i_L increases from zero. The switch $S1$ is tuned off when the input current i_L reaches its maximum value and capacitor voltage increases to $V_{battery} + 2V_D$ at $t_1 = \frac{\varphi_1}{\omega}$, where $\varphi_1 = \arcsin(\frac{V_{battery}+2V_D}{V_p})$. By adding the resonant current, input current i_L is thus increased.

During t_0 to t_1 , the harvester input equivalent inductor L_{eq} resonate with the parallel capacitor C_r . The input current increases from zero and the capacitor voltage is charged from negative to positive.

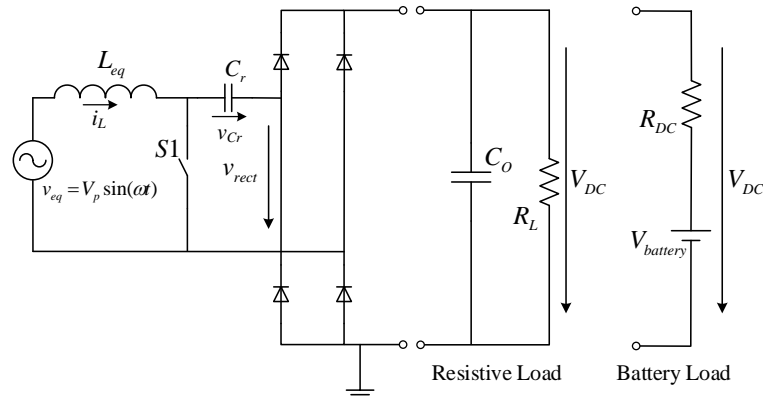
$$\begin{cases} i_L = V_{C_r} \sqrt{\frac{C_r}{L_{eq}}} \sin(\omega_0 t) + \frac{V_p \omega}{L_{eq}(\omega_0^2 - \omega^2)} (\cos(\omega_0 t) - \cos(\omega t)) \\ v_{C_r} = -V_{C_r} \cos(\omega_0 t) + \frac{V_p \omega}{1 - \omega_0^2 \omega^2} \left(\frac{1}{\omega} \sin(\omega_0 t) - \frac{1}{\omega_0} \sin(\omega t) \right) \end{cases} \quad (3.12)$$

where $\omega_0 = \sqrt{\frac{1}{L_{eq}C_r}}$. At t_1 , the input current i_L reaches its maximum value $I_{L\max} = i_L(t_1)$. The numerical solution of the resonant capacitor C_r can be found by $v_{C_r}(t_0) = -(V_{battery} + 2V_D)$ and $v_{C_r}(t_1) = V_{battery} + 2V_D$.

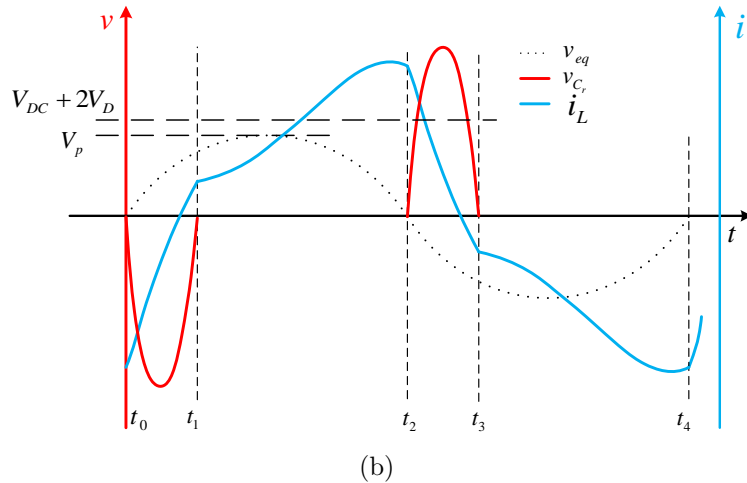
The unused energy in the conventional rectifier ($v_{rect} < V_{DC} + 2V_D$) is extracted with the resonance between equivalent inductance L_{eq} and external capacitor C_r . By adding $I_{L\max}$, more energy is transferred to the load.

3.2.2.4 Type III Capacitive Rectifier

The proposed Type III capacitive rectifier involves adding a bi-directional switch $S1$ in parallel with the coil and a resonant capacitor C_r in series with them (Fig. 3.11(a)).



(a)



(b)

FIGURE 3.11: Resonant capacitive rectifier (Type III).

At t_0 , the bi-directional switch $S1$ is turned off and the harvester inductance resonates with the outside capacitor. During t_0 and t_1 , the inductor current i_L starts to decrease and power transfers from harvester to the load. After half of

a resonant period, the voltage across resonant capacitor return to zero and the bi-directional switch is turned on at t_1 so that the inductor current can continue increase until the reversed half cycle begins at t_2 .

Unlike type I and type II rectifiers, the bi-directional switch is turn off during power transfer. With the resonant voltage across the capacitor, the voltage fed into the rectifier v_{rect} increases dramatically. The output power to the load is thus increased.

3.2.3 Experimental Result

In this section, the experiment results of Type I and Type II capacitive rectifier are presented. A comparison experiment is built with the same circuit parameters for the conventional rectifier without the proposed resonance. The magnetic harvester built into a roller skate has shown in Fig. 2.8 with parameters shown in TABLE 2.1. The open circuit voltage of proposed rotational harvester is shown in Fig. 3.12. The resonant capacitive rectifier is connected to either a 1.2V or a 2.4V NiMH battery as a load. The design parameters of the rectifier are shown in TABLE 3.2.

Since the battery load is connected, the comparison of output power becomes equivalent to compare the output current between the two topologies. The experimental results show both of the proposed circuits give higher output current compared to the conventional rectifier when the threshold voltage $V_{DC} + 2V_D$ is

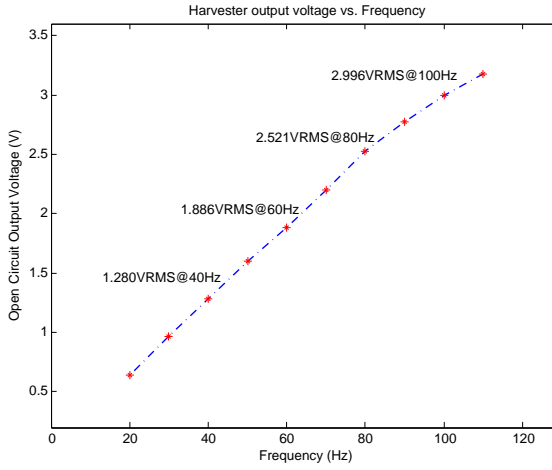


FIGURE 3.12: Open circuit voltage of proposed rotational inductive magnetic harvester.

TABLE 3.2: Circuit parameters of the rectifier

Parameters	Value	
Input inductance	L_{eq}	$\sim 2.98\text{mH}$
Parasitic resistance	R_w	9.4Ω
MOSFET	$R_{DS(on)}$	0.25Ω
Diode voltage drop	V_f	0.23V
Resonant capacitance (Type I)	$C_{r(I)}$	$268\mu\text{F}$
Resonant capacitance (Type II)	$C_{r(II)}$	$200\mu\text{F}$

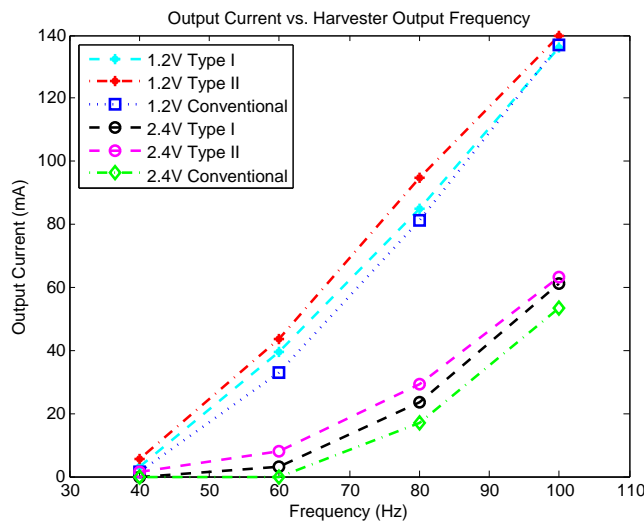


FIGURE 3.13: Output average current vs. Frequency.

relatively close to the maximum harvester output voltage V_p (Fig. 3.13). The Type II rectifier gives a little higher output current than the Type I rectifier at each frequency. Under the same output conditions, the proposed rectifier has a dominant advantage in lower frequency range. The Type I rectifier gives 23.5mA output and Type II rectifier gives 29.3mA at 80Hz with a 2.4V battery connected. Under the same condition, the conventional method only gives 16.9mA. As the frequency increases, the difference between the proposed approaches and the conventional approach gradually decreases. When the harvester frequency increases to 100Hz, the output currents for the two methods are almost the same under 1.2V battery due to the fact that the diode voltage is not the dominant power loss.

Fig. 3.14 shows the output current and voltage of the Type I capacitive rectifier under a 2.4V load and 80Hz harvester output. The output current suddenly drops to zero in the middle of each half period because the harvester cannot keep ideal uniform circular motion. When the coils pass the magnets, the strong magnetic force between them lower the rotation speed of the wheel. Therefore, the harvester output voltage and current of the harvester reduce each half period. Fig. 3.15 shows the input current and the gate signal. The proposed method provides more than 39% improvement in net energy out from the harvester compared to the conventional rectifier.

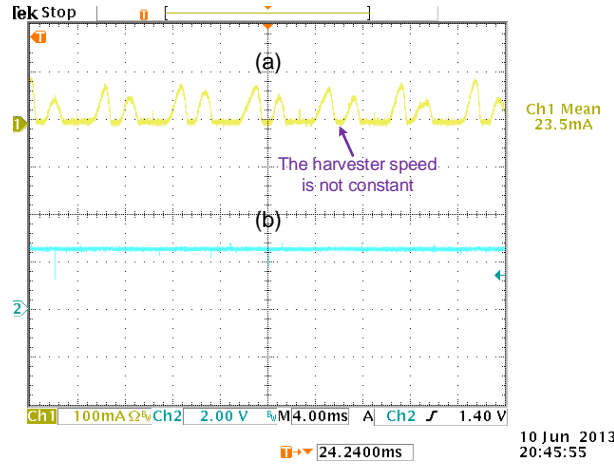


FIGURE 3.14: Capacitive rectifier: (a) Output current (100mA/div); (b) Output voltage (2V/div).

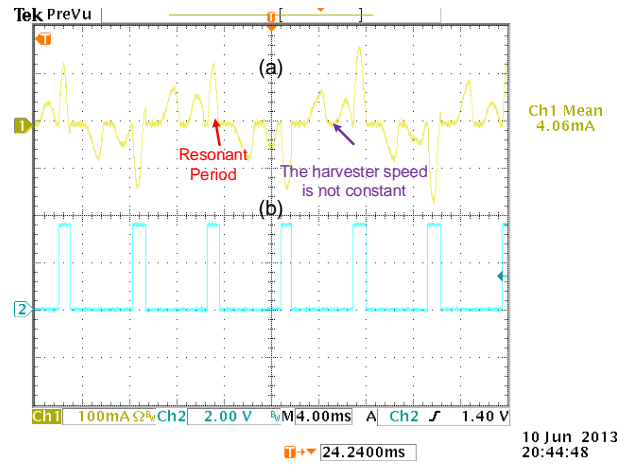


FIGURE 3.15: Capacitive rectifier: (a) Output current (100mA/div); (b) Output voltage (2V/div).

3.3 Dual Polarity Boost Converter

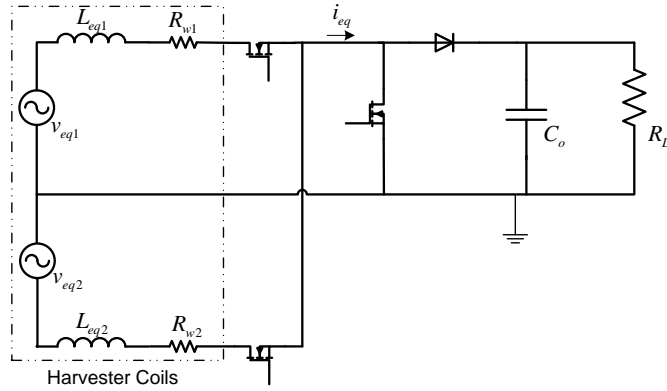
A new inductive magnetic energy harvesting system is introduced in this section. Using the electrical circuit model developed in Chapter 2, the influence of the harvester equivalent inductance on the converter output power is studied. Specifically, the main contributions are:

- Development of a new boost-derived high switching frequency AC-DC converter that utilizes the harvester internal equivalent inductance as the input boost inductance in order to reduce the size of the AC-DC converter.
- The relationship of air gap, harvester equivalent inductance and harvesting system output power is explained. Since the coil equivalent inductance is shared, it becomes a vital parameter affecting both harvester output power and converter power loss.

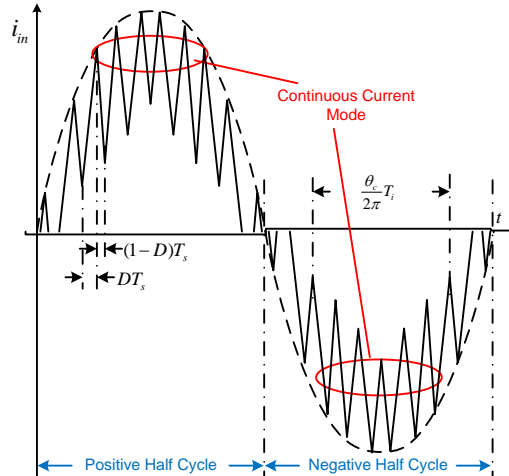
3.3.1 Principle of Operation

We propose to center tap the rotational magnetic harvester coil in Fig. 2.8. The bridgeless rectification is thus achieved by using one positive and one negative winding separately in the proposed dual polarity boost converter (Fig. 3.16). The boost derived topology is suitable for ultra-low voltage and low power application. According to the harvester equivalent model, the proposed circuit utilizes the leakage inductance of the center tapped coils as the two boost inductors. The EMF of the harvester will be considered as sinusoid in the following analysis in order to simplify the process.

The converter has four main operation modes as shown in Fig. 3.17. Each winding operates during a half cycle of the input AC voltage, with the control scheme of each half cycle is similar to a fixed duty ratio boost converter. Positive half cycle ($0 < t < \frac{T_i}{2}$, where T_i is the period of the harvester input voltage):



(a) Circuit diagram



(b) Input current

FIGURE 3.16: Proposed circuit and input current.

Mode I [Fig. 3.17(a)]: This mode begins when the rectification MOSFET M_1 and the main MOSFET M_3 are both turned on and the input current increases. In the negative winding, the rectification MOSFET M_2 is turned off and there is no current. This mode lasts for DT_s , where D is the duty ratio and T_s is switching period. Since the period of harvester input voltage $T_i \gg T_s$, considering the k^{th}

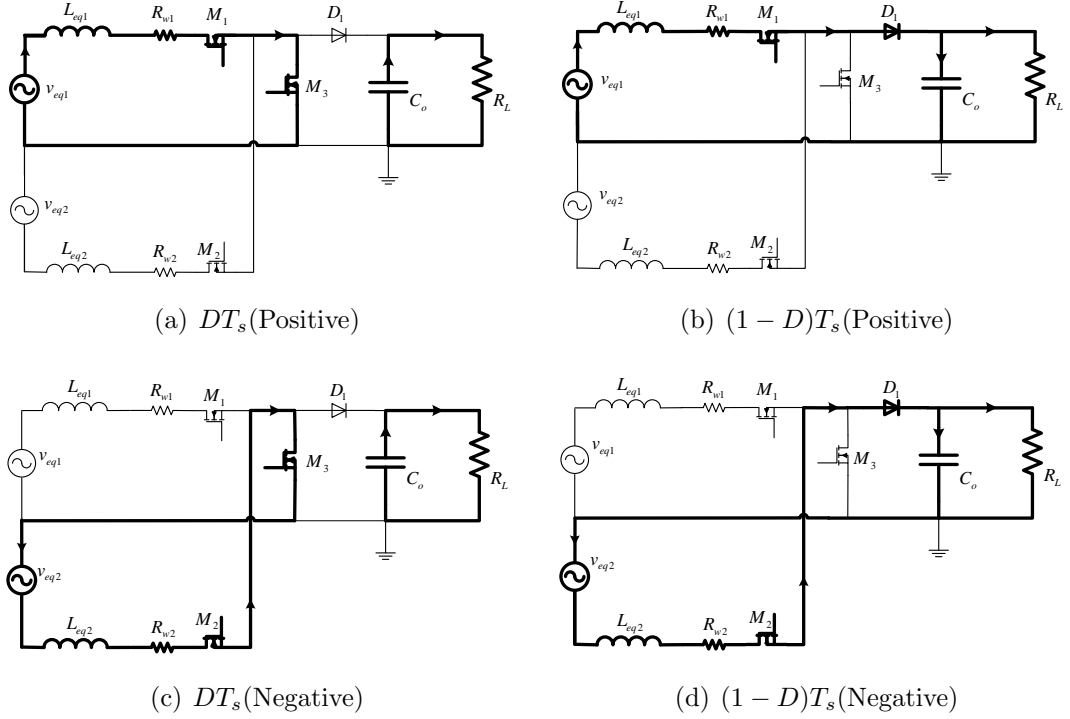


FIGURE 3.17: Principle of Operation:(a) (b) Positive half cycle of AC voltage.
(c) (d) Negative half cycle of AC voltage.

switching cycle of the converter, the input voltage can be seen as constant.

$$v_{eq1k} = v_{eq2k} = v_{eqk} = \frac{L_m}{L_k + L_m} V_p \sin (2\pi k \cdot \frac{T_s}{T_i}) \quad (T_s \ll T_i) \quad (3.13)$$

where V_p is the peak induced voltage of the harvester. Suppose all the switching devices are ideal, the second order equations for the inductors and capacitor during

Mode I are

$$\begin{cases} L_{eq} \frac{di_{eqk}}{dt} = v_{eqk} - R_w i_{eqk} \\ C_o \frac{dv_o}{dt} = -\frac{v_o}{R_L} \end{cases} \quad (3.14)$$

where i_{eqk} is the input current in the k_{th} switching cycle.

Mode II [Fig. 3.17(b)]: In this mode, the rectification MOSFET M_1 keeps on and

the main MOSFET M_3 turns off. The output diode D_1 is forward biased and the energy stored in the equivalent inductance L_{eq1} charges the load. The current is blocked in the negative winding as the same as in *Mode I*. This mode lasts for $(1 - D)T_s$.

In *Mode II*, the second order equation for the inductors and capacitor changes to

$$\begin{cases} L_{eq} \frac{di_{eqk}}{dt} = v_{eqk} - R_w i_{eqk} - v_o \\ C_o \frac{dv_o}{dt} = i_{eqk} - \frac{v_o}{R_L} \end{cases} \quad (3.15)$$

During the negative half cycle, the principle of operation is similar to positive half cycle, except for that the input voltage changes from positive to negative. Thus, the output voltage can be obtained by taking the average of (3.13)-(3.15) in the k^{th} switching cycle and then the solving for steady state values is

$$V_o = \frac{R_L(1 - D)}{R_w + R_L(1 - D)^2} \cdot \langle |v_{eqk}| \rangle = \frac{2}{\pi} \cdot \frac{L_m}{L_k + L_m} \cdot \frac{R_L(1 - D)}{R_w + R_L(1 - D)^2} V_p \quad (3.16)$$

where $\langle f(t) \rangle$ represents the average value of $f(t)$ and V_o is steady state value of output voltage v_o .

Besides these four conduction modes, the converter has discontinuous current mode (DCM) when the input voltage is low. In the DCM, the output diode current goes to zero when the main switch M_3 is off. The converter works in DCM and transfers to CCM after the input voltage builds up. In the proposed rotational magnetic harvester, the internal inductance L_{eq} is large, so the DCM duration is

much smaller compared to CCM duration and it is not considered in the voltage conversion ratio calculation.

3.3.2 Power Loss Analysis

The main losses in the proposed converter circuit results from the ON-state resistance of the MOSFETs, and the input and output diodes:

$$P_{loss} = 2 \cdot I_{eq(rms)}^2 \cdot R_{DS(on)1} + I_{SW(rms)}^2 \cdot R_{DS(on)3} + V_f \cdot I_{D(avg)} \quad (3.17)$$

where I_{eq} , I_{SW} and $I_{D(avg)}$ are RMS values of the input current (M_1 and M_2), main MOSFET (M_3) current and diode current (D_1), respectively. $R_{DS(on)1}$ and $R_{DS(on)3}$ are the turn on resistance of M_1 and M_3 , respectively. V_f is the forward voltage drop of the diode D_1 , which is assumed to be constant.

Considering the k^{th} switching cycle of the converter, the input current ripple is

$$\Delta i_{eqk} = \frac{v_{eqk}DT_s}{L_{eq}} \quad (3.18)$$

where Δi_{eqk} is the difference of the maximum and minimum value of i_{eqk} in k^{th} switching cycle and v_{eqk} is assumed to be constant during k^{th} switching cycle. The

RMS value of the source current over a switch cycle can be derived as

$$\left\{ \begin{array}{l} I_{eqk}^2 = \frac{1}{3} \Delta i_{eqk}^2 (D + D_f) = \frac{1}{3} \frac{v_{eqk}^2 D^3 T_s^2}{L_{eq}^2} \frac{1}{1 - v_{eqk}/V_o} \quad (\text{DCM}) \\ I_{eqk}^2 = I_{eqk(\text{avg})}^2 + \frac{v_{eqk}^2 D^3 T_s^2}{12 L_{eq}^2} \quad (\text{CCM}) \end{array} \right. \quad (3.19)$$

where $D_f = t_f/T_s$ and t_f is the time period that i_{eqk} drops from peak to zero in k^{th} switching cycle. Let $\theta = \omega t$, where $\omega = 2\pi/T_i$. Suppose $v_{eq} \ll V_o$, the RMS value of the input current can be calculated by taking the average of the half cycle integration:

$$I_{eq(rms)}^2 = \underbrace{\frac{1}{\pi} \left[\frac{V_p^2 D^3 T_s^3}{6 L_k^2} (\pi - \theta_c - \sin \theta_c) \right]}_{\text{DCM}} + \underbrace{\frac{V_o^2}{R_L^2 (1-D)^2} \theta_c + \frac{V_p^2 D^2 T_s^2}{24 L_k^2} (\theta_c - \sin \theta_c)}_{\text{CCM}} \quad (3.20)$$

where θ_c is the angular time when the converter works in CCM during half of the period of harvester input voltage T_i (Fig. 3.16(b)).

Similarly, the main MOSFET current (M_3) and diode current (D_1) are:

$$I_{SW(rms)}^2 = D I_{eq(rms)}^2 \quad (3.21)$$

$$I_{D(\text{avg})} = (1-D) I_{eq(\text{avg})} = \frac{1}{\pi} (1-D) \left[\frac{V_p D^2 T_s}{4 L_k} (\pi - \theta_c - \sin \theta_c) + \frac{V_o}{R_L (1-D)} \theta_c \right] \quad (3.22)$$

It can be seen from (3.20)-(3.22) that $I_{eq(rms)}$, $I_{SW(rms)}$ and $I_{D(\text{avg})}$ decrease when the leakage inductance L_k increases under the same load conditions. Therefore, by (3.17) this implies that the power loss on the rectification MOSFETs, main

MOSFET, and diode also decreases with higher L_k , as well as the air gap in the proposed harvesting system.

However, although the power loss of the converter decreases with the air gap, it is still not clear how the converter output power changes with the air gap. From the simulation result, $v_{eq} = \frac{L_m}{L_m + L_k} v_s$ drops severely due to L_m decreases and L_k increases as shown in Fig. 2.13(a) and Fig. 2.13(b) in Chapter 2. At the same time, shown in Fig. 2.11 in Chapter 2, L_{eq} is relatively stable from air gap 0.3mm to 3mm. So when the air gap increases, the output power of the converter decreases. In order to get more power from the harvester, the air gap should be maintained as small as possible.

3.3.3 Experimental Result

The inductive magnetic energy harvester (Fig. 2.8) and dual polarity boost converter, as described above, have been built for experiments. The design parameters of the converter are shown in TABLE 3.3. The converter is operated in open loop with a fixed duty ratio $D = 0.8$ at the switching frequency 20kHz and the frequency of the harvester output voltage is 110Hz. A nominal load of $R_L = 84.4\Omega$ is connected to the converter. The magnitude of the output voltage is around 3.3V (Fig. 3.18(a)), which means the output power is around 129mW. It can be seen in Fig. 3.18(b) that the input current is blocked by the rectification MOSFET during negative half cycle. The input current suddenly drops in the middle of each

TABLE 3.3: Circuit parameters and loss of the converter

Parameters		Value	Estimated Loss
Leakage inductance	L_{eq1}, L_{eq2}	$\sim 1.5\text{mH}$	
Winding resistance	R_w	4.7Ω	180mW
Rectification MOSFETs	$R_{DS(on)1}, R_{DS(on)2}$	0.075Ω	2.87mW
Main MOSFET	$R_{DS(on)3}$	0.002Ω	0.06mW
Output capacitor	C_o	$100\mu\text{F}$	
Output diode	V_f	0.23V	8.99mW
Controller and gate drive	LTC1541,LTC6702, LT1017		$\sim 0.46\text{mW}$
Output voltage	V_o	3.3V	

half period because when the coils pass the magnets, the strong magnetic force between them lower the rotation speed of the wheel.

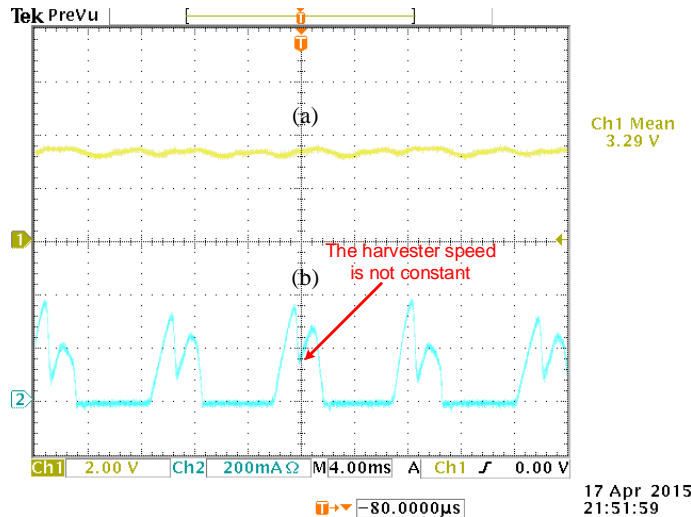


FIGURE 3.18: (a) Output voltage (2V/div); (b) Input current (200mA/div).

The power losses on switching devices are estimated according to (3.20)-(3.22). Due to the large value of input inductance ($\sim 1.5\text{mH}$), there is hardly any current ripple. The harvester is, thus, considered to work under CCM to simplify the calculation. As predicted, the main power losses come from the rectification

MOSFETs and output diode. The converter efficiency is estimated to be around 91%, which is higher than the state of the art converters designed for magnetic energy harvesting applications (50% in [11]).

The harvester has a maximum output power of 162.7mW at 110Hz under optimal resistance 4.7Ω . In this experiment we do not attempt to matching the input impedance to this value, but instead select duty ratio D to make $V_o = 3.3V$. Still, this system is able to extract 79% of the theoretical optimal value of 162.7mW. In order to regulate $V_o = 3.3V$ while at the same time perform maximum power point tracking, a front stage DC-DC might be added.

3.4 Conclusion

In this chapter, two types of AC-DC converter designed for magnetic energy harvester is proposed. The proposed resonant capacitive rectifier and the boost derived high frequency AC-DC converter can both increase the net energy extracted from the harvester. The leakage inductance of coils is utilized to form the input inductance to reduce the converter size. Experimental results are also provided to validate the theory. The results represent a new approach to designing power electronics for magnetic energy harvesters. Using the newly derived and more accurate models, better utilization of the leakage inductance is obtained. There is a design tradeoff between the leakage inductance, current ripple, gap size and

other parameters. For each AC/DC converter, there is an optimal power efficient leakage inductance for the system.

Chapter 4

Maximum Power Point Tracking Control

This chapter presents two maximum power point tracking algorithms designed for AC-DC power converter of magnetic energy harvesters. Due to the low power and intermittent nature of the ambient kinetic energy source, the key factor to design a power conversion algorithm for the magnetic harvester is to extract as much energy as possible from the harvester. A series of control algorithms which track the maximum point point for low power energy harvesting applications are reviewed, including magnetic harvester [18, 36, 37, 40], piezoelectric harvester [1, 2, 23, 28–30, 38, 41, 42], micro-scale PV module [43, 44] and thermoelectric harvester [41, 45]. Based on the summary of previous works, two new

impedance matching control algorithms designed for bridgeless AC-DC power conversion of magnetic energy harvester are introduced to achieve maximum power point tracking (MPPT): *a Phase/RMS MPPT* and *a Quasi MPPT* simplified from Phase/RMS MPPT method. Specifically, the research contributions of this section includes:

- *New maximum power point trackers for inductive energy harvesters:* A methodology to match or approach the input impedance of a bridgeless AC-DC converter to the complex conjugate of the inductive energy harvester is presented by using special designed maximum power point trackers. Specifically, the Phase/RMS MPPT tunes the phase and the RMS value of the input current alternatively in real time through a perturb and observe method to achieve maximum power. A double loop controller is proposed for this implementation. A quasi-MPPT method simplifies the double loop control by tuning the duty ratio directly to approach the maximum power.
- *Experimental verification on a rotational energy harvester:* A boost derived AC-DC converter is built and connected to a rotational magnetic harvester on a roller skate designed to charge a battery. Although a fair comparison to existing harvester MPPT methods in the literature [37] is difficult to discuss due to different experimental harvesters used, both of the proposed MPPT methods are demonstrated to extract higher energy and efficiency than the

latest reported typical MPPT approach designed for electromagnetic harvesters [37]. The experimental results confirm the theory and stability of the approach.

4.1 Literature Review

Due to the low power and intermittent nature of the ambient kinetic energy source, the key factor to design a power conversion circuit for the magnetic harvester is to extract as much energy as possible from harvester to the load and the energy storage element. Most of the previous works use the conventional bridge rectifier structure reviewed in 3.1.1 and the maximum power point tracking algorithm is applied as if the input is DC voltage [1, 2, 18, 23, 28, 29, 36–38]. In [28, 36], an approximate optimal DC voltage is maintained after rectification, which is directly proportional to the harvester open circuit voltage. This approach is simple to implement; however, maximum power point tracking cannot always be guaranteed and the energy transfer duration are suspended occasionally to measure the harvester open circuit voltage. Other approaches tend to use perturb and observe method to control the maximum power flow more precisely, which also employs the conventional bridge rectifier [1, 18, 23, 37]. One typical approach is reported in [37], it rectifies the harvester AC voltage with the bridge rectifier stage and then applies the conventional perturb and observe algorithm as if there is DC input. This approach replaces two lower diodes of the rectifier with two MOSFETs

to combine the rectification stage and voltage conversion stage so that the power loss is reduced. In this section, these typical approaches will be reviewed.

4.1.1 Approximate Optimal Reference Voltage

In [28, 36], an approximate optimal voltage is maintained at the converter input. Depending on the harvester technology, this voltage is either equal to the DC harvester output voltage (PV module and thermal electric harvester) or equal to the rectified AC output voltage (piezoelectric and electromagnetic harvesters). In both cases, the operating voltage is selected directly proportional to the open circuit voltage: the ratio of the voltage to its open circuit voltage is around 0.7 for the PV module and around 0.5 for the magnetic, piezoelectric and thermoelectric harvesters (Fig. 4.1). Theoretically, the harvester has maximum output power when the harvester output voltage is tuned to an optimal voltage. Another stage is needed to regulate the system output voltage if a resistive load is connected to the system.

The major benefit of this algorithm is that it is simple to implement and does not require much power on the control circuit. However, since the ratio of the optimal voltage to the harvester open circuit voltage is calculated approximately, it is not the actual maximum power point during operation. Furthermore, with this method, the energy transfer duration is suspended occasionally to measure the harvester open circuit voltage. The open circuit voltage can only be detected

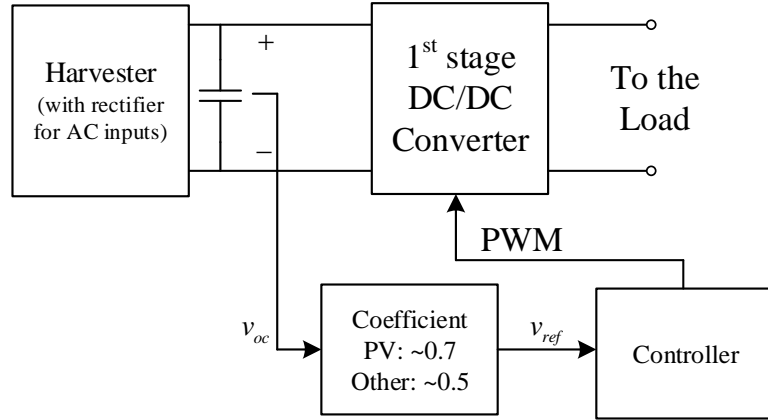


FIGURE 4.1: MPPT with optimal reference voltage.

infrequently in order to save energy. So it has slow response to the change of line and load conditions [28, 36]. At the same time, the energy source of the magnetic harvester is intermittent so that the line voltage and frequency may vary dramatically in a short time. With the fast changing line condition, the maximum power point tracking is not guaranteed. Other methods should be developed to control the maximum power flow more precisely for the magnetic harvester.

4.1.2 PWM Based Perturb and Observe Method

Perturb and observe methods are used to maintain accurate maximum power flow [1, 2, 23, 43, 44]. These approaches normally consist of two stages as shown in Section 3.1.1: a diode bridge rectifier for the first stage and a DC-DC converter for the second stage. The converter can be connected directly to a battery to avoid output voltage feedback control. A typical approach is shown in [1] (Fig. 4.2). Because the battery voltage can be seen as constant, the converter tracks the

power transfer by sensing the output current i_o . The increment of the duty cycle D of the DC-DC converter is determined by the slope of the output current curve $\partial I / \partial D$ [1], according to the formula

$$D_{i+1} = D_i + K \text{sgn}\left(\frac{\partial I}{\partial D}\right) \quad (4.1)$$

where D_{i+1} and D_i are the $(i+1)^{th}$ and i^{th} switching cycle, respectively. K is the

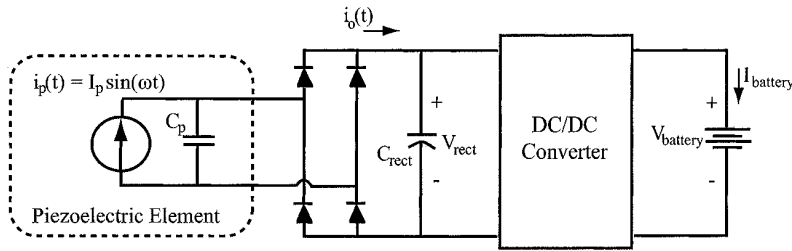


FIGURE 4.2: Conventional PWM based perturb and observe method.

assigned rate of change of the duty cycle and $\text{sgn}()$ is the signum function which returns the sign of the quotient $\partial I / \partial D$ [1]. According to (4.1), the controller adjusts the duty ratio by a small amount and senses the output current; if the output current increases, further adjustments in the same direction are continued each switching cycle until the output current no longer increases. This is called the perturb and observe and is the most popular technique to achieve MPPT. If a resistive load is connected, another DC-DC converter will be needed to regulate the output voltage to the load.

A major drawback of this approach is that it cannot achieve theoretical maximum power point since the MPPT algorithm is applied on the DC side as if the input

voltage is DC. Further, although the duty ratio can be updated every switching cycle, the controller cannot be designed to have fast response to the line voltage and frequency change due to the large input capacitor followed by the rectifier. However, due to the intermittent nature of the energy source, it is important for the magnetic harvester applications to respond fast to the frequency change. Furthermore, since the MPPT algorithm is applied on a DC/DC converter, rectification should be applied as the first stage before the DC/DC converter stage. As analyzed in Chapter 3, with this structure, the voltage drop on the rectifier diodes will severely lower the power conversion efficiency. In order to avoid such draw back, new studies tend to apply the control algorithm in the rectification stage with active bridge to reduce power loss [37].

4.1.3 Perturb and Observe Method with Active Bridge

One approach is reported in [37], the control algorithm is similar to the conventional perturb and observe method. It combines the diode bridge and the DC/DC converter by using two active diodes (MOSFETs) to avoid some power loss (Fig. 4.3). The output voltage is sensed and is assumed DC. As the same as the conventional perturb and observe method, the duty cycle is maintained constant for multiple magnetic harvester input voltage cycles and a slow perturb and observe algorithm is employed to tune the duty cycle.

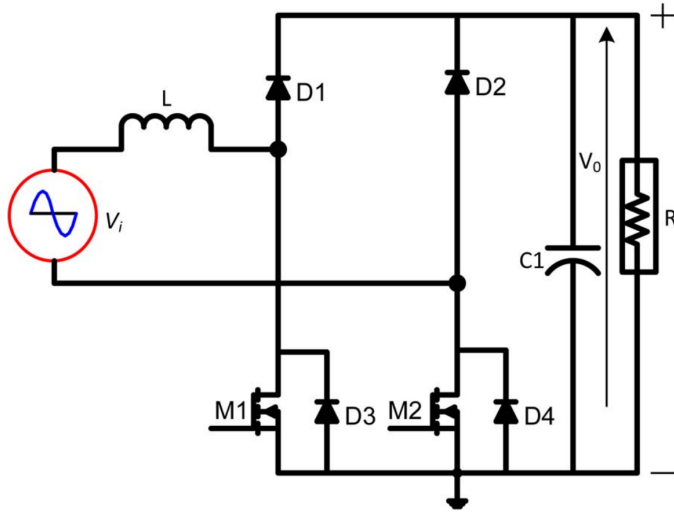


FIGURE 4.3: Perturb and observe method with active diode bridge.

Compared to the conventional PWM based perturb and observe method with diode bridge, this method avoids some power loss on the bridge diodes. However, this approach [37] also employs same control algorithm as the reviewed work shown in Section 4.1.2 so: 1) it cannot achieve the theoretical maximum power point since the duty ratio is fixed or change slowly in one harvester voltage line cycle; 2) the control speed can only be designed according to lowest harvester line cycle to keep duty ratio stable. It is difficult to operate under fast changing input frequency or voltage.

4.2 Proposed MPPT Control Algorithm

Two new approaches are now proposed for MPPT, which attempt to track the maximum power from the magnetic harvester. As derived in Chapter 2, the magnetic harvester can be modeled as an AC voltage source v_{eq} in series with an

inductor L_{eq} and a resistor R_w [31, 32] (Fig. 4.4). In order to reach maximum power transfer, it is desirable to have an AC-DC converter that behaves like an adjustable impedance (z_{in}) that attempts to cancel the effect of the harvester internal inductance. It should also tune its input resistance to be, in Fig. 4.4, equal to the harvester coil resistance. That is, for an ideal sinusoidal $v_{eq} = \sqrt{2}V_{eq} \cos \omega_{in}t$ in Fig. 4.4 with angular frequency ω_{in} , it is desirable to tune the input impedance of the AC-DC converter to become:

$$z_{in} = -j\omega_{in}L_{eq} + R_w \quad (4.2)$$

Keeping z_{in} value in (4.2) requires to control the harvester current to be in phase

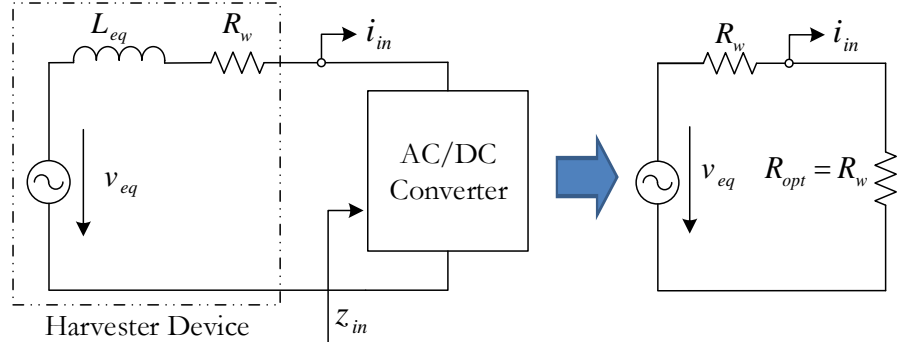


FIGURE 4.4: Match the impedance to get maximum power transfer.

with v_{eq} and to be with optimal RMS. The previous work [1, 2, 23, 37, 43, 44] tends to apply MPPT algorithm after rectifier with the method derived for DC-DC converters. In this case, the change of the duty ratio does not respond to the change in one cycle of the AC harvester line voltage (Fig. 4.5), so z_{in} cannot be tuned to its optimal value to achieve theoretical maximum power point. In this

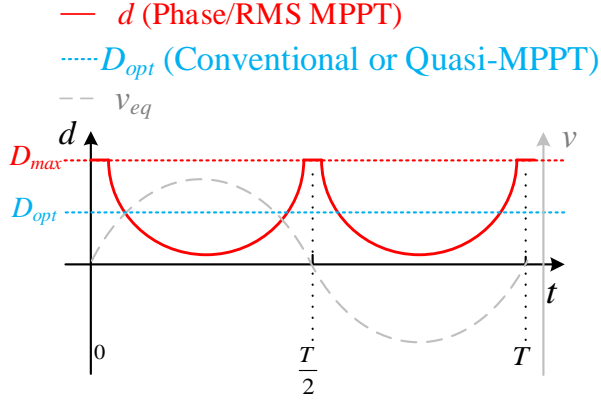


FIGURE 4.5: Duty ratio of conventional MPPT and two proposed MPPT methods.

thesis, the proposed algorithm will change the duty ratio during one line cycle to guarantee the optimal impedance condition is achieved as shown in Fig. 4.5. Further, since the MPPT algorithm is applied on the AC side, it has faster response time to the harvester line frequency and voltage change. This is particularly useful for the kinetic magnetic energy harvesters due to their intermittent and unstable energy sources. Specifically, the main contribution of the proposed Phase/RMS MPPT algorithm are:

- Tracking the theoretical maximum power point by changing the duty ratio to become time varying during one line voltage cycle to adjust the harvester input current i_{in} . Previous MPPT approach only slowly varied the duty ratio over multiple harvester line cycles [1, 2, 23, 37, 43, 44]. The perturbation period is normally 5 to 10 times as the lowest harvester line cycle.
- Applying the perturb and observe algorithm on the AC side so that any

bridgeless boost-derived converter topology can be used for the power conversion to enhance efficiency.

- Achieving faster response to the line voltage and frequency change by sensing the input current i_{in} on the AC side compared with the conventional MPPT methods designed for harvesting applications. Since only the duty ratio is detected, the previous MPPT approaches can only be designed to adjust to the change longer than the lowest harvester line cycle [1, 2, 23, 37, 43, 44]. Considering the intermittent nature of the harvester energy source, they may not be able to operate at the maximum power point due to the fast frequency change. Both of the proposed algorithms are able to track the change of every line cycle no matter how the frequency changes. It is more feasible to apply proposed algorithms to these applications with fast frequency change.

The proposed Phase/RMS method is simplified to a Quasi-MPPT method, which adjusts the duty ratio of the converter directly. The main advantage of the Quasi-MPPT method is:

- Compared to the conventional PWM based MPPT algorithm, the Quasi-MPPT method has faster response to the harvester line voltage and frequency change since the input current is monitored.
- Compared to the Phase/RMS MPPT algorithm, the Quasi-MPPT method simplifies the calculation and is more feasible for the applications with limited computational power.

4.2.1 Impedance Matching

In order to track the theoretical maximum power point, the harvester input current i_{in} needs to be under control. However, in (4.2), L_{eq} can only be roughly calculated by finite element analysis or estimated by measurement as shown in Chapter 2. It also has variation from harvesting device to harvesting device. Therefore, the accurate value of the optimal phase shift and amplitude/RMS of the input current is not available from analysis. In addition, the harvester equivalent voltage v_{eq} is in series with the inductive impedance in the harvester model (Fig. 4.4). The input current i_{in} may be out of phase with v_{eq} . That means the conventional phase modulation methods, such as in power factor correction applications [46–48], which normally generate phase reference of the input current directly from the AC voltage v_{eq} , are not directly applicable in the magnetic harvesting applications. However, this paper employs a new phase/RMS tracking perturb and observe controlling methodology, such that the impedance condition for z_{in} is achieved and maximum power extraction is obtained without measuring harvester equivalent voltage v_{eq} . The approach of the proposed controller has similar objectives of MPPT with impedance control for piezoelectric AC source in [29] by manually adjusting the transition instants of the full bridge converter, although the algorithms are unrelated. It also can be seen as an AC counterpart of DC photovoltaic resistive control that has been more widely applied [49, 50]. In the second approach, the phase/RMS method is simplified to a new quasi impedance matching method by fixing the duty ratio in one period of the input line current and tuning this

fixed duty ratio to approach the optimal output power. Since the line current is still sensed, the system response to the harvester frequency change is faster than the conventional PWM based MPPT algorithm [1, 2, 23, 37, 43, 44], which are designed for DC-DC converters.

A boost derived direct AC-DC converter is employed in this work for its benefits noted in Chapter 2: 1) The harvester internal impedance is used as input inductor to reduce the converter size; 2) The topology avoids diode bridge as the first stage, which is a main reason of the converter power loss; 3) Step-up conversion ratio; 4) The boost topology is feasible for input current control, which is equivalent to converter input impedance control. The schematic diagram of the proposed system is shown in Fig. 4.6. The input current is sensed by a small resistor and sent to a microcontroller after amplifying and filtering. The proposed control algorithm is performed in the microcontroller and then the corresponding PWM signal is generated. Since the low-side switches are used and this application is at low power level, the PWM signal from the microcontroller is directly fed into the MOSFETs, and no external drive circuit is needed. For simplicity of explanation, the voltage from the harvester device is considered as ideal sinusoid waveform in the analysis in this section. Discussion of higher harmonic effects is presented in later sections.

Due to the intermittent nature of lower power energy sources, a battery or a super capacitor is typically employed as energy buffer when the energy source is not

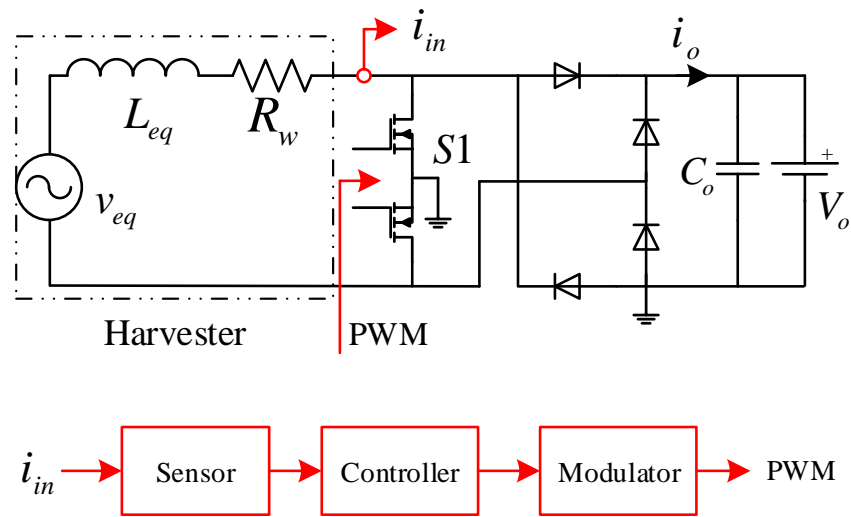


FIGURE 4.6: The schematic diagram of proposed method.

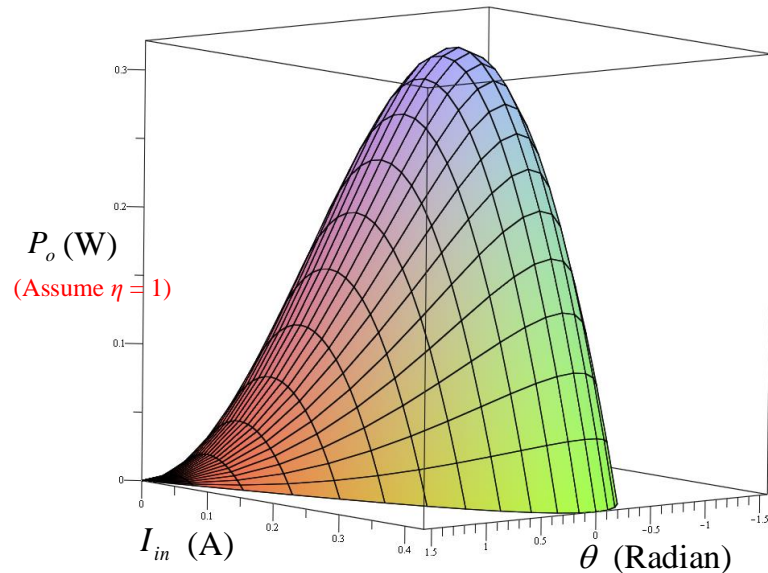


FIGURE 4.7: Tune the phase angle and RMS of input current to achieve MPPT.

achievable [1, 18, 29, 41]. Considering the popularity of DC bus in the low power energy harvesting applications, a battery load is used in the proposed approach.

4.2.2 Phase/RMS Control Algorithm

The proposed controller employs a double-loop system. The outer loop uses a specialized perturb and observe method to track the maximum power point and generate the input current reference i_{ref} . The phase angle θ and the RMS value of the input current I_{in} (upper case variable indicates RMS value) are controlled alternatively. The inner loop uses average current control to ensure that the input current i_{in} follows the reference current i_{ref} waveform. A PI controller is used as compensator in the inner loop. The unique outer loop is first discussed:

From the circuit theory, tuning the input impedance z_{in} of the converter to achieve the maximum power transfer is equivalent to tuning the input current i_{in} to satisfy (4.2). Suppose v_{eq} is sinusoidal with any angular frequency ω_{in} , and the RMS value of the input current is I_{in} and the angle of phase shift is θ , the system input power P_{in} is

$$P_{in} = (V_{eq}I_{in} \cos \theta - I_{in}^2 R_w) \quad \left(-\frac{\pi}{2} < \theta < \frac{\pi}{2}\right) \quad (4.3)$$

Then the output power P_o is

$$P_o = \eta P_{in} = \eta(V_{eq}I_{in} \cos \theta - I_{in}^2 R_w) \quad \left(-\frac{\pi}{2} < \theta < \frac{\pi}{2}\right) \quad (4.4)$$

where η is the efficiency of the energy harvesting system. According to (4.4), the converter input power as the function of I_{in} and θ is shown in Fig. 4.7 based on the parameters of the experimental “power amplifier” prototype which connects a 3.3mH inductor in series with a power amplifier to emulate the proposed rotational harvester (Fig. 2.1(b)). The maximum power occurs at

$$\begin{cases} \frac{\partial P_{in}}{\partial \theta} = V_{eq} I_{in} \sin \theta = 0 \\ \frac{\partial P_{in}}{\partial I_{in}} = V_{eq} \cos \theta - 2I_{in} R_w = 0 \end{cases} \Rightarrow \begin{cases} \theta = 0 \\ I_{in} = \frac{V_{eq}}{2R_w} \end{cases} \quad (4.5)$$

and the maximum converter input power is

$$P_{o(\max)} = \eta P_{in(\max)} = \eta \frac{V_{eq}^2}{4R_w} \quad (4.6)$$

The aim is to tune I_{in} and θ as (4.5) to maximize P_{in} or P_o assuming η is constant within the harvesting system operating range. However, the voltage source v_{eq} has inductive component within its harvester model (Fig. 4.6) and can only be measured under open circuit condition: it cannot directly be instantaneously measured when a real converter is attached to the harvester device. Further, the value of the internal inductance L_{eq} might be calculated off-line by the finite element analysis of the magnetic field or even estimated by measurement in non-operating conditions. However, neither is accurate enough for an MPPT algorithm as shown in Chapter 2. Therefore, the optimal phase shift and amplitude/RMS of input current reference can only be estimated beforehand in a rough range.

To avoid the need to directly estimate L_{eq} , the proposed Phase/RMS MPPT method generates the reference current i_{ref} from the output power P_o instead of harvester open circuit voltage v_{eq} . This is equivalent to maximizing the average output current \bar{I}_o , since the load is a battery and can be assumed as constant voltage [51]. The goal of the controller will be to simultaneously match the phase of θ , while at the same time match the resistive component of the input impedance of the AC-DC converter to R_w in Fig. 4.6.

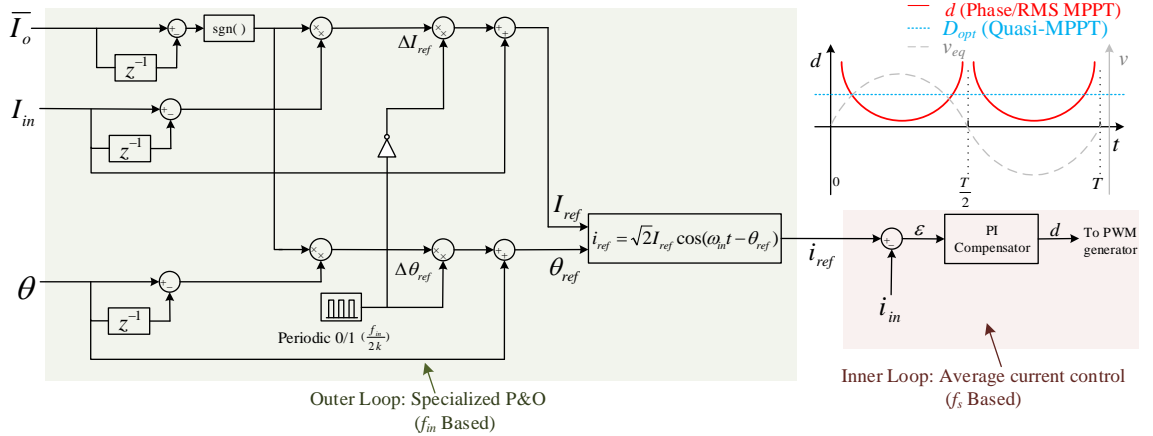
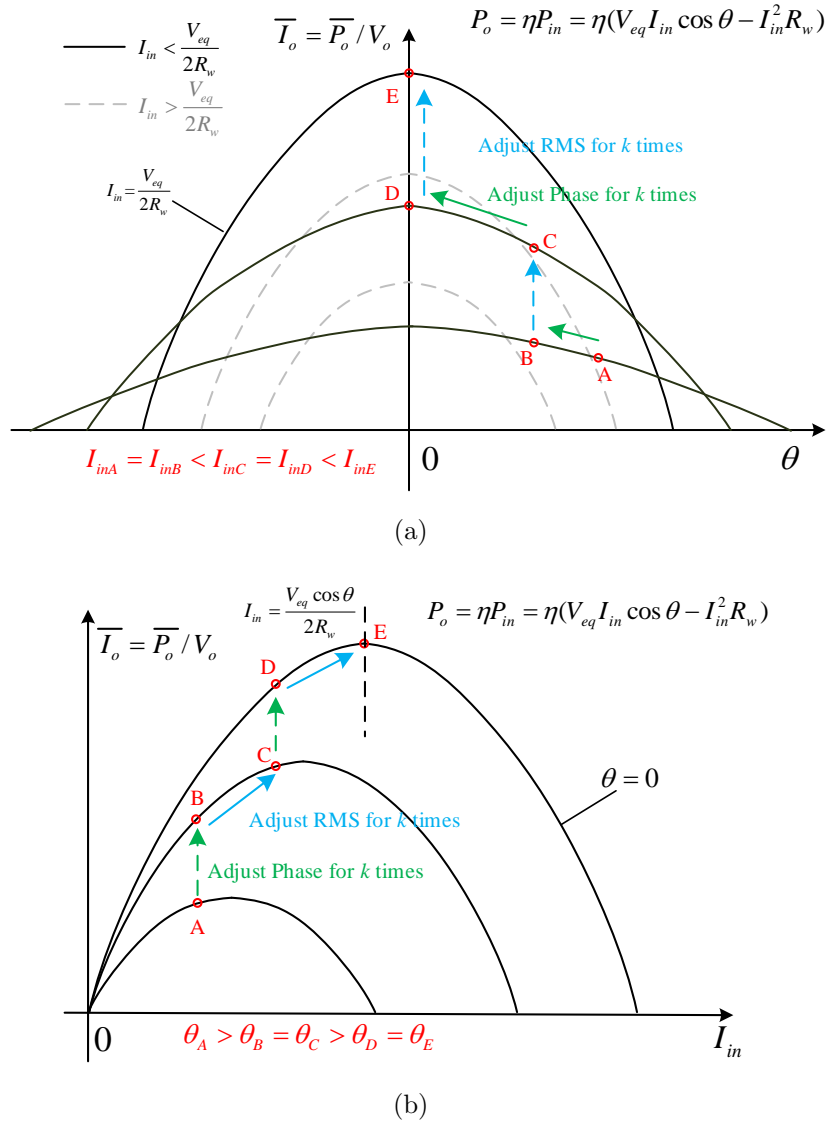


FIGURE 4.8: Control algorithm of the MPPT method.

Fig. 4.8 shows the control algorithm of the proposed approach. The phase angle θ and the RMS value I_{in} of the input current are adjusted alternatively with specialized perturb and observe method in the outer loop to generate reference current i_{ref} . It should be noted that the proposed method may not converge to the maximum power point as quick as some widely adopted optimization methods. Many two-dimensional MPPT approaches are not sensitive to power consumption [52–54]. So high level DSP or microprocessor, such as TMS320 series from

FIGURE 4.9: $I_{o(\text{avg})}$ vs. θ/I_{in} .

Texas Instruments, are normally employed. The MPPT algorithms can be designed to be more complicated to support the needs of these applications. In the proposed application, the available power is limited. In order to reduce energy consumption on the control circuit, a MSP430 series microprocessor is used in this research, which requires 1/10 of the power compared to TMS320 series and much lower computational power. The proposed two-dimensional algorithm is designed

to be simple to implement and easy to explain, even though $d(t)$ is time varying by adjusting phase angle and RMS value alternatively. For the low power energy harvesting applications, it is normal for two-dimensional MPPT algorithm to adjust the parameters alternatively [30, 42].

Often, a feedback controller of the converter would be designed to regulate the output voltage. But the proposed controller is operated to maximize the power flow into the battery, which is equivalent to maximizing the average current into the battery \bar{I}_o when assuming the battery voltage is nearly constant. Fig. 4.9 shows how the proposed control algorithm adjusts the phase angle and RMS value alternatively to achieve maximum average output current. According to (4.4), the output current follows the solid curve shown in 4.9(a) and 4.9(b) with phase angle θ and RMS I_{in} . The phase or RMS value of the input current is incrementally increased or decreased as determined by the slope of the average output current curve to achieve higher \bar{I}_o .

$$\begin{cases} \theta_{ref(i+1)} = \theta_{(i+1)} = \theta_{(i)} + \Delta\theta_{(i)} \cdot \text{sgn}(\Delta\bar{I}_{o(i)}) \\ I_{ref(i+1)} = I_{in(i+1)} = I_{in(i)} + \Delta I_{in(i)} \cdot \text{sgn}(\Delta\bar{I}_{o(i)}) \end{cases} \quad (4.7)$$

$\text{sgn}()$ returns the sign of the change of the average output current. If the average output current \bar{I}_o increases, the Phase/RMS of input current changes further in the same direction with predefined step; otherwise, the Phase/RMS changes to the reverse direction. Since the RMS value and phase angle are tuned, the duty ratio is time varying in one line cycle.

For example, suppose a harvesting system begins at point A in Fig. 4.9(a). The phase angle is adjusted with proposed perturb and observe method from point A to B to get higher output current; similarly, the RMS value is next adjusted from point B to C to get higher output current as shown in Fig. 4.9(b). RMS value and phase angle are adjusted alternatively and each parameter is adjusted for k times. It can be seen from Fig. 4.9(a), with different RMS value, the local maximum average output current jumps to a different curve for point C. Then the phase is adjusted again to move to point D. The process continues until the absolute maximum power point E is approached ($\theta = 0$ & $I_{in} = V_{eq}/2R_w$). Also, the local maximum output current with RMS is at $I_{in} = \frac{V_{eq}\cos\theta}{2R_w}$, which is related to phase angle θ . So the system is more likely to achieve zero phase shift first, then tuned to the absolute maximum average output current. When the output current is tuned to the stable state, there will be small fluctuation around the maximum value because the controller is always “trying” to find a better operation point.

As shown in Fig. 4.8, the inner loop adjusts the duty ratio in every switching period to track the change of the reference current i_{ref} . The sensed input current is processed by an amplifier and a filter. The input voltage i_{in} is compared with the reference current i_{ref} generated from the outer loop. The error signal is used by the PI controller to estimate the control current and then fed into the PWM generator. The PWM signal from the microcontroller goes directly to the gate of the two MOSFETs. The inner loop has much higher bandwidth than the outer loop, normally at least 5-10 times faster. In order to track the reference current

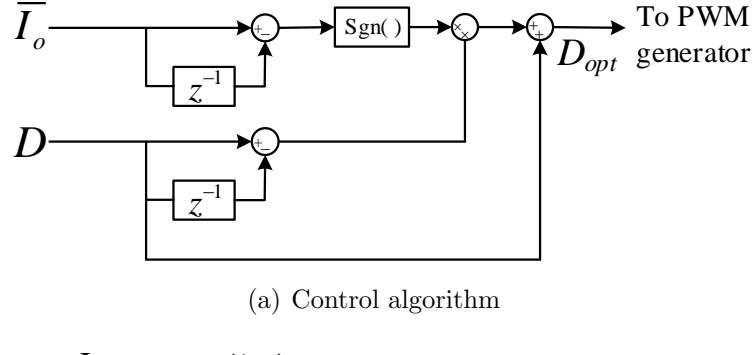
i_{ref} , the duty ratio of the proposed converter is updated every switching period as shown the red solid curve in Fig. 4.5. After a stable maximum power point is found, given $v_{eq} = \sqrt{2}V_{eq} \cos \omega_{int} t$, V_o and $i_{in} = \frac{v_{eq}}{2R_w}$, the duty ratio is

$$d(t) = 1 - \frac{\sqrt{2}V_{eq}}{2V_o} \frac{\sqrt{R_w^2 + \omega_{in}^2 L_{eq}^2}}{R_w} |\cos(\omega_{in}t - \theta)| \quad (4.8)$$

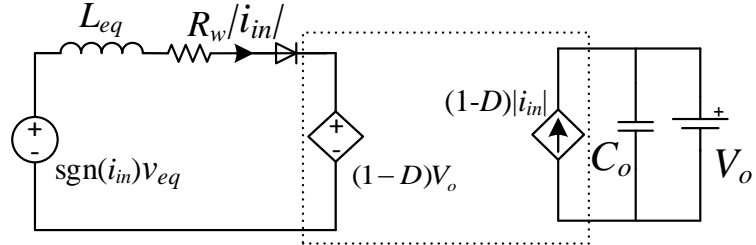
where $\theta = \arctan(\frac{\omega_{in}L_{eq}}{R_w})$. The proposed phase/RMS MPPT algorithm tracks the theoretical maximum power point ($P_o = \frac{V_{eq}^2}{4R_w}$) by tuning the input current i_{in} to the optimal phase and RMS value. Since the MPPT algorithm is applied on the AC side, the harvester line voltage and frequency change is detectable. The proposed method has faster response to the changing line condition compared to the conventional MPPT PWM based algorithm [1, 2, 23, 37, 43, 44] designed for energy harvesting applications.

4.2.3 Simplified Quasi-MPPT Method

In the Phase/RMS MPPT control method, the duty ratio $d(t)$ of the converter is time varying and is adjusting within each harvester line cycle to maintain MPP. This subsection presents a fixed duty ratio quasi-MPPT method (Fig. 4.10) that is simplified from the Phase/RMS MPPT. During each line cycle, a constant fixed duty ratio is maintained (Fig. 4.8). The dynamic response of the Quasi-MPPT algorithm is faster than the conventional PWM based MPPT method since the duty ratio is changed cycle by cycle. Then the best fixed duty ratio for each



(a) Control algorithm



(b) Average model of Quasi-MPPT method.

FIGURE 4.10: Fixed duty ratio Quasi-MPPT method.

line cycle is selected that produces maximum average output power during the line period. In this approach, the duty cycle is no longer adjusted each switching period, but only each line cycle. Since the harvester equivalent voltage is an AC voltage, to model the boost stage, we should assume that:

- The boost inductor operates in the continuous conduction mode;
- The output voltage V_o is constant during one harvester line period (V_o changes slow compared to the change of v_{eq} in one line cycle) [55].

Since the duty ratio D is fixed and V_o changes slower compared to the change of v_{eq} in one line cycle, D and V_o can be seen as constant. The proposed AC-DC converter in Fig. 4.6 is thus simplified as Fig. 4.10(b). Then the proposed AC-DC

converter (Fig. 4.6) can be averaged as shown in Fig. 4.10(b):

$$L_{eq} \frac{d|i_{in}|}{dt} = \text{sgn}(i_{in}) \cdot v_{eq} - |i_{in}|R_w - (1 - D)V_o \quad (4.9)$$

If the converter power loss is ignored, the instantaneous output power of converter is

$$P_o(t) = P_{in}(t) = |i_{in}|(1 - D)V_o \quad (4.10)$$

The maximum P_o over one line period need to be obtained by taking the average of P_{in} over a line cycle and solve the optimal duty ratio by taking derivative of D .

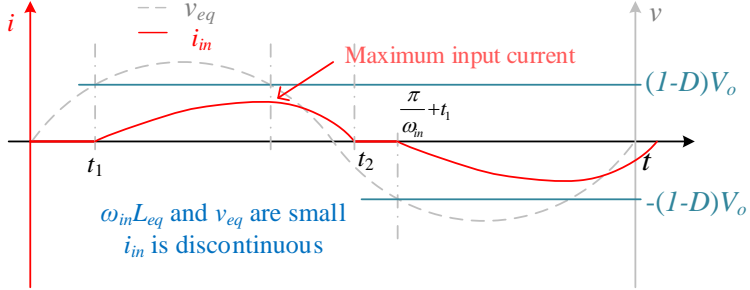
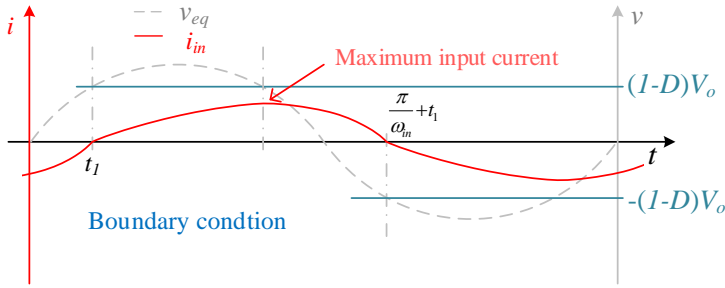
$$\frac{\partial(\frac{1}{T_{in}} \int_0^{T_{in}} P_o(t) dt)}{\partial D} = \frac{\partial(\frac{(1 - D)V_o}{T_{in}} \int_0^{T_{in}} |i_{in}| dt)}{\partial D} = 0 \quad (4.11)$$

It can be seen from (4.11), $i_{in}(t)$ needs to be solved in order to calculate optimal duty ratio D_{opt} . However, since the rectifier is connected to the harvester, the input current changes with circuit parameters as shown in Fig. 4.11.

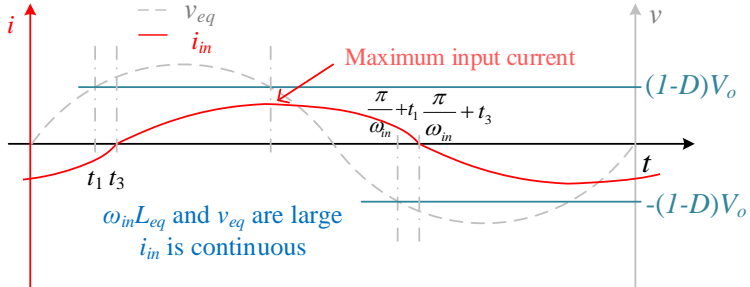
1. Discontinuous i_{in} ($i_{in}(t_1) = 0$, $i_{in}(t_2) < 0$, $t_2 < \frac{\pi}{\omega_{in}} + t_1$)

As shown in Fig. 4.11(a), since there is a rectifier connected with the harvester, if the input current drops to 0 before v_{eq} reaches $(1 - D)V_o$, the input current stays 0 until v_{eq} increases to $(1 - D)V_o$. Suppose the harvester voltage $v_{eq} = \sqrt{2}V_{eq} \sin(\omega_{int}t) = V_p \sin(\omega_{int}t)$, the initial condition for (4.9) is

$$i_{in}(t_1) = 0 \quad (4.12)$$

(a) Discontinuous i_{in} 

(b) Boundary

(c) Continuous i_{in} FIGURE 4.11: Input current changes with L_{eq} , V_{eq} , V_o and ω_{in} .

where $\sin(\omega_{in}t_1) = \frac{(1-D)V_o}{V_p}$. With given initial condition, (4.9) can be solved

$$\begin{aligned}
 i_{in}(t) = & \frac{V_p}{R_w^2 + \omega_{in}^2 L_{eq}^2} (R_w \sin \omega_{in} t - \omega_{in} L_{eq} \cos \omega_{in} t) - \frac{(1-D)V_o}{R_w} \\
 & - \frac{V_p}{R_w^2 + \omega_{in}^2 L_{eq}^2} (R_w \sin \omega_{in} t_1 - \omega_{in} L_{eq} \cos \omega_{in} t_1) e^{-\frac{R_w}{L_{eq}}(t-t_1)} \\
 & + \frac{(1-D)V_o}{R_w} e^{-\frac{R_w}{L_{eq}}(t-t_1)} \quad (t_1 < t < t_2)
 \end{aligned} \tag{4.13}$$

The input current i_{in} drops to 0 again at t_2 . t_2 is given by solving

$$\begin{aligned} & \frac{V_p}{R_w^2 + \omega_{in}^2 L_{eq}^2} (R_w \sin \omega_{in} t_2 - \omega_{in} L_{eq} \cos \omega_{in} t_2) - \frac{(1-D)V_o}{R_w} \\ & - \frac{V_p}{R_w^2 + \omega_{in}^2 L_{eq}^2} (R_w \sin \omega_{in} t_1 - \omega_{in} L_{eq} \cos \omega_{in} t_1) e^{-\frac{R_w}{L_{eq}}(t_2-t_1)} \\ & + \frac{(1-D)V_o}{R_w} e^{-\frac{R_w}{L_{eq}}(t_2-t_1)} = 0 \end{aligned} \quad (4.14)$$

According to (4.11), the optimal duty ratio needs to be solved by set the partial derivative with respect to D of the average input power over a line cycle equal to zero.

$$\begin{aligned} & - \frac{V_p V_o}{\pi \sqrt{R_w^2 + \omega_{in}^2 L_{eq}^2}} [\sin(\omega_{in} t_2 + \phi) - \sin(\omega_{in} t_1 + \phi)] \\ & + (1-D) \frac{V_p V_o}{\pi \sqrt{R_w^2 + \omega_{in}^2 L_{eq}^2}} [\omega_{in}^2 \cos(\omega_{in} t_2 + \phi) \frac{\partial t_2}{\partial D} - \omega_{in}^2 \cos(\omega_{in} t_1 + \phi) \frac{\partial t_1}{\partial D}] \\ & + 2(1-D)(t_2 - t_1) \frac{\omega_{in} V_o^2}{\pi R_w} - \frac{\omega_{in} V_o^2 (1-D)^2}{\pi R_w} \frac{\partial(t_2 - t_1)}{\partial D} \\ & - \frac{V_p V_o}{\sqrt{R_w^2 + \omega_{in}^2 L_{eq}^2}} \frac{\omega_{in} L_{eq}}{\pi R_w} \cos(\omega_{in} t_1 - \phi) (e^{-\frac{R_w}{L_{eq}}(t_2-t_1)} - 1) \\ & + (1-D) \frac{V_p V_o}{\pi \sqrt{R_w^2 + \omega_{in}^2 L_{eq}^2}} \frac{\omega_{in}}{\pi} \cos(\omega_{in} t_1 - \phi) e^{-\frac{R_w}{L_{eq}}(t_2-t_1)} \frac{\partial(t_2 - t_1)}{\partial D} \\ & + (1-D) \frac{V_p V_o}{\pi \sqrt{R_w^2 + \omega_{in}^2 L_{eq}^2}} \frac{\omega_{in}^2 L_{eq}}{\pi R_w} \sin(\omega_{in} t_1 - \phi) \frac{\partial t_1}{\partial D} e^{-\frac{R_w}{L_{eq}}(t_2-t_1)} \\ & + 2(1-D) \frac{\omega_{in} V_o^2 L_{eq}}{\pi R_w^2} (e^{-\frac{R_w}{L_{eq}}(t_2-t_1)} - 1) + \frac{\omega_{in} V_o^2 L_{eq} (1-D)^2}{\pi R_w^2} e^{-\frac{R_w}{L_{eq}}(t_2-t_1)} \frac{\partial(t_2 - t_1)}{\partial D} \\ & = 0 \end{aligned} \quad (4.15)$$

As shown in (4.15), t_1 and t_2 are the function of D , but there is no closed form solution for $\frac{\partial(t_2-t_1)}{\partial D}$. In this case, there is no closed form solution for optimal duty ratio.

2. Boundary condition ($i_{in}(t_1) = 0, i_{in}(\frac{\pi}{\omega_{in}} + t_1) = 0$)

The boundary situation occurs when the input current drops to 0 at $\frac{\pi}{\omega_{in}} + t_1$. At $\frac{\pi}{\omega_{in}} + t_1$, $V_p \sin \omega_{in} t = (1 - D)V_o$, the negative input current starts to increase. i_{in} becomes continuous. The initial condition is the same as discontinuous input current so that the equation for input current is the same as (4.13). Given (4.13), $i_{in}(\frac{\pi}{\omega_{in}} + t_1) = 0$ and $V_p \sin(\omega_{in} t_1) = (1 - D)V_o$, boundary condition equation is

$$\begin{aligned} & -\frac{V_p}{R_w^2 + \omega_{in}^2 L_{eq}^2} \left(R_w \frac{(1 - D)V_o}{V_p} - \omega_{in} L_{eq} \sqrt{1 - \frac{(1 - D)^2 V_o^2}{V_p^2}} \right) (1 + e^{-\frac{\pi R_w}{\omega_{in} L_{eq}}}) \\ & - \frac{(1 - D)V_o}{R_w} (1 - e^{-\frac{\pi R_w}{\omega_{in} L_{eq}}}) = 0 \end{aligned} \quad (4.16)$$

In the proposed application, the frequency is low and $e^{-\frac{\pi R_w}{\omega_{in} L_{eq}}} \ll 1$. The boundary equation can be simplified as

$$\frac{1}{R_w^2 + \omega_{in}^2 L_{eq}^2} (\omega_{in} L_{eq} \sqrt{V_p^2 - (1 - D)^2 V_o^2} - R_w (1 - D)V_o) - \frac{(1 - D)V_o}{R_w} = 0 \quad (4.17)$$

If (4.17) is less than 0, the input current is discontinuous and if (4.17) is larger than 0, the input current is continuous. From (4.17), if V_p, L_{eq}, D

are large and V_o, R_w are small, the input current is continuous. On the contrary, if V_p, L_{eq}, D are small and V_o, R_w are large, the input current is discontinuous.

3. Continuous i_{in} ($i_{in}(t_3) = 0, i_{in}(\frac{\pi}{\omega_{in}} + t_3) = 0, t_3 > t_1$)

The input current is continuous if the current drops to 0 after $\frac{\pi}{\omega_{in}} + t_1$. The initial condition for (4.9) is

$$i_{in}(t_3) = 0 \quad (t_3 > t_1) \quad (4.18)$$

The input current is

$$\begin{aligned} i_{in}(t) = & \frac{V_p}{R_w^2 + \omega_{in}^2 L_{eq}^2} (R_w \sin \omega_{in} t - \omega_{in} L_{eq} \cos \omega_{in} t) - \frac{(1-D)V_o}{R_w} \\ & - \frac{V_p}{R_w^2 + \omega_{in}^2 L_{eq}^2} (R_w \sin \omega_{in} t_3 - \omega_{in} L_{eq} \cos \omega_{in} t_3) e^{-\frac{R_w}{L_{eq}}(t-t_3)} \\ & + \frac{(1-D)V_o}{R_w} e^{-\frac{R_w}{L_{eq}}(t-t_3)} \end{aligned} \quad (4.19)$$

Given $i_{in}(\frac{\pi}{\omega_{in}} + t_3) = 0, t_3$ can be solved

$$\omega_{in} t_3 = \arcsin \left[\frac{(1-D)V_o}{V_p} \cdot \frac{e^{-\frac{\pi R_w}{\omega_{in} L_{eq}}} - 1}{e^{-\frac{\pi R_w}{\omega_{in} L_{eq}}} + 1} \sqrt{1 + \frac{\omega_{in}^2 L_{eq}^2}{R_w^2}} \right] - \phi \quad (4.20)$$

where $\phi = -\arctan \frac{\omega_{in} L_{eq}}{R_w}$. Similar to the discontinuous i_{in} situation, the optimal duty ratio needs to be calculated as the function of t_3 following (4.11).

$$\begin{aligned}
 & \frac{2V_o V_p}{\sqrt{R_w^2 + \omega_{in}^2 L_{eq}^2}} \sin(\omega_{in} t_3 + \phi) - \frac{2(1-D)V_o V_p}{\sqrt{R_w^2 + \omega_{in}^2 L_{eq}^2}} \cos(\omega_{in} t_3 + \phi) \frac{\partial t_3}{\partial D} \\
 & + \frac{2V_o^2(1-D)}{R_w} - \frac{V_p V_o}{\sqrt{R_w^2 + \omega_{in}^2 L_{eq}^2}} \frac{\omega_{in} L_{eq}}{\pi R_w} \cos(\omega_{in} t_3 + \phi) (e^{-\frac{\pi R_w}{\omega_{in} L_{eq}}} - 1) \\
 & - \frac{(1-D)V_p V_o}{\sqrt{R_w^2 + \omega_{in}^2 L_{eq}^2}} \frac{\omega_{in}^2 L_{eq}}{\pi R_w} \sin(\omega_{in} t_3 + \phi) \frac{\partial t_3}{\partial D} (e^{-\frac{\pi R_w}{\omega_{in} L_{eq}}} - 1) \\
 & + \frac{2V_o^2 \omega_{in} L_{eq}}{\pi R_w^2} (1-D) (e^{-\frac{\pi R_w}{\omega_{in} L_{eq}}} - 1) = 0
 \end{aligned} \tag{4.21}$$

As shown in (4.20), t_3 is the function of D .

$$\frac{\partial t_3}{\partial D} = - \frac{\frac{(1-D)V_o}{V_p} \cdot \frac{e^{-\frac{\pi R_w}{\omega_{in} L_{eq}}} - 1}{e^{-\frac{\pi R_w}{\omega_{in} L_{eq}}} + 1} \sqrt{1 + \frac{\omega_{in}^2 L_{eq}^2}{R_w^2}}}{\omega_{in} \sqrt{1 - [\frac{(1-D)V_o}{V_p} \cdot \frac{e^{-\frac{\pi R_w}{\omega_{in} L_{eq}}} - 1}{e^{-\frac{\pi R_w}{\omega_{in} L_{eq}}} + 1} \sqrt{1 + \frac{\omega_{in}^2 L_{eq}^2}{R_w^2}}]^2}} \tag{4.22}$$

Again, there is no closed form solution for optimal duty ratio that maximized output power for the continuous input current situation.

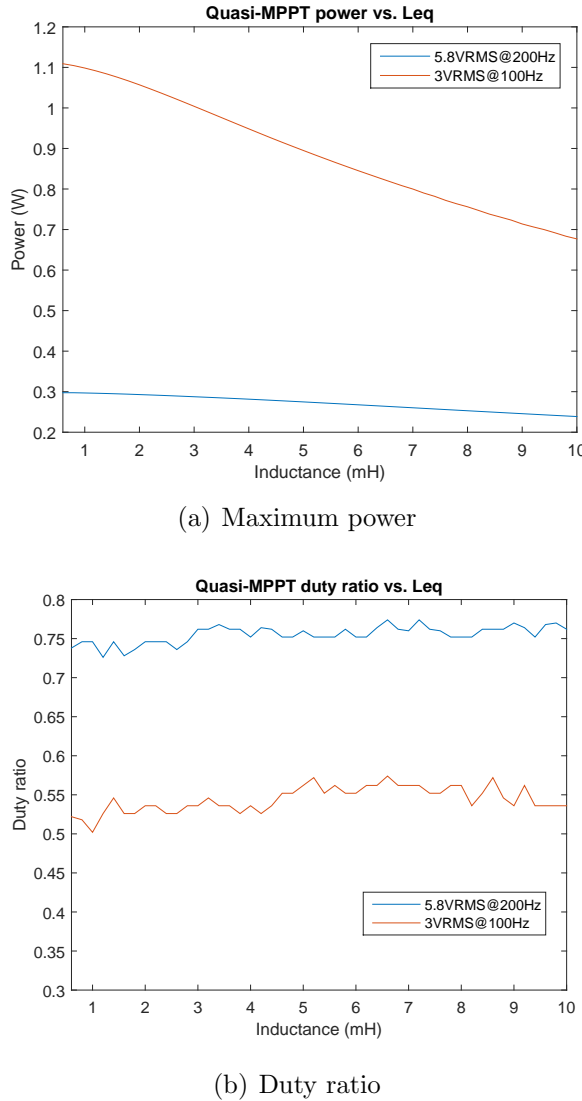
It can be seen from the above analysis, there is no closed form solution for optimal duty ratio. Simulation will be used to calculate maximum output power and optimal duty ratio for Quasi-MPPT method. A simulation model is built in MATLAB/Simulink with ideal circuit parameters. The circuit parameters are from the

proposed harvester: V_{eq} is 3VRMS@100Hz and 5.8VRMS@200Hz, R_w is 7Ω , V_o is 7V. With the given conditions, the converter works in discontinuous mode when L_{eq} is smaller than 0.6mH and the average model is not valid. In the simulation, L_{eq} changes from 0.6mH to 10mH. With given L_{eq} , duty ratio is swept from 0 to 1 to find the maximum output power point. It can be seen from Fig. 4.12 that the maximum input power drops with increasing inductance L_{eq} . According to (4.6), the output power of the Phase/RMS MPPT method does not change with L_{eq} . Phase/RMS method has more advantage over Quasi-MPPT method when L_{eq} increases. The input power reaches its maximum point when L_{eq} is 0.6mH, 1109mW at 200Hz and 297mW at 100Hz. Compared to the theoretical maximum power calculated from (4.3) for Phase/RMS, 1200mW at 200Hz and 321mW at 100Hz, both of them has 92% of the theoretical maximum power. The optimal duty ratio D_{opt} decreases with RMS value of input voltage V_{eq} .

Therefore, an MPPT can be designed to slowly track D_{opt} cycle by cycle to achieve high output power (Fig. 4.10(a)). The proposed Phase/RMS MPPT algorithm is thus simplified. The duty ratio of the converter is controlled by

$$D_{opt(i+1)} = D_{opt(i)} + \Delta D_{opt} \cdot \text{sgn}(\Delta \overline{I_{o(i)}}) \quad (4.23)$$

In order to match the harvester impedance, the duty ratio of the previously presented Phase/RMS MPPT method adjusts every switching period $T_s \ll T_{in}$ (Fig. 4.5). So it can track the theoretical maximum power of the harvester. The

FIGURE 4.12: Quasi-MPPT method: maximum power vs. L_{eq} .

quasi-MPPT control keeps the duty ratio fixed over one period and only updates it at the beginning of each input period. Although it may not track the theoretical instantaneous maximum power point, if it reaches stable state, it may be close to optimal. This method avoids to use the double loop system, which dramatically reduces the design complexity of the controller and makes it more feasible for the microprocessors with limited memory size. Compared to the conventional

PWM-based MPPT methods designed for DC-DC converters [1, 2, 23, 37, 43, 44], the proposed Quasi-MPPT method has faster response to the line voltage and frequency change of the harvester. Conventional PWM-based MPPT controller normally has fixed bandwidth no matter how the line frequency changes at AC side. The outer loop needs to be designed according to the lowest line frequency. With the proposed quasi-MPPT controller, the line frequency is tracked so that the dynamic response is faster at higher frequency.

4.3 Control Implementation

The proposed controller is implemented using MSP430F5172 microprocessor from Texas Instruments. Comparing to other popular controllers, such as TMS320 series from Texas Instruments, it offers ultra low power consumption and less cost, only about 1/10 of power consumption and 1/5 of the cost. However, at the same time, only limited peripherals and computational speed are provided. It includes analog-to-digital converter (ADC), pulse-width modulator (PWM) and hardware multiplier for controlling the converter. The proposed specialized perturb and observe algorithm is shown in Fig. 4.13. The phase and RMS value are selected alternatively, each for $2k$ line cycle periods ($k = 5$ in the experimental section), to generated reference input current in Phase/RMS MPPT control (Fig. 4.13(a)). If the output current increases, the phase angle or RMS value will be tuned to the same direction, and vice-a-versa. The step of phase angle and RMS value are

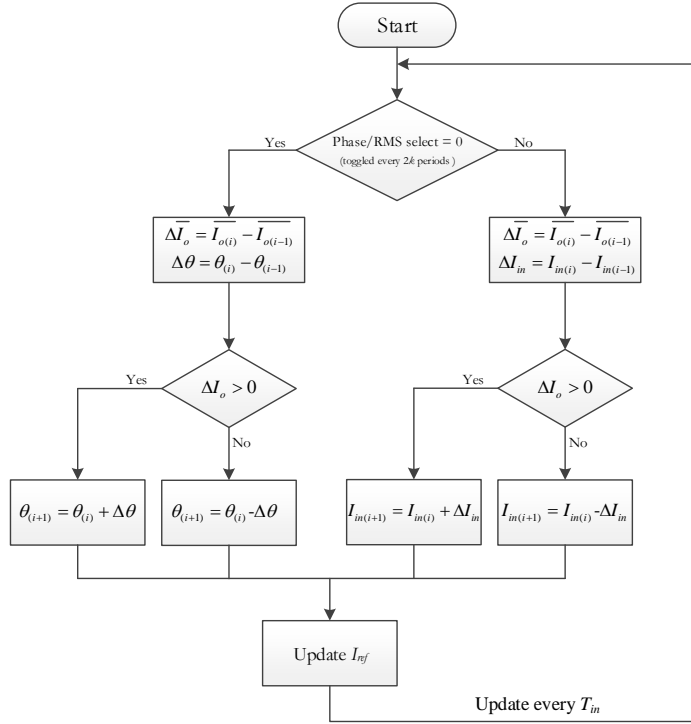
fixed and duty ratio is time varying in each line period. A new reference current is generated for I_{in} by the end of each line period based on known phase and RMS value. In the Quasi-MPPT method, the duty ratio is tuned directly (Fig. 4.13(b)). The duty ratio is fixed during every line cycle. If the output current increases compared to the previous line cycle, the duty ratio is tuned to the same direction, and vice-versa. The perturbation step of duty ratio is fixed. New duty ratio is updated by the end of each line period. In this section, explanation on how the proposed controller is implemented with the microprocessor is presented.

4.3.1 Current Sampling

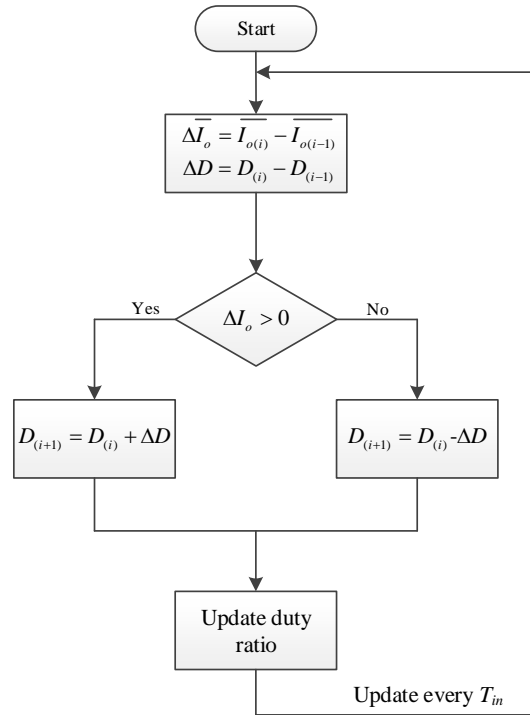
The input current i_{in} is measured using a current-sense resistor in series with the harvester input. The sensed current signal passes through an op-amp with an RC low pass filter and then feed to the ADC of the microprocessor. The sampling frequency of the input current i_{in} is the same as the switching frequency. There is no current-sense circuit for output current i_o although the proposed converter is designed to regulate i_o . The output current i_o is calculated by

$$\overline{i_{o(i)}} \approx \overline{i_{in(i)}}(1 - d_{(i)}) \quad (4.24)$$

where $\overline{i_{o(i)}}$ and $\overline{i_{in(i)}}$ are the average value of the output and input current over i^{th} switching period. When the harvester voltage is close to zero crossing, the converter cannot work in continuous current mode and this relation between input



(a) Phase/RMS MPPT



(b) Simplified quasi-MPPT

FIGURE 4.13: Proposed phase/RMS MPPT and quasi-MPPT control algorithm.

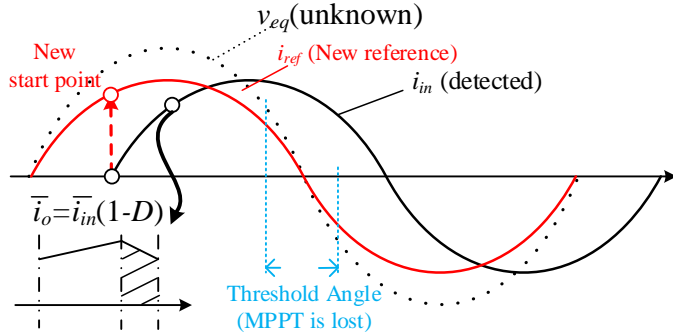


FIGURE 4.14: Tune the input current i_{in} /impedance z_{in} to achieve MPPT.

and output current is not valid. The output current during this period is ignored due to its small value and short time duration. This arrangement simplifies the design and reduces the power consumption of the converter.

4.3.2 Limitation on Conversion Ratio

Theoretically, the maximum power point is achieved when the input current is in phase with the harvester voltage v_{eq} and with appropriate RMS. So the reference current and the input current will gradually approach the phase of the harvester voltage and reach the stable state (Fig. 4.14). However, in the real application, the harvester impedance will not exactly satisfy (4.2), due to circuit nonlinearities. For example, suppose the diode voltage drop is V_D . The maximum power occurs at

$$i_{in}(t) = \frac{\sqrt{2}V_{eq} \cos(\omega_{in}t)}{R_w} \quad (4.25)$$

In order to simplify the calculation, AC effect is ignored in the analysis (assume $R_w \gg \omega_{in}L_{eq}$). According to the basic relations of boost converter under steady

state, the duty ratio is

$$d(t) = 1 - \frac{\sqrt{2}V_{eq}|\cos(\omega_{in}t)|}{2(V_o + 2V_D)} \quad (4.26)$$

When the input voltage is low, the MPPT is lost for duty ratio cannot become too close to 1 in real applications, and (4.26) can no longer be satisfied. If we consider the upper limit for the duty ratio is 0.9 and the threshold angle (Fig. 4.14) is 30° , then the design limitations for output voltage is roughly $V_o < 2.5V_p - 2V_D$. Suppose the output voltage V_o is fixed. When the harvester voltage is low, the duty ratio of both MPPT algorithms will approach D_{max} . In the proposed magnetic harvester, the input voltage increases with the input frequency (Fig. 3.12). Therefore, the controller shifts to fixed maximum duty ratio $D_{max} = 0.88$ when the frequency of the input current is detected to be lower than 40Hz. Because under such low frequency, v_{eq} is too low and most of the time in one line cycle the duty ratio will be D_{max} . (The inability to track the phase of the input line voltage due to limits on duty ratio is typical of design constraints found in power factor correction circuits [46].)

4.3.3 Current Reference (Phase/RMS)

In the analysis, the harvester equivalent voltage v_{eq} is assumed to be a sinusoid waveform where a sine table may be used as current reference table. However, in experiment, the output of the proposed rotational harvester actually contains

noticeable high order harmonics. So a sine table cannot be used directly to build the current reference table. The parameters of n^{th} order harmonics are defined as $v_{eq(n)}$, $i_{in(n)}$, $P_{in(n)}$ and etc. In the proposed harvester voltage, there is no even order harmonics. The maximum output power follows

$$P_{o_max} = \eta P_{in_max} = \eta P_{in(1)_max} + \eta P_{in(3)_max} + \eta P_{in(5)_max} + \dots \quad (4.27)$$

where $P_{in(n)_max}$ represents to the maximum input power of the n^{th} order harmonics. In order to achieve maximum output power, it requires all the high order harmonics achieve maximum power. For each harmonics, the requirements to achieve maximum power for phase and RMS value in (4.4) and (4.5) are still valid.

$$P_{in(n)} = (V_{eq(n)} I_{in(n)} \cos \theta_{(n)} - I_{in(n)}^2 R_w) \quad \left(-\frac{\pi}{2} < \theta_{(n)} < \frac{\pi}{2}\right) \quad (4.28)$$

So for the n^{th} order harmonic, the maximum power is achieved when it follows

$$\begin{cases} \frac{\partial P_{in(n)}}{\partial \theta_{(n)}} = V_{eq(n)} I_{in(n)} \sin \theta_{(n)} = 0 \\ \frac{\partial P_{in(n)}}{\partial I_{in(n)}} = V_{eq(n)} \cos \theta - 2I_{in(n)} R_w = 0 \end{cases} \Rightarrow \begin{cases} \theta_{(n)} = 0 \\ I_{in(n)} = \frac{V_{eq(n)}}{2R_w} \end{cases} \quad (4.29)$$

For a sinusoid waveform, $I_{in(n)} = \frac{V_{eq(n)}}{2R_w}$ is equivalent to $i_{in(n)} = \frac{v_{eq(n)}}{2R_w}$. The condition to achieve maximum output power is

$$\begin{cases} \theta = 0 \\ i_{in} = i_{in(1)} + i_{in(3)} + i_{in(5)} + \dots = \frac{v_{eq(1)} + v_{eq(3)} + v_{eq(5)} + \dots}{2R_w} = \frac{v_{eq}}{2R_w} \end{cases} \quad (4.30)$$

The methodology previously presented for the controller should remain valid and still produce maximum power extraction if the input current is in phase with v_{eq} waveform and has instantaneous value $v_{eq}/2R_w$. Thus, the input current reference table should be generated off-line from the shape of harvester equivalent voltage v_{eq} . According to harvester model (Fig. 4.4), it is assumed that the harvester equivalent voltage v_{eq} can be measured under open circuit condition. In order to avoid noise, the Fast Fourier Transform (FFT) is used to analyze the harvester open circuit voltage at each fundamental frequency and construct the current reference lookup table. Fig. 4.15(a) shows the FFT result of the harvester voltage at each frequency. The frequency and amplitude are normalized by the fundamental frequency and amplitude at fundamental frequency, respectively. In the lookup table, higher order harmonics ($7^{th}, \dots$) are ignored except for $1^{st}, 3^{rd}, 5^{th}$.

$$i_{ref} \approx \sqrt{2}I_{in(1)} \cos(\omega_{int}t + \theta_{(1)}) + \sqrt{2}I_{in(3)} \cos(\omega_{int}t + \theta_{(3)}) + \sqrt{2}I_{in(5)} \cos(\omega_{int}t + \theta_{(5)}) \quad (4.31)$$

It can be seen that the ratios of high order harmonics are close when the input frequency changes from 40Hz to 100Hz, so the shape of harvester equivalent voltage v_{eq} is assumed to be unchanged within the harvester operating range (40Hz-100Hz). The result of the constructed reference is shown in Fig. 4.15(b) at 80Hz.

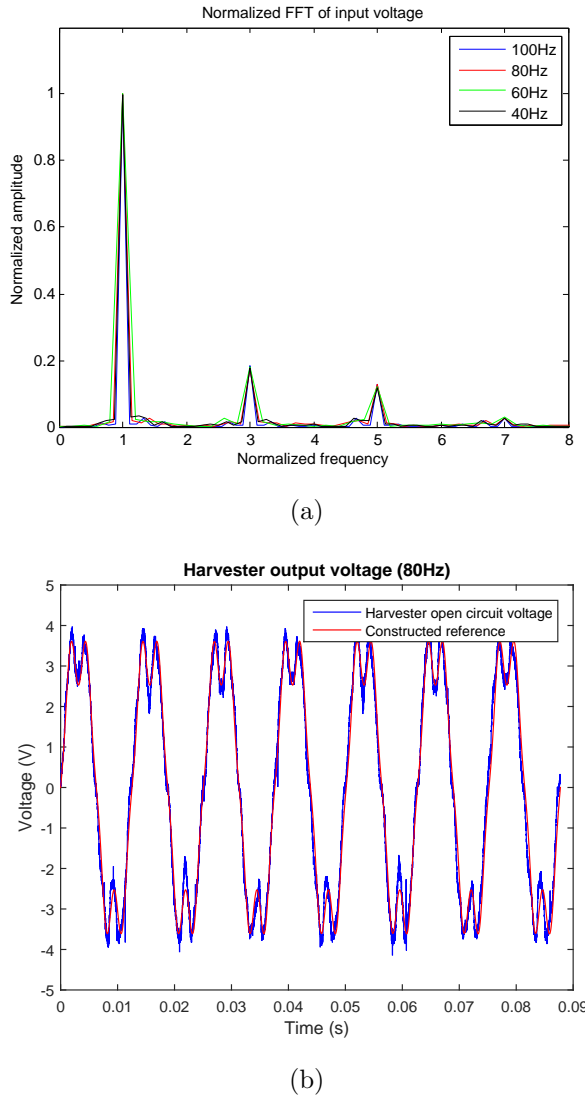


FIGURE 4.15: Construct the look up table for input current reference.

4.3.4 Frequency Tracking (Phase/RMS)

In the proposed prototype, the frequency of input voltage of the harvester may change from 0Hz to 110Hz. The period of i^{th} input voltage line cycle $T_{in(i)}$ is used for $(i + 1)^{th}$ cycle to calculate the switching frequency in $(i + 1)^{th}$ cycle. A lookup table with 256 points are constructed to generate the current reference. The switching cycle is updated at the beginning of each input period by detecting

the zero crossing of input current from negative to positive value.

$$T_{s(i+1)} = T_{s(i)} \cdot N/256 \quad (4.32)$$

N is the switching cycles counted in i^{th} input period. In this way, the switching frequency is maintained approximately 256 times as the harvester line frequency. It should be noted that if the input frequency jumps from multiple times of f to f , the proposed frequency tracking algorithm will not work properly since there is no voltage reference and the zero crossing of the input current i_{in} will still be maintained at the same position. However, in the proposed system, the input voltage frequency is directly proportional to the rotational speed, which changes continuously and slowly. It should not jump abruptly. Therefore, the frequency tracking algorithm using input current is feasible. Although the frequency jump is unlikely to happen, an algorithm is designed to correct wrong working frequency in case it happens. The harvester starts up with a fixed duty ratio ($D = 0.8$) to count the line frequency. During operation, the converter switches to the fixed duty ratio ($D = 0.8$) mode for a line period every two minutes to count the real line frequency. This algorithm keeps the converter always working under the real line frequency.

4.4 Stability Analysis

When the output current is tuned to the stable state, there will be small fluctuation around the maximum value because the controller is always searching for a maximum power point. In this section, the stability of the proposed control algorithm will be analyzed. V_{eq-q} and I_{in-q} are defined as quiescent value of v_{eq} and i_{in} at fixed time intervals, respectively.

In the harvesting system, the input voltage v_{eq} is an AC voltage source. In this case, it is assumed that the AC line variations are much slower than the converter dynamics, so that the rectifier always operates near equilibrium. The quiescent operating point changes slowly along the input sinusoid, and we can find the slowly-varying equilibrium duty ratio. The harvester voltage source v_{eq} thus changes to quiescent voltage V_{eq-q} (Fig. 4.16). To simplify the analysis, the basic boost topology will be used in this section instead of the one used in the paper. This substitution will not affect small signal analysis because the diode bridge is only designed for rectification. The battery is modeled as a resistor (R_b) in series with a DC voltage source V_b . The output current i_o used in the previous sections is the current going through the rectification diodes. In this section, the current fed into the battery i'_o will be used. Suppose the voltage across C_o is constant, in steady state, i'_o equals to the average of i_o over the input line period. No ESR or ESL value will be considered in this section.

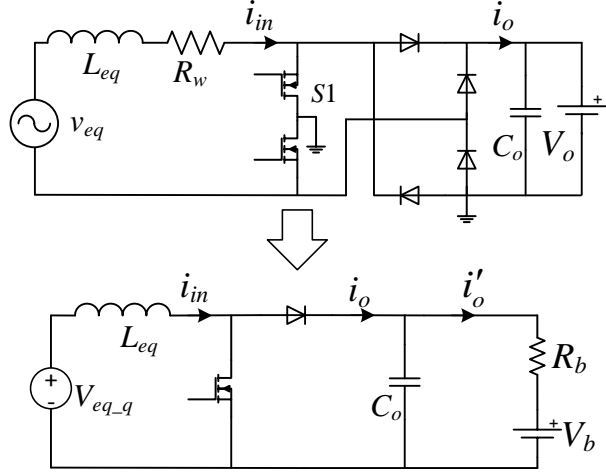


FIGURE 4.16: The proposed boost derived AC-DC converter is simplified.

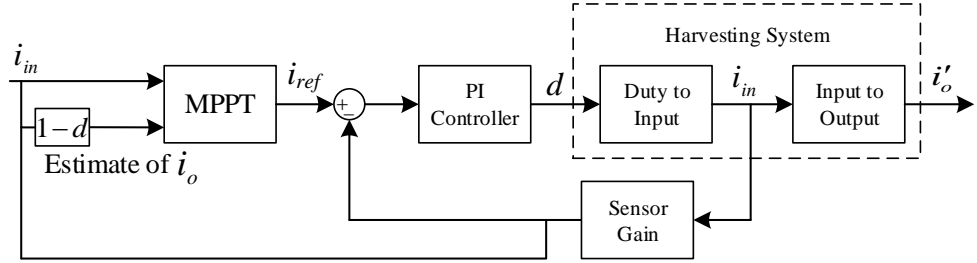


FIGURE 4.17: Block diagram of Phase/RMS MPPT algorithm.

Fig. 4.17 shows the block diagram of the proposed Phase/RMS control algorithm. For the inner loop, Small signal transfer functions of duty ratio to input current (G_{id}) is derived to analyze the close loop stability. For the outer loop, since the perturb and observe algorithm is used, at any given operation point after system settling time, outer loop can be considered as being in open loop control. Thus, it does not have stability issue. The open loop transfer function is the transfer function of input current to output current (G_{io}). The stability of the perturb and observe method is analyzed separately.

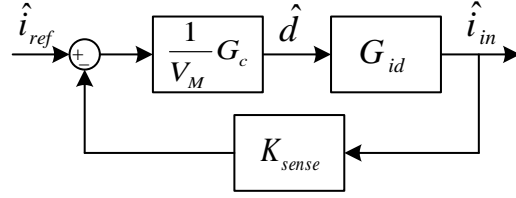


FIGURE 4.18: The inner loop.

4.4.1 Duty Ratio to Input Current $G_{id}(s)$

The inner loop is shown in Fig. 4.18. G_c is the compensator transfer function and $1/V_M$ is the modulator gain. In the experimentally implemented controller, PI compensator is used so that $G_c(s) = K_p + \frac{K_i}{s}$. Small signal duty ratio to input current transfer function G_{id} needs to be derived from space average model.

Fig. 4.19 shows the linear equivalent circuit for each state of the converter in continuous current mode. When MOSFET is on and diode is off (Fig. 4.19(a)):

$$L_k \frac{di_{in}}{dt} = V_{eq-q} \quad (4.33)$$

$$C_o \frac{dv_{C_o}}{dt} = -\frac{v_{C_o} - V_b}{R_b} \quad (4.34)$$

$$v_o = v_{C_o} \quad (4.35)$$

where V_{eq-q} is the harvester voltage at the quiescent operation point. When MOSFET is off and diode is on(Fig. 4.19(b)):

$$L_k \frac{di_{in}}{dt} = V_{eq-q} - v_{C_o} \quad (4.36)$$

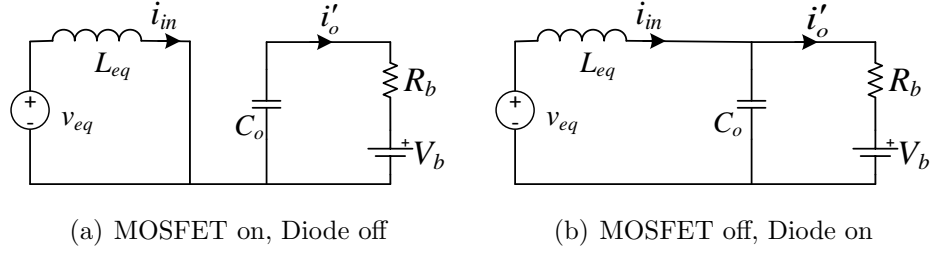


FIGURE 4.19: State space average model.

$$C_o \frac{dv_{C_o}}{dt} = i_{in} - \frac{v_{C_o} - V_b}{R_b} \quad (4.37)$$

$$v_o = v_{C_o} \quad (4.38)$$

The averaged state equations over a switching cycle are:

$$L_{eq} \frac{d\langle i_{in} \rangle}{dt} = V_{eq-q} - (1-d)\langle v_{C_o} \rangle \quad (4.39)$$

$$C_o \frac{d\langle v_{C_o} \rangle}{dt} = (1-d)\langle i_{in} \rangle - \frac{\langle v_{C_o} \rangle - V_b}{R_b} \quad (4.40)$$

$$\langle v_o \rangle = \langle v_{C_o} \rangle \quad (4.41)$$

where $\langle x \rangle = \frac{1}{T_{SW}} \int_t^{t+T_{SW}} x(t) dt$ and T_{SW} is the MOSFET switching period. To construct a small signal model at the quiescent operating point, the input current $\langle i_{in} \rangle$, capacitor voltage $\langle v_{C_o} \rangle$ and duty ratio d are assumed to be equal to their given quiescent values I_{in-q} , V_{C_o-q} and D_q plus superimposed small perturbation \hat{i}_{in} , \hat{v}_{C_o} and \hat{d} .

$$\langle i_{in} \rangle = I_{in-q} + \hat{i}_{in} \quad (4.42)$$

$$\langle v_{C_o} \rangle = V_{C_o-q} + \hat{v}_{C_o} \quad (4.43)$$

$$d = D_q + \hat{d} \quad (4.44)$$

Now (4.39)-(4.41) become:

$$L_{eq} \frac{d(I_{in(q)} + \hat{i}_{in})}{dt} = V_{eq-q} - (1 - D_q - \hat{d})(V_{C_o-q} + \hat{v}_{C_o}) \quad (4.45)$$

$$C_o \frac{d(V_{C_o-q} + \hat{v}_{C_o})}{dt} = (1 - D_q - \hat{d})(I_{in-q} + \hat{i}_{in}) - \frac{(V_{C_o-q} + \hat{v}_{C_o}) - V_b}{R_b} \quad (4.46)$$

Discarding the second order terms and taking Laplace transform leads to:

$$L_k \frac{d\hat{i}_{in}}{dt} = -(1 - D_q)\hat{v}_{C_o} + \hat{d}V_{C_o-q} \quad (4.47)$$

$$C_o \frac{d\hat{v}_{C_o}}{dt} = (1 - D_q)\hat{i}_{in} - \hat{d}I_{in-q} - \frac{\hat{v}_{C_o}}{R_b} \quad (4.48)$$

$$\hat{v}_o = \hat{v}_{C_o} \quad (4.49)$$

Change the equations from time domain to frequency domain

$$\hat{i}_{in}(s) = \frac{\hat{d}(s)V_{C_o-q} - (1 - D_q)\hat{v}_{C_o}(s)}{sL_{eq}} \quad (4.50)$$

$$\hat{v}_{C_o}(s) = \frac{(1 - D_q)\hat{i}_{in}(s) - \hat{d}(s)I_{in-q}}{sC_o + \frac{1}{R_b}} \quad (4.51)$$

$$\hat{v}_o(s) = \hat{v}_{C_o}(s) \quad (4.52)$$

From (4.50)-(4.52), the duty ratio to input current transfer function is derived as

$$G_{id}(s) = \frac{\hat{i}_{in}(s)}{\hat{d}(s)} = \frac{V_{o-q}C_o s + \frac{V_{o-q}}{R_b} + (1 - D_q)I_{in-q}}{L_{eq}C_o s^2 + \frac{L_{eq}}{R_b}s + (1 - D_q)^2} \quad (4.53)$$

The loop gain of the inner loop is

$$T(s) = \frac{1}{V_M} G_c(s) G_{id}(s) K_{sense} \quad (4.54)$$

A simple PI controller is easily derived using (4.53) and (4.54) in the experimental energy harvester. It is also sometimes helpful to realize (for outer loop) design that the closed loop transfer function of the inner loop is

$$T_{CL}(s) = \frac{T(s)}{1 + K_{sense}T(s)} \quad (4.55)$$

In low frequencies sufficiently below the bandwidth of $T_{CL}(s)$, then $T_{CL}(s) \approx \frac{1}{K_{sense}}$, since $|T(j\omega)| \gg 1$ for low frequencies.

4.4.2 Input Current to Output Current G_{io}

Suppose the perturb and observe algorithm is slow enough, and the converter moves from one reference current to another slowly. Once the system is settled to a given operation point, the outer loop can be considered as under open loop control. There is no given output current reference to feedback the output current

error to form a close loop control. So for the outer loop, no matter what the transfer function G_{io} is, the system is always stable if the inner loop is stable since there is no feedback loop at any determined operation point.

The transfer function of the outer loop at any determined operation point G_{io} can be calculate below. In the proposed circuit, $v_o = i'_o R_b + V_b$ (Fig. 4.16) leading to the small signal relationship

$$\hat{v}_o(s) = \hat{i}'_o(s) R_b \quad (4.56)$$

Therefore, the input current to output current transfer function G_{io} is obtained from combining (4.50), (4.51) and (4.56):

$$\frac{\hat{i}'_o(s)}{\hat{i}_{in}(s)} = \frac{\hat{v}_{Co}(s)}{R_b \hat{i}_{in}(s)} = \frac{(1 - D_q) - \frac{I_{in_q}}{G_{id}}}{s C_o R_b + 1} \quad (4.57)$$

4.4.3 Perturb and Observe Algorithm

As analyzed before, the system is alway stable at any operation point if the inner loop is stable and the perturb and observe method is sufficiently slow. However, the system require some settling time when it moves from one stable operation point to another. During the settling period, the system is not working at one certain operation point. The stability characteristics of perturb and observe algorithm has been studied on photovoltaic systems in [56, 57]. There are two factors related

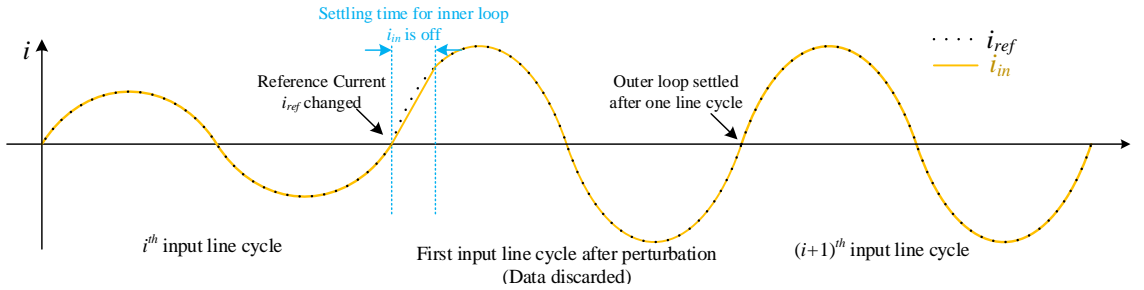


FIGURE 4.20: The perturbation settling time.

to the system stability: perturbation step size and perturbation sampling period. If the system settling time to the perturbation step signal is sufficiently shorter than the perturbation sampling period, the system is stable [57]. In the proposed system, since the inner loop is designed to track a changing reference current i_{ref} , the inner loop settling time to the step signal is much shorter than one input line period ($T_{in} \approx 256T_s$) as shown in Fig. 4.20. However, the average output current of one line period is calculated in the outer loop, so the average output current from first line period after perturbation is not accurate. The system should settle to the new stable operation point on the second line period after perturbation (Fig. 4.20). That means, if the perturbation sampling periods is more than two line period and the data from first line period after perturbation is discarded, the system should be stable. So if the perturbation is applied after one input line period, the data from the first line period followed is discarded due to the settling time shown in Fig. 4.20. The data from the second line period after perturbation is actually used. The converter should work in a stable operation point in the second line period after perturbation.

TABLE 4.1: Circuit parameters of the converter

Parameters	Model Type	Value
Harvester winding resistance		R_w 9.4Ω
MOSFET	AO7400	$R_{DS(on)}$ 75mΩ
Output capacitor		C_o 115μF
Output diode	NSR0320	V_f 0.23V
Current amplifier	INA286	

TABLE 4.2: Electrical performance of the system

Parameters	Nominal Value
Power Amplifier	
Input frequency (f_{in})	50Hz~100Hz
Open circuit voltage (v_{eq})	1.5VRMS~3VRMS
Magnetic Harvester	
Input frequency (f_{in})	40Hz~110Hz
Open circuit voltage (v_{eq})	1.28VRMS~3.5VRMS
Available input power (P_{in})	46mW@40Hz~325mW@110Hz
Boost Derived Converter	
Switching frequency (Phase/RMS)	$\sim 256 \cdot f_{in}$
Switching frequency (Quasi-MPPT)	25kHz
Output voltage (V_o)	3.6VDC

4.5 Experimental Results

A prototype of the power conversion circuit (Fig. 4.6) is built to verify the two proposed MPPT algorithms. The circuit parameters are shown in TABLE 4.1. The prototype is tested with different sources to evaluate the performance. The summary of the sources are listed in TABLE 4.2.

It is not possible to measure the harvester open circuit voltage v_{eq} during real

operation. This makes it difficult to verify whether the correct MPPT is achieved. Therefore, in order to validate control algorithms, a second, benchwork “approximate” prototype of the energy harvester according to its equivalent model is built with a signal generator followed by a power amplifier as a high-current buffer. We refer to this second prototype as ‘Power Amplifier’. A 3.3mH inductor with $\sim 7\Omega$ ESR is connected in series with the power amplifier to emulate the harvester equivalent inductance. The output voltage of the signal generator can be set between 1.5VRMS \sim 3VRMS and 50Hz \sim 100Hz corresponding to the harvester equivalent voltage v_{eq} and input frequency, respectively. Because the voltage of the Power Amplifier prototype can be measured and its inductance is known, the accuracy of the proposed MPPT methods can be evaluated.

On the power amplifier prototype, the proposed Phase/RMS MPPT algorithm (Fig. 4.8) regulates the input current i_{in} (Fig. 4.21) as desired. When the input voltage is close to zero crossing, the input current cannot follow the voltage due to maximum duty ratio limit ($D_{max} = 0.88$). The zero crossing limit time is shorter when the input voltage increases from 1.5VRMS to 3VRMS. The dataset of shown waveforms in Fig. 4.21 is exported from the oscilloscope to Matlab to calculate the average input power and the power factor from v_{eq} and i_{in} . The input power is calculated by taking the average of the products of i_{in} and v_{eq} . The results show that the proposed method achieves 77mW input power at 1.5VRMS ($P_{in(max)}=82.4\text{mW}$) and 288mW at 3VRMS ($P_{in(max)}=320\text{mW}$), both are around 90% of the theoretical maximum power defined by (4.6). Suppose v_{eq} contains

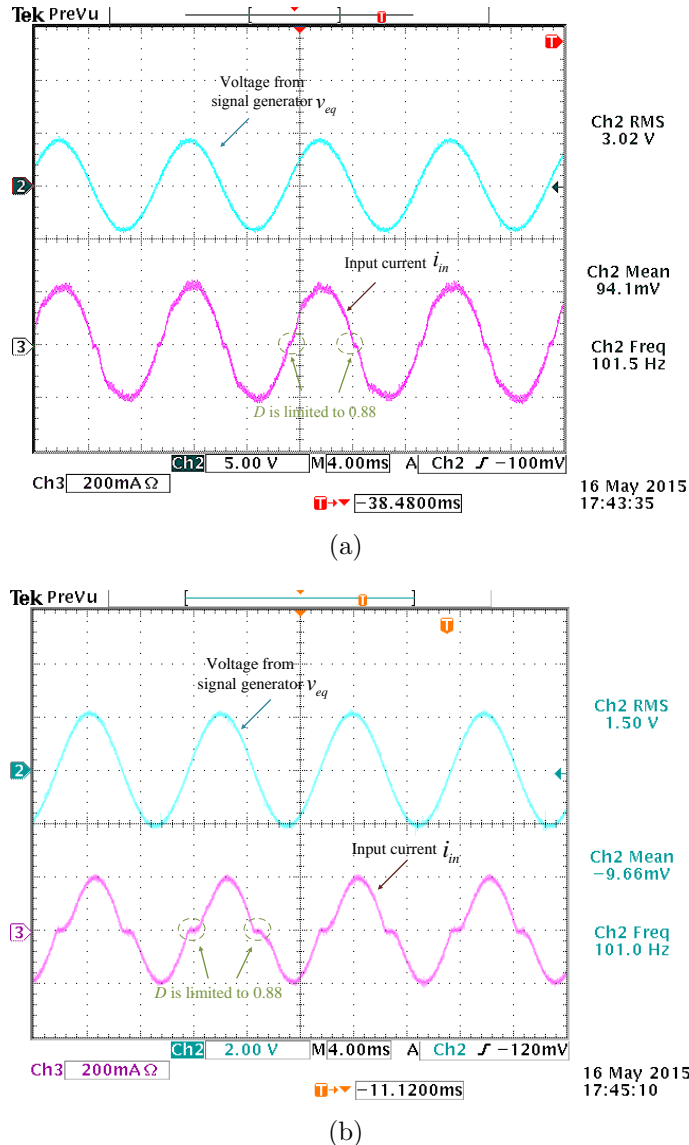


FIGURE 4.21: Experimental results of power amplifier (Phase/RMS MPPT): $f_{in} = 100\text{Hz}$; X-axis: 4ms/div; Y-axis: (a) Ch2: $v_{eq} = 3\text{VRMS}$, 5V/div; Ch3: i_{in} , 200mA/div; and (b) Ch2: v_{eq} , 1.5VRMS, 2V/div; Ch3: i_{in} , 200mA/div.

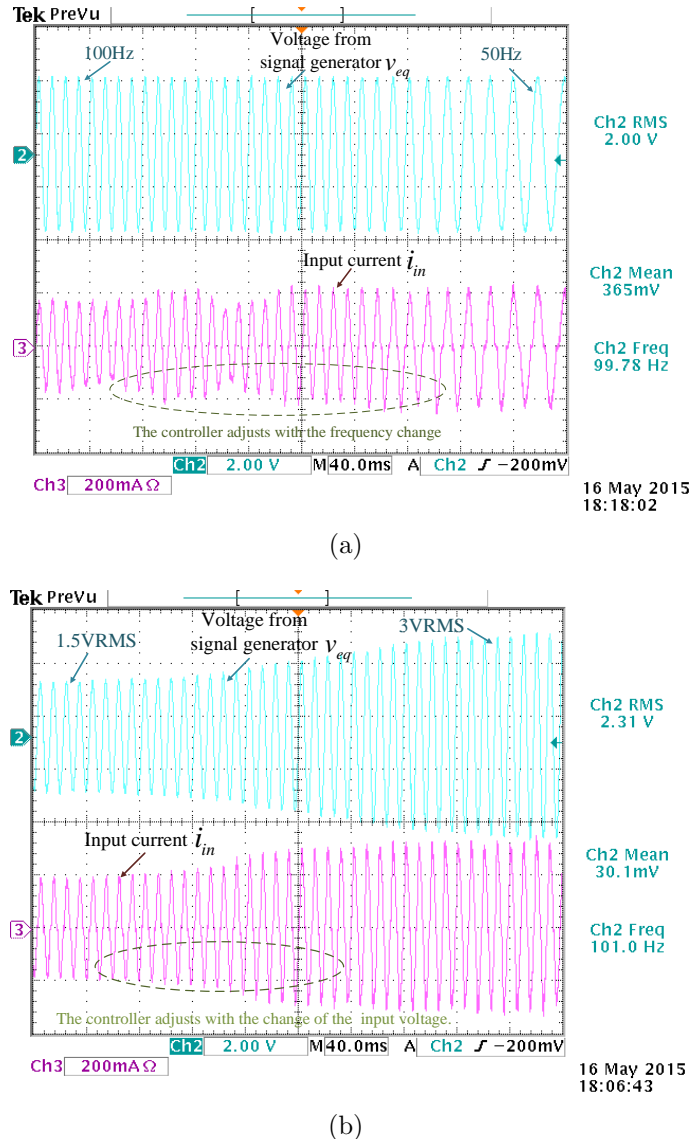


FIGURE 4.22: Experimental results of power amplifier (Phase/RMS MPPT): X-axis: 40ms/div; Y-axis: (a) f_{in} from 100Hz to 50Hz; Ch2: $v_{eq} = 2\text{VRMS}$, 2V/div; Ch3: i_{in} , 200mA/div; and (b) v_{eq} from 1.5VRMS to 3VRMS; Ch2: v_{eq} , 2V/div; Ch3: i_{in} , 200mA/div.

no high order harmonics (i.e., $V_{eq} = V_{eq(1)}$ in our power amplifier prototype), the power factor is defined by

$$PF = \frac{P}{S} = \frac{V_{eq(1)}I_{in(1)}\cos\theta_{(1)}}{V_{eq(1)}\sqrt{I_{in(1)}^2 + I_{in(3)}^2 + I_{in(5)}^2 + \dots}} = \frac{I_{in(1)}\cos\theta_{(1)}}{I_{in}} \quad (4.58)$$

The experimental measured power factor of the proposed method is 0.97 for 1.5VRMS and 0.99 for 3VRMS, respectively. This indicates that the controller is working to keep the harvester current in phase with its voltage, which is a goal for the MPPT. The experimental waveforms with change of input voltage amplitude and frequency are illustrated in Fig. 4.22. The proposed converter adapts to the change and adjusts the amplitude/frequency of the input current as designed in the MPPT. The sinusoid waveform is used to construct the lookup table of the current reference i_{ref} when the power amplifier circuit is connected. In summary, the experiments with the power amplifier prototype demonstrate: 1) MPPT is nearly achieved, although there are errors due to the nonlinearities of the circuit; 2) higher voltage inputs may have reduced nonlinearities; and 3) the MPPT controller is able to track input frequency and voltage disturbances.

To verify the circuit performance with the actual roller skate magnetic harvester, the inductive magnetic energy harvester (Fig. 2.1(b) and Fig. 2.8), as described above, has been built for experiments. The open circuit voltage v_{eq} with frequency is shown in Fig. 3.12. The converter is tested with the harvester under different frequency. The output voltage V_o , input current i_{in} and output current i_o are

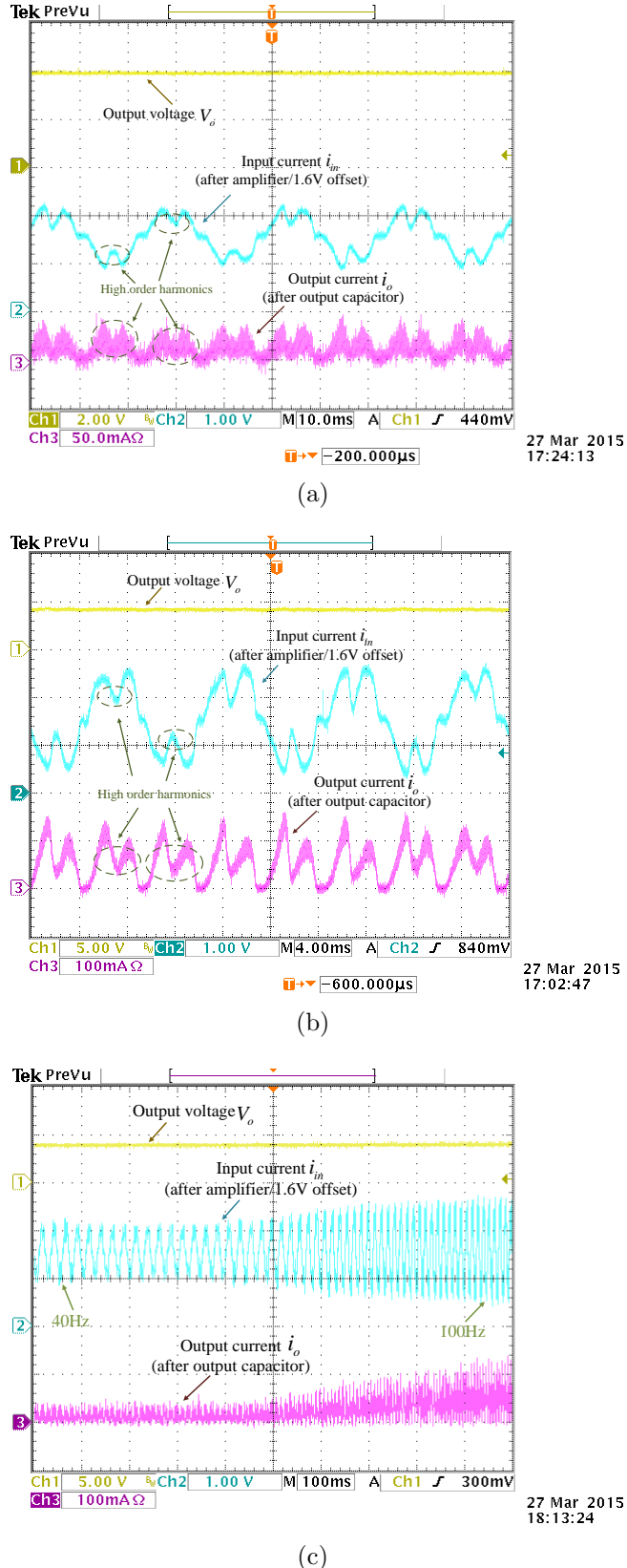


FIGURE 4.23: Experimental waveforms of magnetic harvester (Phase/RMS MPPT): X-axis: (a) 10ms/div; (b) 4ms/div; (c) 100ms/div; Y-axis: (a) $f_{in} = 40\text{Hz}$; Ch1: V_o , 2V/div; Ch2: i_{in} , 1V/div(250mA/div); Ch3: i_o , 50mA/-div; (b) $f_{in} = 100\text{Hz}$; Ch1: V_o , 5V/div; Ch2: i_{in} , 1V/div(250mA/div); Ch3: i_o , 100mA/div; (c) f_{in} from 40Hz to 100Hz; Ch1: V_o , 5V/div; Ch2: i_{in} , 1V/-div(250mA/div); Ch3: i_o , 100mA/div.

measured, as depicted in Fig. 4.23. The input current is sensed by a 0.04Ω resistor and a current amplifier with $100V/V$ gain. The waveform of input and output current are not sinusoid waveform due to high order harmonics in the harvester voltage. Similar to the input current with power amplifier, it cannot follow the input voltage during zero crossing due to maximum duty ratio $D_{max} = 0.88$.

Fig. 4.23(c) shows how the Phase/RMS MPPT algorithm adjusts the input current to track the change of the frequency and amplitude of the input voltage. The harvester input line frequency changes from 40Hz to 100Hz in about 500ms. At the same time, the RMS value of the harvester equivalent voltage v_{eq} changes from 1.28V to 3V. As mentioned in Section 4.3.4, the input voltage period is updated every input line cycle. Since the harvester line frequency changes gradually, the frequency of the input current i_{in} quickly adjusts from 40Hz to 100Hz. The proposed algorithm adjusts the phase and RMS value alternatively to find a new maximum power point. It can be seen from Fig. 4.23(c), compared to the frequency, it takes longer time (about 150ms more) for the system to settle to a new maximum power point.

In Fig. 4.24, the average output current i_o of the two proposed MPPT control methods are compared with the fixed duty ratio control at each frequency [11, 15]. Due to the battery load connected, it is equivalent to output power comparison. It can be seen that at each frequency, the proposed control method can always maintain the output current at a higher level. The proposed methods increase the output current from 47.2mA ($D = 0.8$) to 65.1mA (Phase/RMS) and

62mA (Quasi-MPPT) at 110Hz; and increase the output current from 1.78mA ($D = 0.6$) to 9.02mA (Phase/RMS) and 8.97mA (Quasi-MPPT) at 40Hz, respectively. The experimental results show that the output current of the Quasi-MPPT is close to Phase/RMS algorithm. There are three reasons may cause the result:

- 1) In the proposed harvester, $R_w \gg \omega_{in}L_{eq}$. R_w is 9.4Ω and L_{eq} is around 3mH working at around 100Hz. As shown in (4.6) and Fig. 4.12, when the harvester is more resistive, the best power from Quasi-MPPT method approaches Phase/RMS MPPT. The extracted power is even closer at the low frequency region.
- 2) The harvester voltage v_{eq} is low compared to the output voltage. As shown in Section 4.3.2, if the conversion ratio is high, the duty ratio is always limited by the maximum duty ratio D_{max} . Especially at low frequency region, which means low harvester voltage in the proposed system, the Phase/RMS method is limited by D_{max} for a long time during one line period and the Quasi-MPPT works close to or is also limited by D_{max} , the output power of the two method will be close.
- 3) The voltage and frequency of the input voltage from the harvester is not stable. Since the magnets and coils cannot be designed to be ideally symmetric, the frequency jitter of the harvester input voltage lowers system output power more on Phase/RMS method than Quasi-MPPT method due to its dependence on the shape of the input.

The output power of the proposed methods is compared with the maximum available power as shown in Fig. 4.25. The maximum available power is measured by connecting a 9.4Ω resistor, which equals to the harvester internal coil resistance,

to the harvester and measuring the power across it. Similar to the maximum available AC power, the converter output power also increases with the square of the voltage. The converter becomes more essential to harvester energy when the input voltage increases due to fixed power loss on control and current sensing circuit. The converter power loss is estimated by measuring the input and output current, and then calculating the power loss on the switching devices, control and current sensing circuit. The estimated converter efficiency is 82.4% (Phase/RMS) at 110Hz with power loss analysis. If the harvester maximum output power shown in (4.6) is considered as the base, the harvesting efficiency is 78.1%. This harvesting efficiency is close to the estimated converter efficiency, that is to say, the system operation point is close to the maximum power point. The efficiency reported from the latest MPPT algorithm designed for magnetic energy harvester was previously around 63% [37]; yet due to lower harvester voltage in [37], the efficiency is only listed here for reference, as it is not a fair comparison.

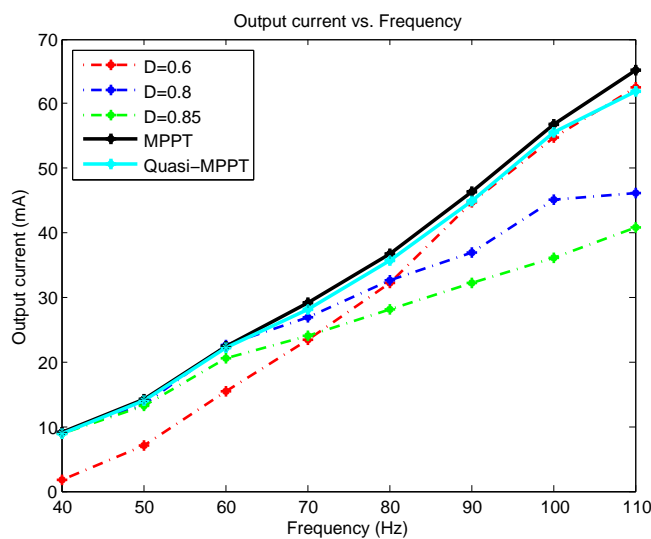


FIGURE 4.24: Output current vs. Frequency.

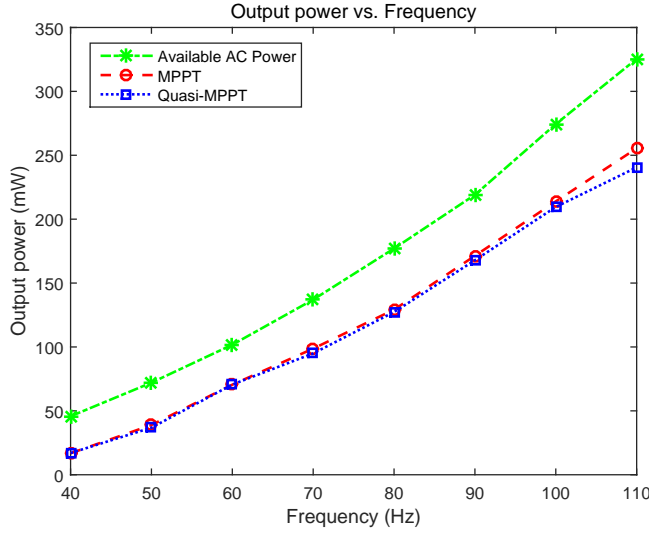


FIGURE 4.25: Output power vs. Frequency.

4.6 Dynamic Input Voltage/Frequency

In order to make a fair comparison between the two proposed MPPT algorithms and the conventional PWM based MPPT algorithm [1, 2, 23, 37, 43, 44], both MATLAB/Simulink simulation models and experimental setups are utilized for testing based on the rotational harvester shown in Fig. 2.8 and circuit parameters shown in Table 4.1. As shown in Fig. 4.26, a changing equivalent voltage source is applied to the harvesting system to represent the change of the harvester rotational speed. The equivalent voltage ramps from 3VRMS to 5.8VRMS and the frequency ramps from 100Hz to 200Hz according to the open circuit voltage measured from proposed rotational harvester. The RMS value and the frequency ramps up for 0.25s, keeps constant at 200Hz/5.8VRMS for 2s, ramps down for 0.25s, and remains at 100Hz/3VRMS for 2s. Three MPPT algorithms, Phase/RMS MPPT, Quasi-MPPT and conventional PWM based MPPT, are applied to the converter.

The average power is calculated by taking average of the instantaneous power on the 7V battery load over the 4.5 seconds. This 7V battery is a typical voltage level of two charging depleted Li-ion batteries (4.2V based) operated in series.

The system average output power is presented in this section using three methods:

- 1) MATLAB/Simulink simulation; 2) sinusoidal voltage with Chroma AC source and 3) rotational harvester shown in Fig. 2.8, which contains non-sinusoidal and nonlinear harmonics.

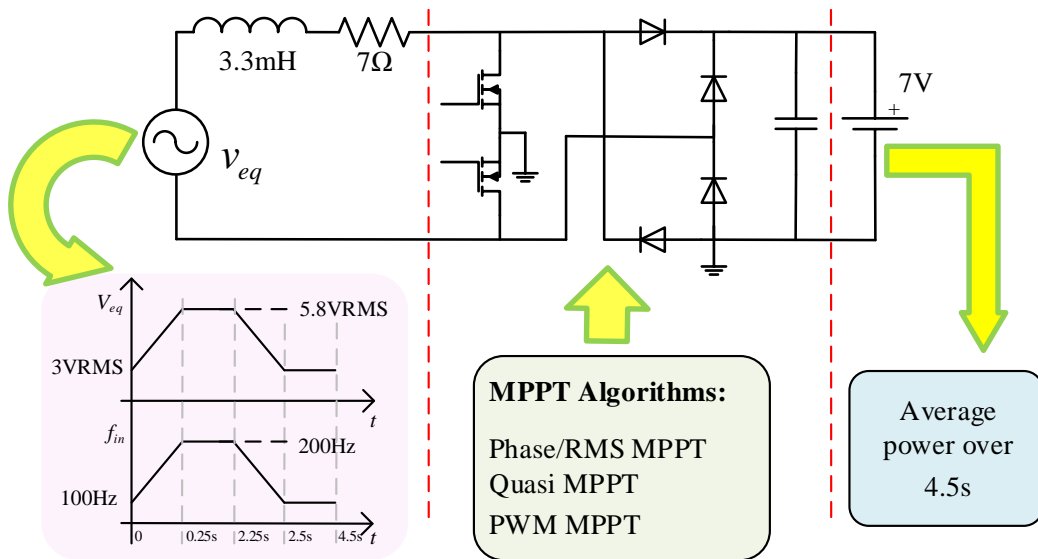


FIGURE 4.26: Block diagram of MPPT algorithms comparison.

4.6.1 Simulation

MATLAB/Simulink models are built according to Fig. 4.26. The circuit parameters are shown in Table 4.2 and include estimates of the switch losses in the simulation models. In the Phase/RMS algorithm, the RMS value and the phase

of the reference current are changed alternatively at the end of each line period as shown in Fig. 4.27. The first plot is the equivalent voltage of harvester. It ramps up from 3VRMS@100Hz to 5.8VRMS@200Hz in 0.25s, keeps at 5.8VRMS@200Hz for 2s, ramps down from 5.8VRMS@200Hz to 3VRMS@100Hz in 0.25s, and then remains constant at 3VRMS@100Hz for 2s. Fig. 4.27(a), (b) and (c) are the maximum power point tracking scheme of Phase/RMS MPPT, Quasi-MPPT and conventional PWM based MPPT algorithm, respectively. As shown in Fig. 4.27(a), Phase/RMS algorithm adjusts the phase and RMS value alternatively by the end of each line cycle. Fig. 4.27(b) shows the duty ratio is changed by the end of each line period in the Quasi-MPPT algorithm. Fig. 4.27(c) shows in the PWM based MPPT method, since the line voltage condition is not detected, the frequency to update the duty ratio is set to 1/10 of the lowest line frequency, so the conventional PWM based MPPT methods [1, 2, 23, 37, 43, 44] update at frequency 10Hz. It can be seen from Fig. 4.27 that the dynamic response to the change of the line conditions of both proposed MPPT algorithms are faster than the conventional PWM based MPPT algorithm. The steady state duty ratio of Quasi-MPPT method is around 0.55 at 200Hz and 0.75 at 100Hz, which is close to the steady state duty ratio of conventional PWM based MPPT algorithm. As shown in Fig. 4.28, the duty ratio of Phase/RMS method varies during one line period to track the change of the reference current. The maximum duty ratio for the simulation is set at $D_{max} = 0.88$. When the RMS value V_{eq} is higher, the duty ratio of Phase/RMS method varies in larger range. According to (4.8), the duty ratio in one line period

changes from 0.32 to 1 at 200Hz, and the duty ratio changes from 0.68 to 1 at 100Hz, respectively. Considering the different circuit parameters in calculation and simulation, the calculated results matches the simulation results.

The duty ratio of Quasi-MPPT method is fixed during every line cycle and updated by the end of each cycle. When the RMS value V_{eq} is high, the duty ratio becomes smaller, and matches Fig. 4.12. According to the theoretical ideal (no loss) maximum values shown in Fig. 4.12, the optimal duty ratio of Quasi-MPPT is 0.55 at 200Hz and 0.75 at 100Hz. In the simulation, the duty ratio of Quasi-MPPT method is around 0.56 at 200Hz and 0.76 at 100Hz. Considering the power loss on the switching devices, the simulation results can be seen as consistent as calculation. Finally, for the conventional PWM based MPPT method, $d(t)$ is updated every 0.1s and the steady state value is close to Quasi-MPPT method.

Fig. 4.29 shows the instantaneous power of three MPPT algorithms. The output power of three methods increases as the frequency ramp up during the time interval 0s to 0.25s, keeps high output power at 200Hz for 2s, and then decreases the power as the frequency ramps down during the time interval 2.25s to 2.5s, the power remains low output power at 100Hz for 2s. Over the 4.5s, the Phase/RMS MPPT algorithm has highest output power among the three methods. The average power over the 4.5s is 602.1mW. The average power of the Quasi-MPPT method and the PWM based MPPT method is 536.5mW and 516.7mW, respectively. Compared to the conventional PWM based MPPT method, the Phase/RMS MPPT method enhances the output power by 16.5% and the Quasi-MPPT method enhances the

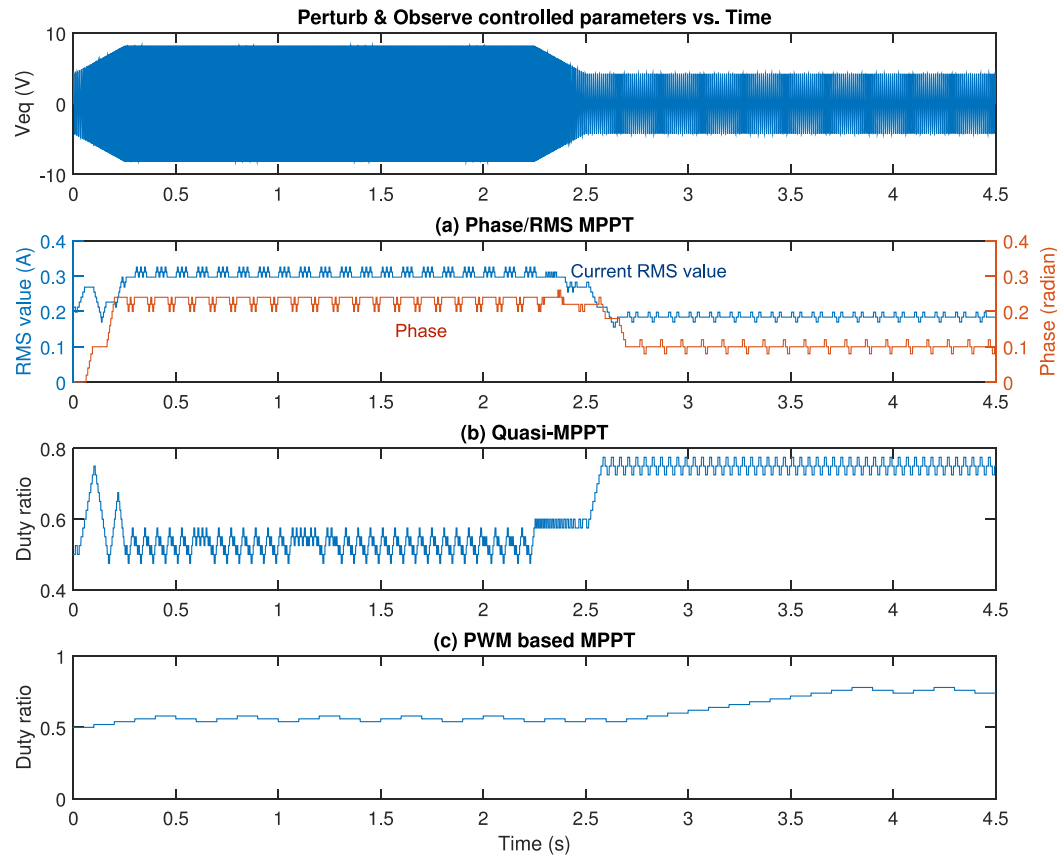


FIGURE 4.27: The Perturb & Observe controlled parameters vs. Time.

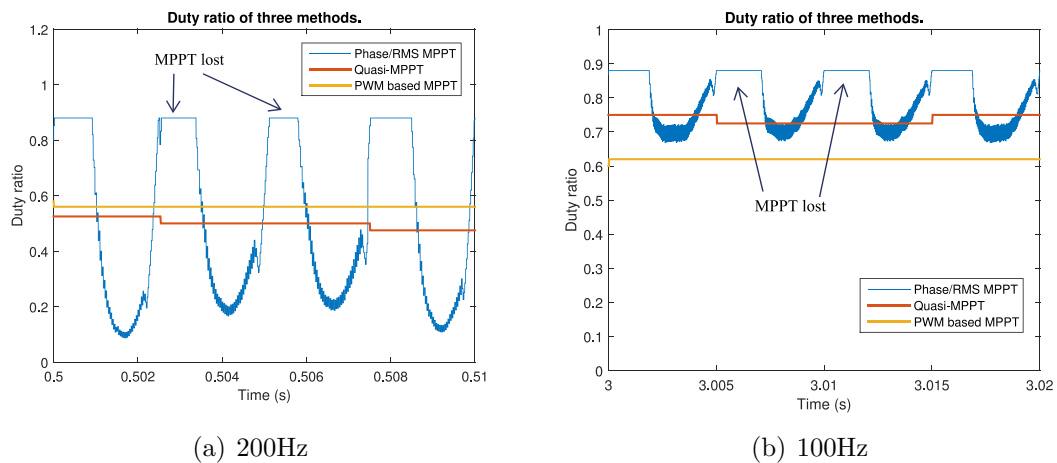


FIGURE 4.28: The duty ratio of three methods

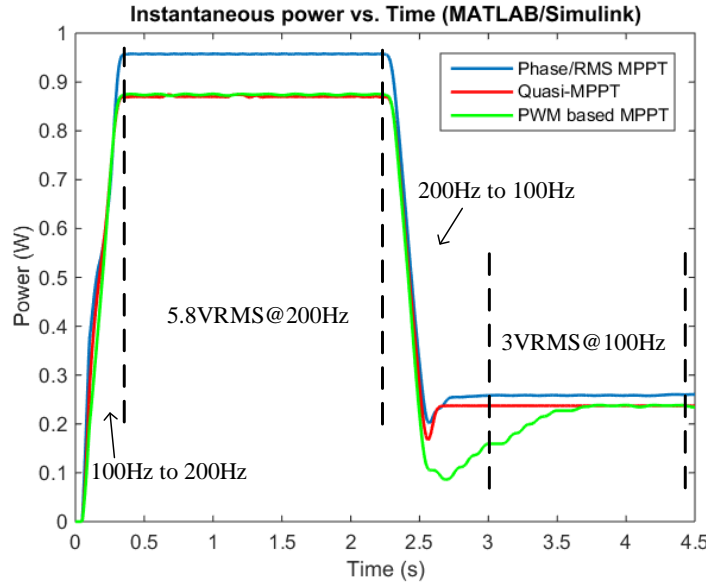


FIGURE 4.29: Instantaneous power of Phase/RMS MPPT, Quasi-MPPT and PWM based MPPT method (MATLAB/Simulink).

TABLE 4.3: Output power of three methods

f_{in}	Phase/RMS		Quasi-MPPT		PWM based MPPT	
	Simulation	Ideal	Simulation	Ideal	Simulation	Ideal
100Hz	258mW	321mW	236mW	287mW	236mW	287mW
200Hz	958mW	1200mW	858mW	987mW	875mW	987mW
Overall (4.5s)	602.1mW	760mW	536.5mW	637mW	516.7mW	637mW

output power by 4%. The influence of the frequency on the different MPPT approaches can be seen from the simulation (Fig. 4.29). The output power of the three methods is shown in Table 4.3. The theoretical values of Phase/RMS MPPT is calculated by (4.3). The theoretical values of Quasi-MPPT method is based on the simulation results with ideal circuit parameters shown in Fig. 4.12. In the steady state, the conventional PWM based MPPT method has the same theoretical ideal output power with the Quasi-MPPT method, so it is also based on Fig. 4.12.

The simulation results show the Quasi-MPPT method harvests 91% of output power compared to the Phase/RMS method in both 100Hz and 200Hz input frequency. It is caused by two reasons: 1) The operating frequency is low and $\omega_{in}L_{eq}$ is much less than R_w . As shown in Fig. 4.12, when the harvester is more resistive, the theoretical output power of Quasi-MPPT method increases, approaching 92% of the theoretical maximum power of the Phase/RMS method. By theory, the Quasi-MPPT method may reach higher output power. 2) Duty ratio clamping effect. Phase/RMS method extracts around 80% of the output power compared to its theoretical maximum under both 100Hz and 200Hz input voltage. And the Quasi-MPPT method extracts 82% and 87% of the output power compared to its theoretical maximum under 100Hz and 200Hz input voltage frequency, respectively. The circuit parameters for the two methods are the same shown in Table 4.2. The possible reason may be the maximum duty ratio clamp. As discussed in Section 4.3.2, the converter duty ratio increases when the input voltage is low and will be clamped to D_{max} if the input voltage is sufficiently low. During D_{max} clamping period, the maximum power point cannot be tracked. As shown in Fig. 4.28, when the input voltage is low, the duty ratio of the Phase/RMS MPPT method is clamped to $D_{max} = 0.88$. The maximum power point cannot be tracked fully for the Phase/RMS method. In contrary, the optimal duty ratio of the Quasi-MPPT method is the average of the Phase/RMS duty ratio, which is not clamped to D_{max} . Thus, the Quasi-MPPT method is less affected by the duty ratio clamping effect and extracts higher amount of power from its theoretical

maximum.

4.6.2 Experiments

Experimental test beds are built according to Fig. 4.26. The proposed two methods and conventional PWM based method are tested with both the programmable AC source with pure sinusoidal voltage and the rotational energy harvester containing real-world nonlinearities. The experimental results are presented and analyzed in this section.

4.6.2.1 Experiment 1: Programmable AC Source

A Chroma programmable AC source is used as the source instead of the harvester in this section. The Chroma AC source is connected to a 3.3mH inductor (parasitic resistance 7Ω) to emulate the rotational harvester. The equivalent pure sinusoidal voltage ramps up and down from 3VRMS to 5.8VRMS and the frequency ramps from 100Hz to 200Hz as the same as the in the simulation as shown in Fig. 4.26. The voltage ramps up and down for eight rounds. The output power is calculated by taking average of instantaneous power over the time to complete 8 up and down ramp tests of Fig. 4.26. Both the Phase/RMS and Quasi-MPPT methods update the controlled parameters at the end of each line period. The conventional benchmark PWM based MPPT method updates the duty ratio at 10Hz.

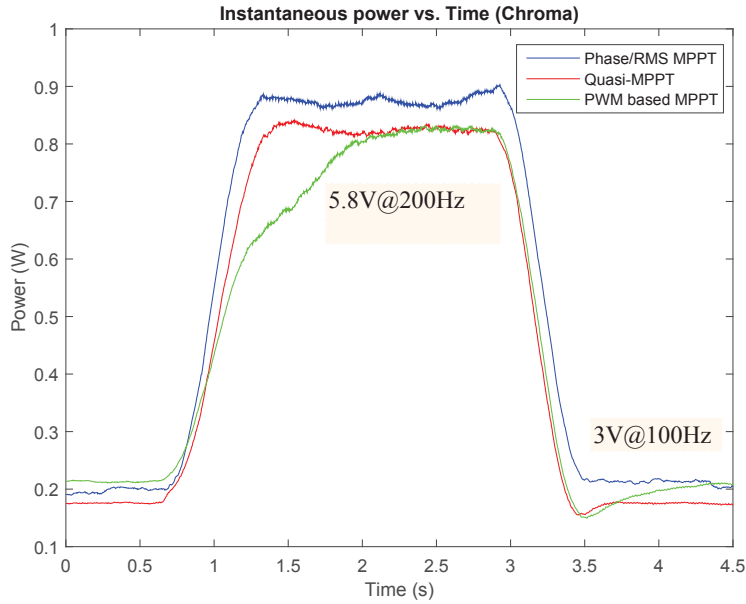


FIGURE 4.30: Instantaneous power of Phase/RMS MPPT, Quasi-MPPT and PWM based MPPT method (Chroma AC source).

Fig. 4.30 shows the instantaneous power of three MPPT algorithms. It is calculated by taking average of 8 rounds instantaneous output power. The Phase/RMS MPPT algorithm has highest output power among the three methods. The average power is 537.6mW. The average power of the Quasi-MPPT method and the PWM based MPPT method is 482.4mW and 474.3mW, respectively. Compared to the conventional PWM based MPPT method, the Phase/RMS MPPT method enhances the output power by 13.3% and the Quasi-MPPT method enhances the output power by 1.7%. This 1.7% improvement is likely smaller than the measurement error. As shown in Fig. 4.30, both Phase/RMS MPPT and Quasi-MPPT have faster response to the dynamic load. In the high frequency region, the experimental results show that the Phase/RMS method has higher output power, slightly above the measurement error. In the low frequency region, the result shows

the output power of Phase/RMS method and PWM base MPPT method is similar, about 20mW higher than the Quasi-MPPT method. Considering 7V output voltage, the difference of output current is less than 3mA, within the measurement error of current probe. Three methods can be considered as having similar output power. It is due to reasons analyzed in Section 4.5: 1) Output power of three methods is closer when the harvester is more resistive in low frequency region; 2) The switching loss makes duty ratio approach D_{max} and lowers the prominence of Phase/RMS MPPT. The experiment results with Chroma AC source verify both analytic and simulation results.

4.6.2.2 Experiment 2: Real Rotational Harvester

The rotational harvester shown in Fig. 2.8 is used as the source in this section. In the real harvester, nonlinearities, higher order harmonics and frequency jitter are unavoidable. The equivalent circuit of the proposed rotational harvester is an AC source with high order harmonics in series with an 3.12mH inductor and a 9.4Ω resistor. The frequency of the harvester open circuit voltage ramps from 100Hz/3VRMS to 200Hz/5.75VRMS in this test. The frequency ramps up for 0.25s, stay at 200Hz/5.8VRMS for 2s, ramps down for 0.25s and stay at 100Hz/3VRMS for 2s. The output power is calculated by taking average of ramp up/down for eight rounds.

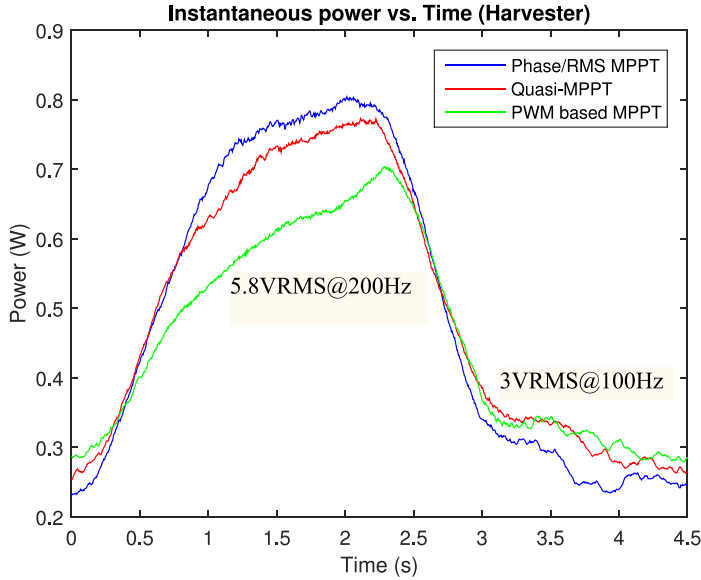


FIGURE 4.31: Instantaneous power of Phase/RMS MPPT, Quasi-MPPT and PWM based MPPT method (Harvester).

Fig. 4.31 shows the instantaneous power of three MPPT algorithms over one round. In the high frequency range, the difference of Phase/RMS method and Quasi-MPPT is less than theoretically predicted, and possible explanation are below. However, both the proposed methods harvest more power than the conventional PWM MPPT baseline. The average output power from Phase/RMS MPPT, Quasi-MPPT and PWM based MPPT method is 496.3mW, 495.4mW and 459.9mW, respectively. The Phase/RMS MPPT and Quasi-MPPT method has similar output power, essentially within measurement error. In theory, this should not happen, but in practicality the roller skate harvester is non-ideal and leads to several possible difficulties that can be explained:

1. There is instability of the input line frequency. As analyzed in Section 4.5, The magnets and coils of the harvester are not ideally symmetric, so the

frequency is not constant. The frequency jitter lowers the output power of Phase/RMS method, but it has less effect on the Quasi-MPPT method. The frequency jitter is more severe when the frequency increases. This can be seen, also in the simulations in Fig. 4.32. In the MATLAB/Simulink model, a random noise is added to the voltage source to simulate the frequency and voltage jitter of the harvester line voltage. The equivalent voltage is 5.8 ± 0.1 VRMS at $200\text{Hz} \pm 5\text{Hz}$ and the simulation results is shown in Fig. 4.32. The average output power of Phase/RMS method drops from 1.35W to 1.22W, but the output power of Quasi-MPPT method is almost unchanged. Therefore, the Phase/RMS method is more applicable to systems without frequency jitter cycle per cycle. Actually, if the roller blade were a commercial product that was precisely manufactured with equispaced magnets, then it is expected that the Phase/RMS method would improve more over the Quasi-MPPT. This is substantiated by the Experiment 1 and these simulation results.

2. The voltage shape changes over time. As shown in Fig. 4.33, the shape of the harvester open circuit voltage changes from one period to another period. It becomes severe when the frequency increases from 100Hz to 200Hz. The pre-made reference lookup table does not match all of them. The FFT analysis is calculated based on the average waveform of several periods (Fig. 4.34). A larger radius spindle is used in this experiment in order to increase harvester voltage frequency from 100Hz to 200Hz, so the high order harmonics shown

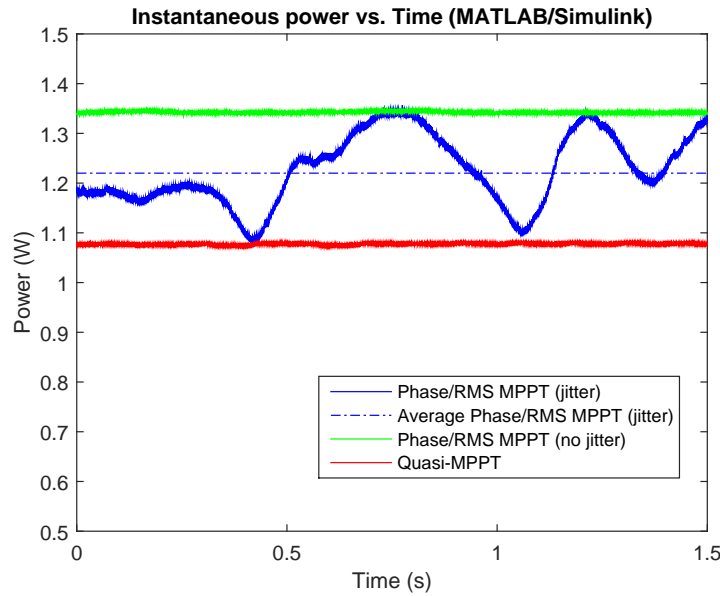


FIGURE 4.32: Frequency jitter lowers the output power.

in (Fig. 4.34 is slight different from Fig. 4.15(a)). The reference current lookup table changes with it accordingly. The shape change will not affect Quasi-MPPT method, but might lower the output of the Phase/RMS MPPT method. Both of the proposed MPPT algorithms have 8% improvement compared to the conventional PWM based algorithm. From Fig. 4.31, it can be seen that the PWM based method has slower response to the line condition change, as expected.

4.7 Conclusion

In this chapter, several typical MPPT control algorithm for inductive magnetic harvester are reviewed and two new MPPT control algorithm are introduced.

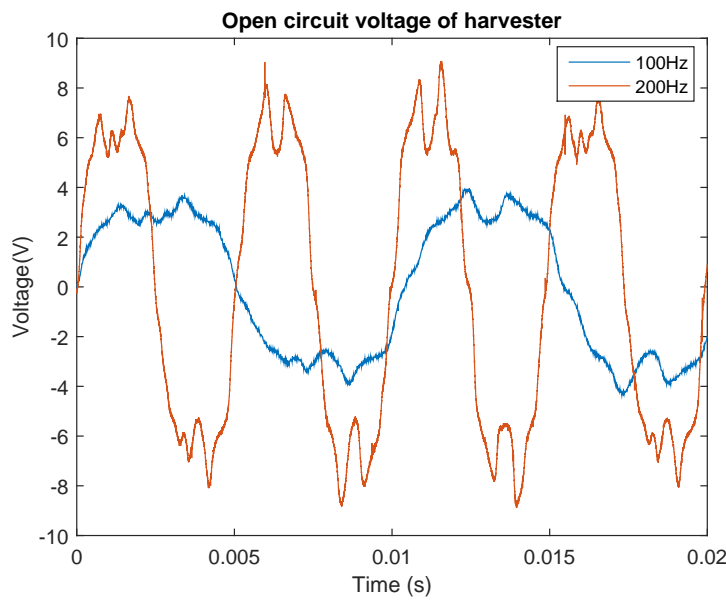


FIGURE 4.33: Harvester open circuit voltage at 100Hz and 200Hz.

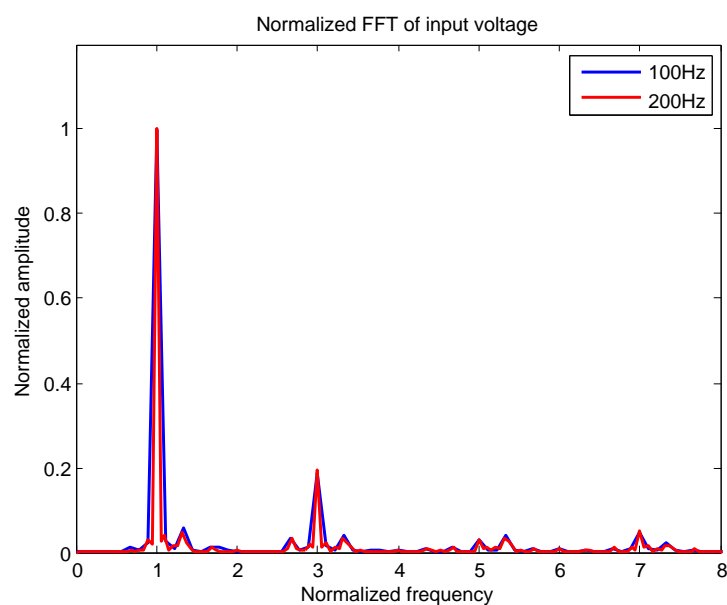


FIGURE 4.34: High order harmonics of harvester voltage under 100Hz and 200Hz.

Conventional MPPT converters and controllers normally use diode bridge rectifier as the first stage followed by a DC-DC converter. The MPPT algorithm is applied to the DC-DC converter duty ratio. With low harvester line voltage, there is significant power loss from the bridge diode bridge. These losses are reduced using the topologies presented in this chapter. Further, the proposed maximum power point trackers introduce new methods to adjust the input current on the AC side to force an impedance matching criteria. Compared to the conventional fixed duty ratio methods for MPPT [1, 2, 23, 37, 43, 44], the output power of proposed algorithms is closer to the theoretical maximum value. This chapter also experimentally demonstrated that the two new proposed MPPT algorithms can operate and adjust with changing harvester input line frequency. Experimental results verify the theory and also show that higher efficiency can be achieved with the proposed MPPT control algorithm.

Chapter 5

Conclusions and Future Work

The research presented in this thesis first reviewed typical approaches of modeling, power conversion topologies and control algorithms designed for the inductive magnetic energy harvesting applications. After studying the benefits and drawbacks of the previous methods, new models, power conversion circuitries and control algorithms are developed in this research to increase energy harvested. The main contributions of the research are presented as follows as well as the recommendations for future work.

5.1 Conclusions

The main contributions of this research including harvester modeling, power conversion circuit and control algorithm design are presented in Chapter 2, Chapter 3

and Chapter 4, respectively.

Chapter 2 proposes a new equivalent circuit model, which is built according to the flux variation in the magnetic field to estimate performance of the harvester. In order to enhance the output energy of the energy harvesting system, an equivalent circuit model is required to study the electrical performance of the harvester with its AC-DC converter. The proposed model employs a magnetizing inductance and a leakage inductance to represent the effect of the excitation current and the leakage flux of the magnetic field, respectively. With the equivalent circuit model, the harvester and the converter can be analyzed as a system using the circuit theory and circuit simulation software that simplifies the analysis process dramatically. Simulation and experimental setup are built to validate the proposed model.

Chapter 3 introduces two new AC-DC converter topologies built for inductive magnetic harvesters, including several resonant capacitive rectifiers that work at rotation/vibration frequency, and also a high switching frequency AC-DC converter to boost the harvester AC input voltage to 3.3VDC. With the equivalent circuit model derived in Chapter 2, the leakage inductance/air gap is tuned in the simulation to achieve the optimal operation point of the harvesting system. Further, the new proposed AC-DC converters are designed, built and experimentally tested. The equivalent circuit model from Chapter 2 is utilized to simulate the entire harvesting system with the AC-DC converters.

Chapter 4 proposed two new MPPT control methods specialized for magnetic energy harvesters. A new Phase/RMS MPPT algorithm tunes the phase and RMS value of the converter input current with perturb and observe method without voltage reference. Compared to the conventional methods, the proposed method may give higher output power since it approaches the theoretical maximum power point. It also has faster dynamic response to the change of the harvester line voltage and frequency, which is more feasible to apply to the applications with changing energy sources such as kinetic energy harvesters. The Phase/RMS MPPT method is then simplified to a quasi-MPPT method that directly adjusts converter duty ratio. Compared to the conventional PWM-based MPPT algorithm, it still has faster response to the harvester line and frequency change. Both simulation and experimental results verify the theory and also show that higher converter efficiency and output power can be achieved with the proposed MPPT control algorithms.

5.2 Future Work

As mentioned in Chapter 3, the difficulty of the power conversion circuit design is to achieve both high energy density and high energy efficiency due to harvester's low voltage and low frequency AC output. Obviously, the transformer size will become unacceptable under such low frequency. So, most of the power conversion circuits designed for magnetic harvester, including the proposed dual boost power

converter in this research, tend to use boost derived topologies to increase the voltage before rectification stage to avoid some power loss [11–15]. In this case, the boost circuits work at high switching frequency to guarantee the energy density of the converter is acceptable, and the line frequency of the harvester voltage is not changed. However, an alternative solution may be created with a special circuit to enhance the harvester frequency (Fig. 5.1). Under high input frequency, the size of the step-up transformer will not be a problem. It would be a nice topic to explore whether any resonant circuit could be attached to the transformer harvester to increase the frequency.

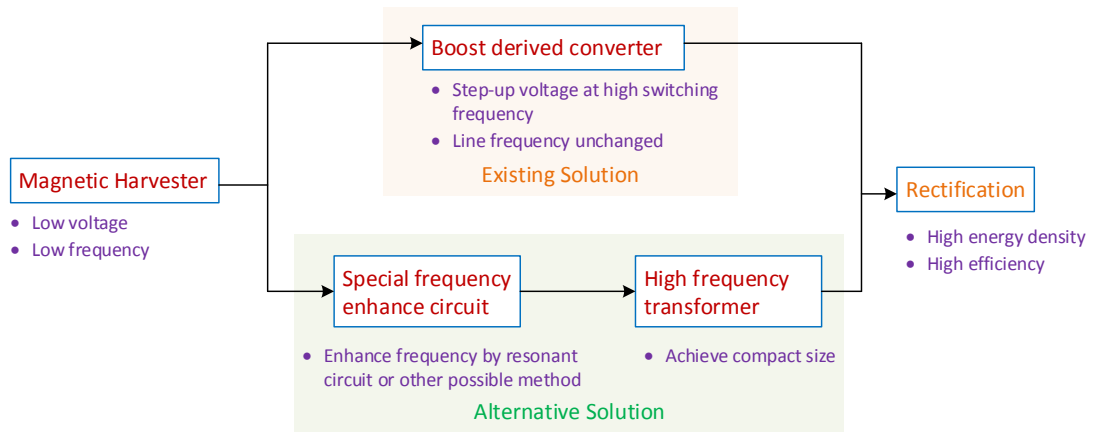


FIGURE 5.1: Alternative power conversion solution.

Due to the intermittent nature of the energy source of the magnetic harvesters, many converter designs employed maximum power point tracking algorithm [1, 18, 23, 37], sometimes with a battery or super capacitor as energy storage. With maximum power point tracking, the converter output voltage is uncontrolled. All the existing solutions tend to connect either a battery or a resistive load to the

converter. Even when a battery is connected, the battery voltage would change in a wide range under different charge and discharge conditions, which restricts the practical application when the real load is connected. In order to improve the converter for the practical use, there are still remaining questions that can be investigated in future research.

- Is it advantageous to add a second DC-DC converter to control the converter output voltage? If MPPT algorithm is applied, the output power is controlled and the harvesting circuit is not able to control the output voltage simultaneously. If voltage regulation is required, it is normally achieved by adding a second converter as voltage regulator. However, this may introduces extra power loss to the harvesting system. Research should investigate any design trade-offs when adding the additional converter.
- Is it necessary to apply a power management algorithm when the battery and load both exist? When the battery and load are both present, a power management algorithm is needed to regulate the power flow at high efficiency. However, a more complicated energy control algorithm may also require addition power to run the control circuits (auxiliary power). For power sensitive applications, a future topic of research may be to derive methods that simplify and combine the power management with the existing MPPT algorithm to adapt the demand with limited power. This may lead to new topologies that merge energy management and MPPT circuits together.

The future work may focus on these topics and improve the existing designs for practical use.

Appendix A

Source Code of The Phase/RMS Algorithm

```
#include <msp430.h>

#define RSLT 100 //Number of input current point saved
#define ZERO 511 //zero point of input current
#define Fsin_std 64 //standard number of points of reference current: 100Hz/25k/2
#define Fcount 3

const int I_ref[Fsin_std+1] = {0,12,23,35,47,59,72,85,98,112,127,141,157,173,189,205,
222,240,257,275,293,310,328,345,362,379,395,410,424,438, 450,462,472,481,488,495,
500,503,505,506,506,504,501,497, 491,485,478,470,462,453,444,435,425,416,407,399,
391,383, 377,371,366,362,359,357,357};

const int *Phase = I_ref;
```

```
volatile int step = 1;  
  
volatile int shift = 3;  
  
volatile unsigned int Amplitude = 40; //The amplitude of I_ref is divided by 32  
  
volatile int delta=1;  
  
volatile int Period=0, Loopcounter=0;  
  
volatile int T=2392, Tflag = 0;//40hz  
  
volatile long totalfsw;  
  
  
  
int LinArray[RSLT] = {512,512,512,512,512,512,512,512,512,512,512,512,512,512,512,  
512,512,512,512,512,512,512,512,512,512,512,512,512,512,512,512,512,512,512,512,  
512,512,512,512,512,512,512,512,512,512,512,512,512,512,512,512,512,512,512,512,  
512,512,512,512,512,512,512,512,512,512,512,512,512,512,512,512,512,512,512,512,  
512,512,512,512,512,512,512,512,512,512,512,512,512,512,512,512,512,512,512,512,512,  
512,512,512,512};  
  
volatile int LinTemp=512;  
  
volatile signed int Lin = 0;  
  
volatile int *I_POINT = I_inArray;  
  
  
  
volatile signed int errorL; //error of last period and current period  
  
volatile int PWM = 2152, PWM_L = 0; //On time of last period and this period  
  
volatile int Duty_Max = 2152, Duty_Min = 300;
```

```
//volatile unsigned int a=0, b=0, c=0, d=0;//for test use  
volatile unsigned int ConFlag = 0; //Flag of the beginning of each switching cycle  
volatile int Rst1 = 0, mark = 2;//Reset current reference to the beginning of a  
period  
  
volatile long Fsin_C=0, Fsin = 0; //number of points of input current in last pe-  
riod and current period  
volatile int FlagFsin=0;  
volatile int Fsin_Array[Fcount+1] = {0,0,0,0};  
volatile int *F_POINT = Fsin_Array;  
volatile long Fsin_sum=0;  
  
volatile long I_sum = 0, I_sumnew = 0;  
volatile long I_avg = 0, I_avgold = 0;  
  
void ConfigWDT(void);  
void ConfigClocks(void);  
void ConfigADC10(void);  
void ConfigTimerA(void);
```

```
void PhaseLoop(void);

void CurrentLoop(void);

void main(void)

{

//Initiate system

ConfigWDT();

ConfigClocks();

ConfigADC10();

ConfigTimerA();

P1DIR |= BIT0; // Set P1.0 to output direction

P1OUT &= ~BIT0; // Turn LED off

.BIS_SR(GIE);

while(1)

{ //The beginning of a switching cycle

if (ConFlag==1)

{ PhaseLoop();

CurrentLoop();
```

```
ConFlag = 0;  
}  
  
}  
}  
}  
} void ConfigWDT(void)  
{ WDTCTL = WDTPW + WDTHOLD; // Stop watchdog timer  
}  
  
  
  
void ConfigClocks(void)  
{ PJSEL == BIT4+BIT5; // Port select XT1  
UCSCTL6 &= ~(XT1OFF); // XT1 On  
UCSCTL6 |= XCAP_3; // Internal load cap 12pF  
UCSCTL3 = 0; // FLL Reference Clock = XT1  
  
  
  
// Loop until XT1 & DCO stabilizes - In this case loop until XT1 and DCo settle  
do  
{ UCSCTL7 &= ~(XT1LFOFFG + XT1HFOFFG + DCOffG);  
// Clear XT1,DCO fault flags  
SFRIFG1 &= ~OFIFG; // Clear fault flags  
}while (SFRIFG1&OFIFG); // Test oscillator fault flag  
UCSCTL6 &= ~(XT1DRIVE_3); // Xtal is now stable, reduce drive strength
```

```
UCSCTL4 |= SELA_3 + SELM_4; // ACLK = DCO

// Initialize DCO to 24MHz
__bic_SR_register(SCG0); // Disable the FLL control loop
UCSCTL0 = 0x0000; // Set lowest possible DCOx, MODx
UCSCTL1 = DCORSEL_5; // Select DCO range 24MHz operation
UCSCTL2 = FLLD_0 + 762; // Set DCO Multiplier for 12MHz
// (N + 1) * FLLRef = Fdco
// 1 * (762 + 1) * 32768 = 24.5MHz
// Set FLL Div = fDCOCLK/1
__bic_SR_register(SCG0); // Enable the FLL control loop

// Worst-case settling time for the DCO when the DCO range bits have been
// changed is n x 32 x 32 x f_MCLK / f_FLL_reference. See UCS chapter in 5xx
// UG for optimization.
// 32 x 32 x 12 MHz / 32,768 Hz = 375000 = MCLK cycles for DCO to settle
__delay_cycles(375000);

}

void ConfigADC10(void)
{
    ADC10CTL0 == ADC10SHT_3 + ADC10ON; //ADC10 ON
```

```
//ADC10 sample-and-hold time 32*ADC10CLKs  
ADC10CTL1 == ADC10SHP; // ADCCLK = MODOSC; sampling timer  
ADC10CTL2 == ADC10RES; // 10-bit conversion results  
ADC10MCTL0 == ADC10INCH_1 + ADC10SREF_0; // A1 ADC input select;  
Vref=VCC  
  
ADC10CTL0 == ADC10ON; //ADC10 ON  
ADC10CTL0 == ADC10ENC + ADC10SC; // Sampling and conversion start  
  
}  
  
void ConfigTimerA(void)  
{ // Configure ports P3DIR == BIT6 + BIT5; // P3.6 and P3.5 output  
P3SEL == BIT6 + BIT5; // P3.6 and P3.5 options select  
  
// configure TA0  
TA0CCR0 = T; // PWM Period  
TA0CCTL0 == CCIE; // Enable CCR0 interrupt  
TA0CCTL1 = OUTMOD_6 + CCIE; // CCR1 toggle/set, enable CCR1 interrupt  
TA0CTL = TASSEL_1 + MC_1 + TACLR; // ACLK, up mode, clear TAR  
TA0CCR1 = 800; // CCR1 PWM duty cycle
```

}

```
#pragma vector=TIMER0_A1_VECTOR
__interrupt void Timer_A1 (void)
{
    ADC10CTL0 == ADC10ON; //ADC10 ON
    ADC10CTL0 == ADC10ENC + ADC10SC; // Sampling and conversion start
    TA0CCTL1 &= ~CCIFG;
}
```

```
#pragma vector=TIMER0_A0_VECTOR
```

```
__interrupt void Timer_A0 (void)
```

```
{
```

```
TA0CCR1 = PWM; // CCR1 PWM duty cycle
```

```
while(ADC10CTL1 & ADC10BUSY); //Check if the ADC conversion is finished;
```

```
b++ for test
```

```
I_inTemp = ADC10MEM0; // Read conversion value
```

```
ADC10IFG &= ~ADC10IFG0;
```

```
TA0CCTL0 &= ~CCIFG;
```

```
ConFlag = 1;
```

```
I_inTemp = (*I_POINT + I_inTemp) / 1;
```

```
ADC10CTL0 &= ~ADC10ENC + ADC10SC); // Disable ADC conversion  
// ADC10CTL0 &= ~ADC10ON; // Ref and ADC10 off  
}
```

```
void PhaseLoop(void)  
{  
    volatile unsigned int offTime;  
    volatile unsigned long result;  
    volatile long I_avgnew=0;  
    volatile long Remainder;  
    volatile int count2=0;  
    volatile int checkFsin;
```

```
if (I_POINT >= LinArray + RSLT -1) //If current pointer is out of range, reset  
I_POINT = LinArray;  
else  
I_POINT++;  
  
*I_POINT = LinTemp;
```

```
//—Detect if there is an rising edge—  
if (*I.POINT < ZERO)  
{  
    I_in = *I.POINT - ZERO;  
    if (mark == 1 && Rst1 > 0)  
        Rst1++;  
    else if (mark == 0)  
        Rst1=1;  
    mark = 1;  
}  
else  
{  
    I_in = ZERO - *I.POINT;  
    if (mark == 1)  
        Rst1 = 0;  
    mark = 0;  
}  
  
Fsin_C++;  
  
//—Calculate the average of this period and reset at zero crossing—  
if((Rst1>=8))
```

```

{
//reset zero crossing flag

Rst1=0;

if (Fsin_C<=120) { //Calculate the average current of input period before T is
updated

MPY = T; // Load first operand -signed mult

OP2 = Fsin_C; // Load second operand

totalfsw = RESHI;

totalfsw = (totalfsw<<16)|RESLO;

while((totalfsw = totalfsw<<1)<=I_sumnew)

count2++; //Left aligned

totalfsw=totalfsw>>1;//recover

for(;count2>=0;count2--)

{

if(I_sumnew>=totalfsw)

{

I_sumnew=I_sumnew - totalfsw;

```

```
totalfsw=totalfsw>>1;//new round  
I_avgnew+=(0x01<<count2);  
}  
else  
{  
totalfsw=totalfsw>>1;  
continue;  
}  
}
```

```
//Check if the measured frequency is correct  
//checkFsin=Fsin_C-*F_POINT;  
if (FlagFsin==0&&Tflag==0)  
{  
if (Fsin_C>296——Fsin_C<216)  
{  
T=1700;  
FlagFsin=1;  
}  
}
```

```
//Calculate the average period  
Fsin_sum = Fsin_sum + Fsin_C-*F_POINT;
```

```
Fsin = Fsin_sum>>2;  
  
*F_POINT = Fsin_C;  
  
}  
  
else  
  
{  
  
Fsin_sum = Fsin_sum + 256-*F_POINT;  
  
*F_POINT = 256;  
  
Fsin = Fsin_C;  
  
FlagFsin=0;  
  
}  
  
  
  
if (F_POINT >= Fsin_Array + Fcount) //If current pointer is out of range, reset  
F_POINT = Fsin_Array;  
  
else  
  
F_POINT++;  
  
  
  
//Fsin = (Fsin_C+Fsin)>>1;  
  
  
  
//reset phase of reference current  
Fsin_C=0;
```

```
I_sumnew = 0;

//Calculate and update the new switching frequency if T is not set to average

if (FlagFsin==0)

{

MPYS = T; // Load first operand -signed mult

OP2 = Fsin; // Load second operand

totalfsw = RESHI;

totalfsw = (totalfsw<<16)—RESLO; //+I_rem

T = totalfsw>>8;

if (T<900&&T>0)

{

T=1700;

Tflag = 1;

}

else if (T>2800||T<=0)

{

T=1700;

Tflag = 1;

}

else
```

```
Tflag = 0;  
}  
TA0CCR0 = T; // Update switching period
```

```
if (Loopcounter>0)  
{  
    I_avg=I_avg + I_avgnew;  
}  
//Perturb and Observe each 2 input cycle  
//Calculate average current in the 1 cycle  
if (Loopcounter>=2)  
{  
    //Perturb and Observe  
    if (Period<10)  
    {  
        if (I_avg<I_avgold)  
            shift = -shift;  
        Phase = I_ref + 9 + shift; //reset phase of reference current  
    }  
    else  
    {  
        if (I_avg<I_avgold)
```

```
delta = -delta;  
Amplitude = Amplitude + delta;  
if (Amplitude>60)  
    Amplitude = 60;  
Phase = I_ref + 9;  
}  
//Reset the average current  
I_avgold = I_avg;  
I_avg = 0;
```

```
Period++;  
  
if (Period>=20)  
    Period=0;  
    Loopcounter=0;  
}  
else  
{  
    Loopcounter++;  
    Phase = I_ref + 9;  
}  
}
```

```
// else if (Fsin_C>=500)
// {
// Fsin_C=0;
// I_sumnew = 0;
// I_avg=0;
// I_avgold=0;
// T=2392;//40hz
// TA0CCR0 = T; // Update switching period
// } }

// -Calculate the average current of one switching cycle-
if (I_in>5 && PWM>200)
{
    offTime = T-PWM;
    MPY = offTime; // Load first operand -signed mult
    OP2 = I_in; // Load second operand
    result = RESHI;
    result = (result<<16)|RESLO; //+I_rem
    //I_in * offTime = I_sum of one cycle
    I_sumnew = I_sumnew + result;
}
```

}

void CurrentLoop(void)

{

volatile signed int error, errorC;

volatile int edge;

volatile unsigned long value;

volatile unsigned int ref;

ref = *Phase;

MPY = ref; // Load first operand -signed mult

OP2 = Amplitude; // Load second operand

value = RESLO;

errorC = (value>>6) - I_in;

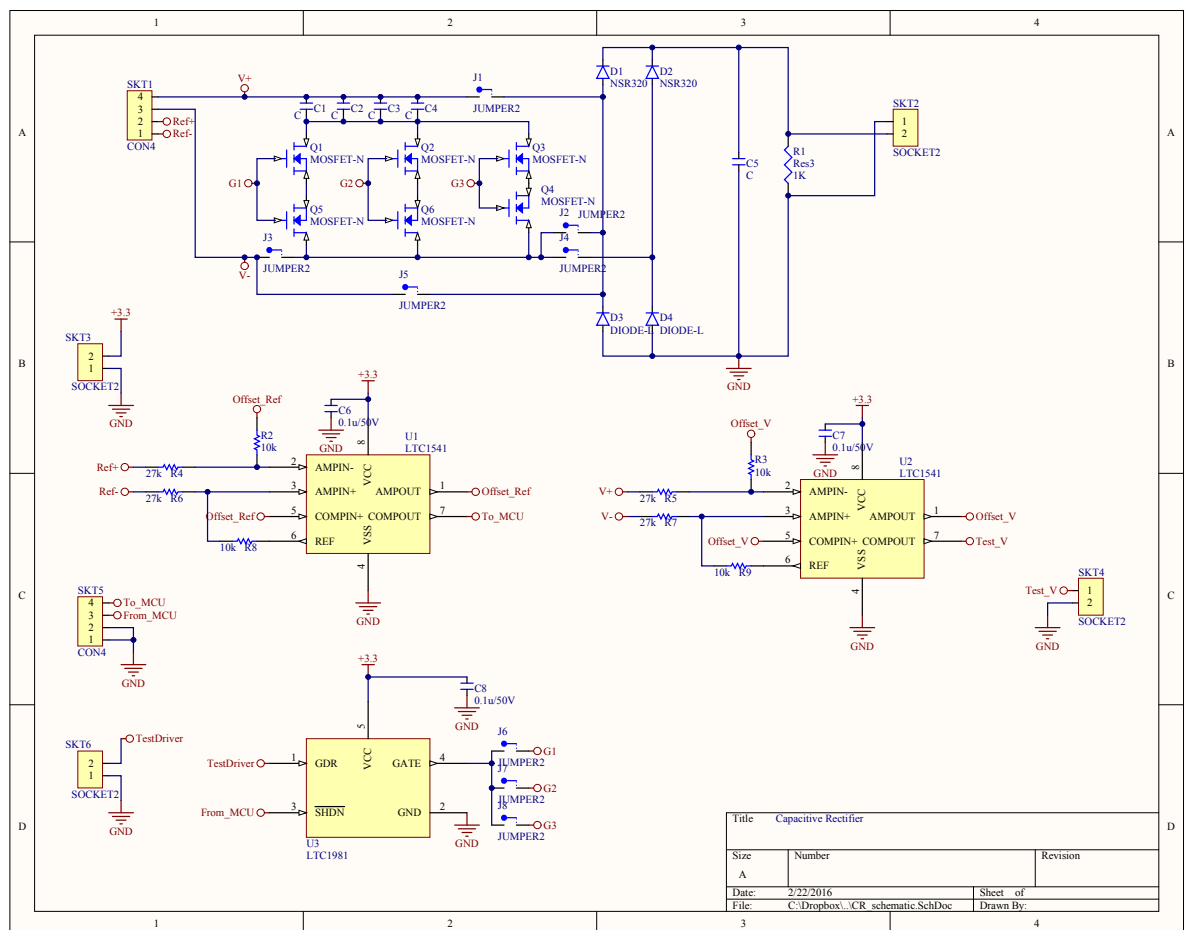
error = errorC - errorL;

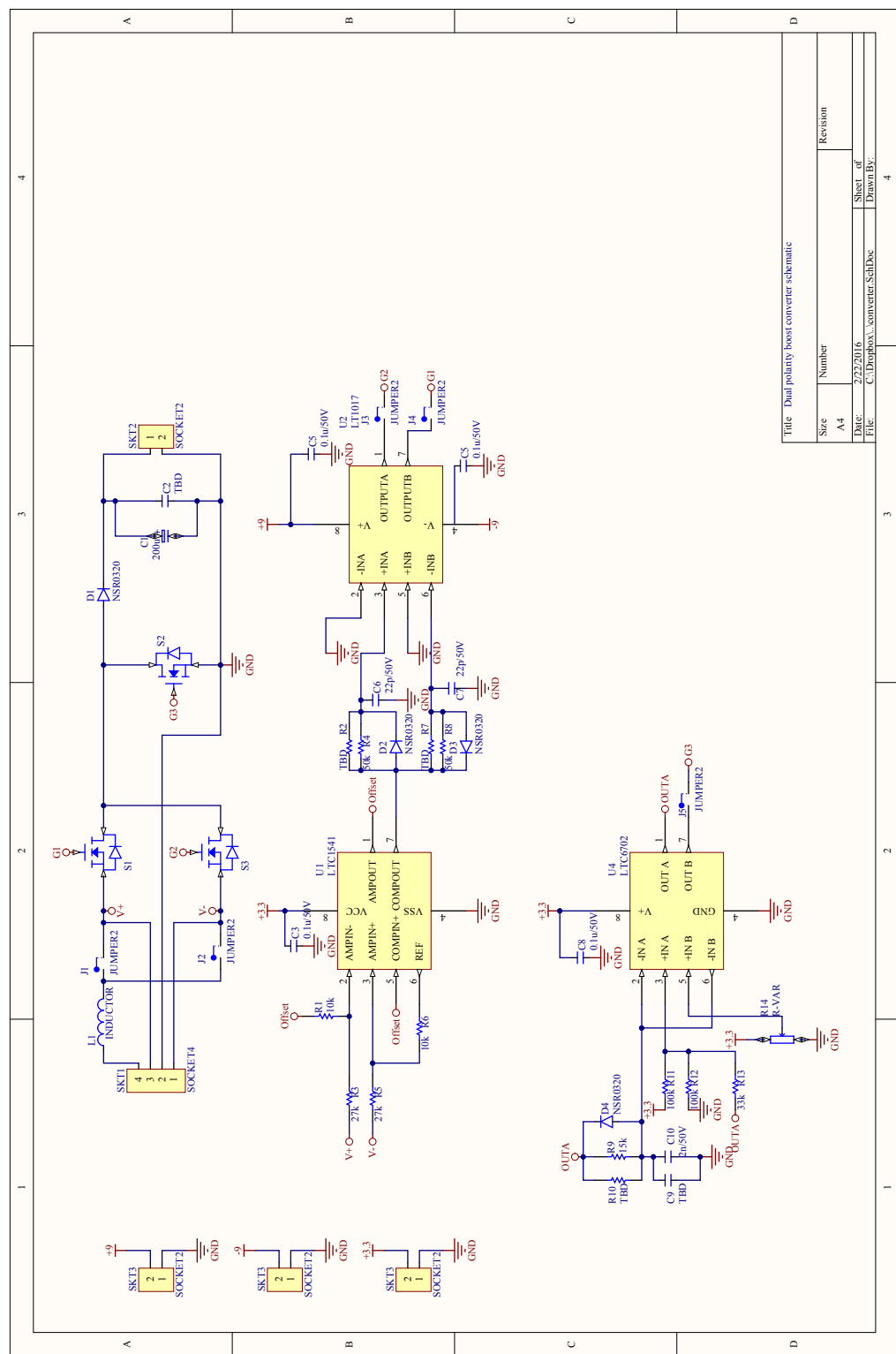
PWM = (error>>1) + (errorC>>3)- (errorL>>4) + PWM_L;

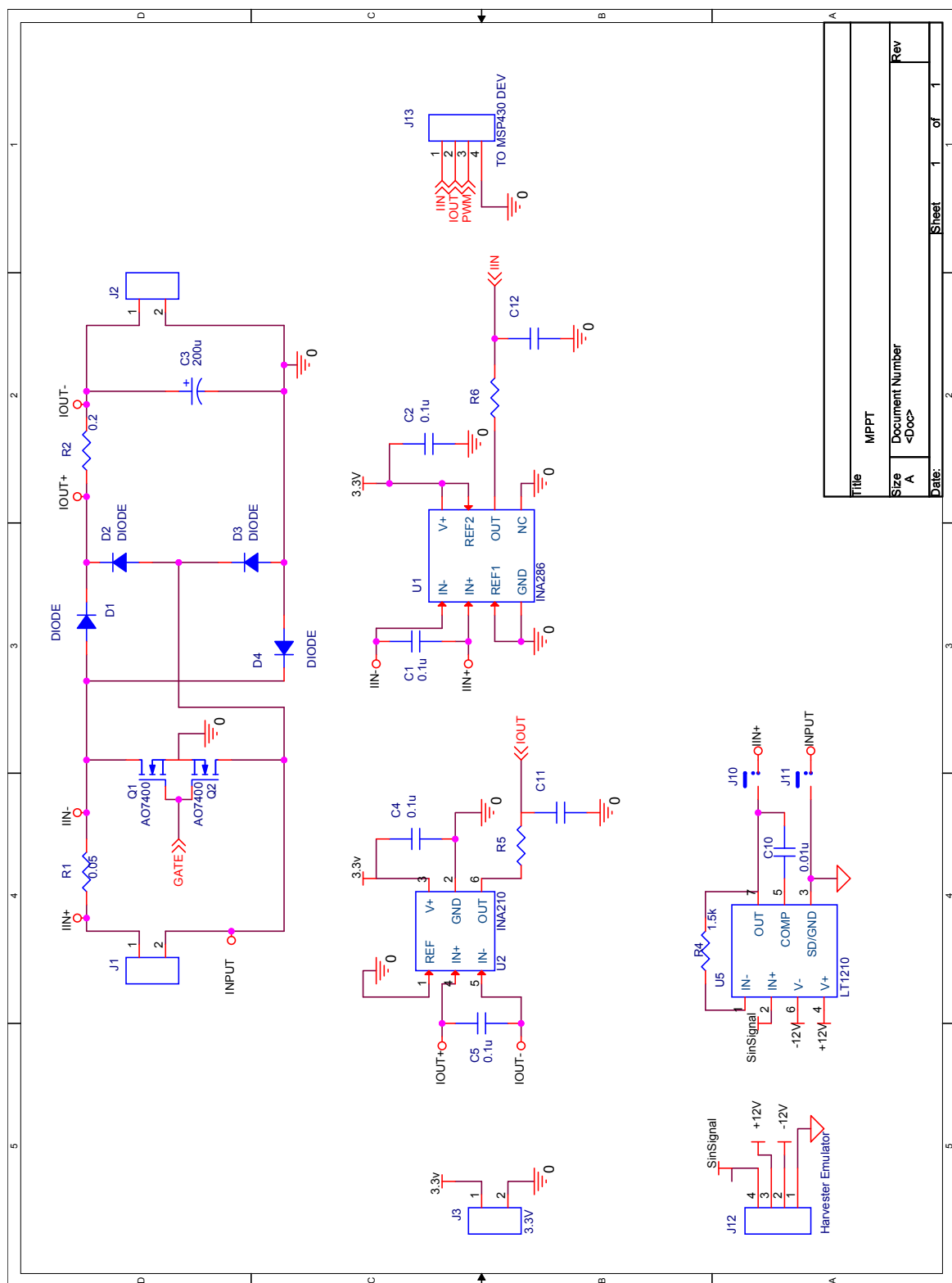
```
Duty_Max = (T>>1)+(T>>2)+(T>>4);  
Duty_Min = T>>3;  
if (PWM > Duty_Max||Tflag==1||FlagFsin==1)  
    PWM = Duty_Max;  
if (PWM < Duty_Min)  
    PWM = Duty_Min;  
  
if (Phase >= I_ref + Fsin_std)  
    step = -1;  
if (Phase <= I_ref)  
    step = 1;  
Phase = Phase + step;  
  
PWM_L = PWM;  
errorL = errorC;  
P1OUT ^= BIT0;  
}
```

Appendix B

Converter Schematics







Bibliography

- [1] G. Ottman, H. Hofmann, A. Bhatt, and G. Lesieutre, “Adaptive piezoelectric energy harvesting circuit for wireless remote power supply,” *Power Electronics, IEEE Transactions on*, vol. 17, no. 5, pp. 669–676, Sep 2002.
- [2] E. Lefevre, D. Audiger, C. Richard, and D. Guyomar, “Buck-boost converter for sensorless power optimization of piezoelectric energy harvester,” *Power Electronics, IEEE Transactions on*, vol. 22, no. 5, pp. 2018–2025, Sept 2007.
- [3] A. Badel, D. Guyomar, E. Lefevre, and C. Richard, “Piezoelectric energy harvesting using a synchronized switch technique,” *Journal of Intelligent Material Systems and Structures*, vol. 17, no. 8-9, pp. 831–839, 2006. [Online]. Available: <http://jim.sagepub.com/cgi/content/abstract/17/8-9/831>
- [4] A. Badel, D. Guyomar, E. Lefevre, and C. Richard, “Efficiency enhancement of a piezoelectric energy harvesting device in pulsed operation by synchronous charge inversion,” *Journal of Intelligent Material Systems*

- and Structures*, vol. 16, no. 10, pp. 889–901, 2005. [Online]. Available: <http://jim.sagepub.com/cgi/content/abstract/16/10/889>
- [5] L. Garbuio, M. Lallart, D. Guyomar, C. Richard, and D. Audigier, “Mechanical energy harvester with ultralow threshold rectification based on shi nonlinear technique,” *Industrial Electronics, IEEE Transactions on*, vol. 56, no. 4, pp. 1048–1056, April 2009.
- [6] S. Meninger, J. Mur-Miranda, R. Amirtharajah, A. Chandrakasan, and J. H. Lang, “Vibration-to-electric energy conversion,” *Very Large Scale Integration (VLSI) Systems, IEEE Transactions on*, vol. 9, no. 1, pp. 64–76, Feb 2001.
- [7] E. Torres and G. Rincon-Mora, “Electrostatic energy harvester and li-ion charger circuit for micro-scale applications,” in *Circuits and Systems, 2006. MWSCAS '06. 49th IEEE International Midwest Symposium on*, vol. 1, Aug 2006, pp. 65–69.
- [8] P. Li, Y. Wen, C. Jia, and X. Li, “A magnetoelectric composite energy harvester and power management circuit,” *Industrial Electronics, IEEE Transactions on*, vol. 58, no. 7, pp. 2944–2951, July 2011.
- [9] X. Xing, G. M. Yang, M. Liu, J. Lou, O. Obi, and N. X. Sun, “High power density vibration energy harvester with high permeability magnetic material,” *Journal of Applied Physics*, vol. 109, no. 7, 2011.
- [10] X. Xing, J. Lou, G. M. Yang, O. Obi, C. Driscoll, and N. X. Sun, “Wideband vibration energy harvester with high permeability magnetic material,”

- Applied Physics Letters*, vol. 95, no. 13, pp. 1–1, 2009. [Online]. Available: <http://scitation.aip.org/content/aip/journal/apl/95/13/10.1063/1.3238319>
- [11] R. Dayal, S. Dwari, and L. Parsa, “A new design for vibration-based electromagnetic energy harvesting systems using coil inductance of microgenerator,” *Industry Applications, IEEE Transactions on*, vol. 47, no. 2, pp. 820–830, March 2011.
- [12] P. Mitcheson, T. Green, and E. Yeatman, “Power processing circuits for electromagnetic, electrostatic and piezoelectric inertial energy scavengers,” *Microsystem Technologies*, vol. 13, no. 11-12, pp. 1629–1635, 2007. [Online]. Available: <http://dx.doi.org/10.1007/s00542-006-0339-0>
- [13] R. Dayal, S. Dwari, and L. Parsa, “Design and implementation of a direct ac-dc boost converter for low-voltage energy harvesting,” *Industrial Electronics, IEEE Transactions on*, vol. 58, no. 6, pp. 2387–2396, June 2011.
- [14] S. Dwari and L. Parsa, “An efficient ac-dc step-up converter for low-voltage energy harvesting,” *Power Electronics, IEEE Transactions on*, vol. 25, no. 8, pp. 2188–2199, Aug 2010.
- [15] H. Wang, Y. Tang, and A. Khaligh, “A bridgeless boost rectifier for low-voltage energy harvesting applications,” *Power Electronics, IEEE Transactions on*, vol. 28, no. 11, pp. 5206–5214, Nov 2013.

- [16] G. Szarka, S. Burrow, and B. Stark, “Ultralow power, fully autonomous boost rectifier for electromagnetic energy harvesters,” *Power Electronics, IEEE Transactions on*, vol. 28, no. 7, pp. 3353–3362, July 2013.
- [17] Y. Rao and D. Arnold, “An input-powered vibrational energy harvesting interface circuit with zero standby power,” *Power Electronics, IEEE Transactions on*, vol. 26, no. 12, pp. 3524–3533, Dec 2011.
- [18] G. Szarka, S. Burrow, P. Proynov, and B. Stark, “Maximum power transfer tracking for ultralow-power electromagnetic energy harvesters,” *Power Electronics, IEEE Transactions on*, vol. 29, no. 1, pp. 201–212, Jan 2014.
- [19] A. Nasiri, S. Zabalawi, and D. Jeutter, “A linear permanent magnet generator for powering implanted electronic devices,” *Power Electronics, IEEE Transactions on*, vol. 26, no. 1, pp. 192–199, Jan 2011.
- [20] R. Amirtharajah, J. Wenck, J. Collier, J. Siebert, and B. Zhou, “Circuits for energy harvesting sensor signal processing,” in *Design Automation Conference, 2006 43rd ACM/IEEE*, 2006, pp. 639–644.
- [21] E. Dallago, M. Marchesi, and G. Venchi, “Analytical model of a vibrating electromagnetic harvester considering nonlinear effects,” *Power Electronics, IEEE Transactions on*, vol. 25, no. 8, pp. 1989–1997, Aug 2010.

- [22] L. Wang, T. Kazmierski, B. Al-Hashimi, S. Beeby, and R. Torah, “An integrated approach to energy harvester modeling and performance optimization,” in *Behavioral Modeling and Simulation Workshop, 2007. BMAS 2007. IEEE International*, Sept 2007, pp. 121–125.
- [23] N. Kong and D. S. Ha, “Low-power design of a self-powered piezoelectric energy harvesting system with maximum power point tracking,” *Power Electronics, IEEE Transactions on*, vol. 27, no. 5, pp. 2298–2308, May 2012.
- [24] G. Szarka, B. Stark, and S. Burrow, “Review of power conditioning for kinetic energy harvesting systems,” *Power Electronics, IEEE Transactions on*, vol. 27, no. 2, pp. 803–815, Feb 2012.
- [25] Y. Sun, N. H. Hieu, C.-J. Jeong, and S.-G. Lee, “An integrated high-performance active rectifier for piezoelectric vibration energy harvesting systems,” *Power Electronics, IEEE Transactions on*, vol. 27, no. 2, pp. 623–627, Feb 2012.
- [26] A. Phipps and T. Nishida, “System modeling of piezoelectric energy harvesters,” *Power Electronics, IEEE Transactions on*, vol. 27, no. 2, pp. 790–802, Feb 2012.
- [27] J. Dicken, P. Mitcheson, I. Stoianov, and E. Yeatman, “Power-extraction circuits for piezoelectric energy harvesters in miniature and low-power applications,” *Power Electronics, IEEE Transactions on*, vol. 27, no. 11, pp. 4514–4529, Nov 2012.

- [28] C. Lu, C. Tsui, and W. Ki, "Vibration energy scavenging system with maximum power tracking for micropower applications," *Very Large Scale Integration (VLSI) Systems, IEEE Transactions on*, vol. 19, no. 11, pp. 2109–2119, Nov 2011.
- [29] C. Luo and H. Hofmann, "Wideband energy harvesting for piezoelectric devices with linear resonant behavior," *Ultrasonics, Ferroelectrics, and Frequency Control, IEEE Transactions on*, vol. 58, no. 7, pp. 1294–1301, July 2011.
- [30] X. Liu and E. Sanchez-Sinencio, "20.7 a 0.45-to-3v reconfigurable charge-pump energy harvester with two-dimensional mppt for internet of things," in *Solid-State Circuits Conference - (ISSCC), 2015 IEEE International*, Feb 2015, pp. 1–3.
- [31] Q. Sun, S. Patil, S. Stoute, N. Sun, and B. Lehman, "Optimum design of magnetic inductive energy harvester and its ac-dc converter," in *Energy Conversion Congress and Exposition (ECCE), 2012 IEEE*, Sept 2012, pp. 394–400.
- [32] Q. Sun, S. Patil, N. Sun, and B. Lehman, "Modeling and optimization of an inductive magnetic harvester considering nonlinear effects," in *Control and Modeling for Power Electronics (COMPEL), 2013 IEEE 14th Workshop on*, June 2013, pp. 1–6.

- [33] S. Cheng, Y. Jin, Y. Rao, and D. Arnold, “An active voltage doubling ac/dc converter for low-voltage energy harvesting applications,” *Power Electronics, IEEE Transactions on*, vol. 26, no. 8, pp. 2258–2265, Aug 2011.
- [34] N. Golbon and G. Moschopoulos, “A low-power ac-dc single-stage converter with reduced dc bus voltage variation,” *Power Electronics, IEEE Transactions on*, vol. 27, no. 8, pp. 3714–3724, Aug 2012.
- [35] S. Cheng, R. Sathe, R. Natarajan, and D. Arnold, “A voltage-multiplying self-powered ac/dc converter with 0.35-v minimum input voltage for energy harvesting applications,” *Power Electronics, IEEE Transactions on*, vol. 26, no. 9, pp. 2542–2549, Sept 2011.
- [36] D. Maurath, P. Becker, D. Spreemann, and Y. Manoli, “Efficient energy harvesting with electromagnetic energy transducers using active low-voltage rectification and maximum power point tracking,” *Solid-State Circuits, IEEE Journal of*, vol. 47, no. 6, pp. 1369–1380, June 2012.
- [37] R. Dayal, K. Modepalli, and L. Parsa, “A new optimum power control scheme for low-power energy harvesting systems,” *Industry Applications, IEEE Transactions on*, vol. 49, no. 6, pp. 2651–2661, Nov 2013.
- [38] J. Leicht, M. Amayreh, C. Moranz, D. Maurath, T. Hehn, and Y. Marioli, “20.6 electromagnetic vibration energy harvester interface ic with conduction-angle-controlled maximum-power-point tracking and harvesting efficiencies

- of up to 90%,” in *Solid- State Circuits Conference - (ISSCC), 2015 IEEE International*, Feb 2015, pp. 1–3.
- [39] Q. Sun, S. Patil, N. Sun, and B. Lehman, “Inductive magnetic harvester with resonant capacitive rectifier based on synchronized switch harvesting technique,” in *Energy Conversion Congress and Exposition (ECCE), 2013 IEEE*, Sept 2013, pp. 4940–4947.
- [40] T. Huang, M. Du, Y. Kang, R. Peng, K. Chen, Y. Lin, T. Tsai, C. Lee, L. Chen, and J. Chen, “120% harvesting energy improvement by maximum power extracting control for high sustainability magnetic power monitoring and harvesting system,” *Power Electronics, IEEE Transactions on*, vol. 30, no. 4, pp. 2262–2274, April 2015.
- [41] S. Heo, Y. Yang, J. Lee, S. Lee, and J. Kim, “Micro energy management for energy harvesting at maximum power point,” in *Integrated Circuits (ISIC), 2011 13th International Symposium on*, Dec 2011, pp. 136–139.
- [42] X. Liu, L. Huang, K. Ravichandran, and E. Snchez-Sinencio, “A highly efficient reconfigurable charge pump energy harvester with wide harvesting range and two-dimensional mppt for internet of things,” *IEEE Journal of Solid-State Circuits*, vol. 51, no. 5, pp. 1302–1312, May 2016.
- [43] C. Lu, S. Park, V. Raghunathan, and K. Roy, “Low-overhead maximum power point tracking for micro-scale solar energy harvesting systems,” in *VLSI Design (VLSID), 2012 25th International Conference on*, Jan 2012, pp. 215–220.

- [44] T. Esram and P. Chapman, “Comparison of photovoltaic array maximum power point tracking techniques,” *Energy Conversion, IEEE Transactions on*, vol. 22, no. 2, pp. 439–449, June 2007.
- [45] H. Nagayoshi, T. Kajikawa, and T. Sugiyama, “Comparison of maximum power point control methods for thermoelectric power generator,” in *Thermoelectrics, 2002. Proceedings ICT '02. Twenty-First International Conference on*, Aug 2002, pp. 450–453.
- [46] R. Erickson and D. Maksimovic, *Fundamental of Power Electronics*. Springer, 2001.
- [47] P. Das, M. Pahlevaninezhad, J. Drobnik, G. Moschopoulos, and P. Jain, “A nonlinear controller based on a discrete energy function for an AC/DC boost PFC converter,” *Power Electronics, IEEE Transactions on*, vol. 28, no. 12, pp. 5458–5476, Dec 2013.
- [48] K. De Gusseme, W. Ryckaert, D. Van de Sype, J. Ghijsselen, J. Melkebeek, and L. Vandevelde, “A boost PFC converter with programmable harmonic resistance,” *Industry Applications, IEEE Transactions on*, vol. 43, no. 3, pp. 742–750, May 2007.
- [49] J. Lee, H. Bae, and B. Cho, “Resistive control for a photovoltaic battery charging system using a microcontroller,” *Industrial Electronics, IEEE Transactions on*, vol. 55, no. 7, pp. 2767–2775, July 2008.

- [50] K. Kim, R. Li, and P. Krein, “Voltage-offset resistive control for dc-dc converters in photovoltaic applications,” in *Applied Power Electronics Conference and Exposition (APEC), 2012 Twenty-Seventh Annual IEEE*, Feb 2012, pp. 2045–2052.
- [51] F. Boico, B. Lehman, and K. Shujaee, “Solar battery chargers for NiMH batteries,” *Power Electronics, IEEE Transactions on*, vol. 22, no. 5, pp. 1600–1609, Sept 2007.
- [52] S. Reza Tousi, M. Moradi, N. Basir, and M. Nemati, “A function-based maximum power point tracking method for photovoltaic systems,” *Power Electronics, IEEE Transactions on*, vol. 31, no. 3, pp. 2120–2128, March 2016.
- [53] S. Saggini, S. Giro, F. Ongaro, and P. Mattavelli, “Implementation of reactive and resistive load matching for optimal energy harvesting from piezoelectric generators,” in *2010 IEEE 12th Workshop on Control and Modeling for Power Electronics (COMPEL)*, June 2010, pp. 1–6.
- [54] F. Boico, B. Lehman, and K. Shujaee, “Solar battery chargers for nimh batteries,” in *2005 IEEE 36th Power Electronics Specialists Conference*, June 2005, pp. 146–152.
- [55] J. Sun, “Input impedance analysis of single-phase pfc converters,” *Power Electronics, IEEE Transactions on*, vol. 20, no. 2, pp. 308–314, March 2005.

- [56] M. Elgendy, B. Zahawi, and D. Atkinson, “Assessment of perturb and observe mppt algorithm implementation techniques for PV pumping applications,” *Sustainable Energy, IEEE Transactions on*, vol. 3, no. 1, pp. 21–33, Jan 2012.
- [57] M. Elgendy, B. Zahawi, and D. Atkinson, “Operating characteristics of the P&O algorithm at high perturbation frequencies for standalone PV systems,” *Energy Conversion, IEEE Transactions on*, vol. 30, no. 1, pp. 189–198, March 2015.